

Winter 2016

# DUCTILITY OF 304 STAINLESS STEEL UNDER PULSED UNIAXIAL LOADING

Graham Webb Cullen

*University of New Hampshire, Durham*

Follow this and additional works at: <https://scholars.unh.edu/thesis>

---

## Recommended Citation

Cullen, Graham Webb, "DUCTILITY OF 304 STAINLESS STEEL UNDER PULSED UNIAXIAL LOADING" (2016). *Master's Theses and Capstones*. 1102.

<https://scholars.unh.edu/thesis/1102>

This Thesis is brought to you for free and open access by the Student Scholarship at University of New Hampshire Scholars' Repository. It has been accepted for inclusion in Master's Theses and Capstones by an authorized administrator of University of New Hampshire Scholars' Repository. For more information, please contact [nicole.hentz@unh.edu](mailto:nicole.hentz@unh.edu).

**DUCTILITY OF 304 STAINLESS STEEL  
UNDER PULSED UNIAXIAL LOADING**

BY

Graham W Cullen

BS Chemistry, Clarkson University 2005

THESIS

Submitted to the University of New Hampshire  
in Partial Fulfillment of  
the Requirements for the Degree of

Master of Science  
in  
Mechanical Engineering

December, 2016

This thesis has been examined and approved in partial fulfillment of the requirements for the degree of Masters of Science in Mechanical Engineering by:

Thesis Director, Yannis Korkolis, Associate Professor of Mechanical Engineering

Todd Gross, Professor of Mechanical Engineering and Materials Science

Igor Tsukrov, Professor of Mechanical Engineering and Materials Science

On October 17, 2016

Original approval signatures are on file with the University of New Hampshire Graduate School.

# TABLE OF CONTENTS

<b>LIST OF TABLES</b> .....	<b>v</b>
<b>LIST OF FIGURES</b> .....	<b>vi</b>
<b>ABSTRACT</b> .....	<b>ix</b>
<b>CHAPTER 1 INTRODUCTION</b> .....	<b>1</b>
<b>CHAPTER 2 EXPERIMENTAL</b> .....	<b>4</b>
2.1 Tensile Specimen Manufacturing.....	4
2.2 Strain Measurements.....	6
2.2.1 Extended Extensometer Arms .....	6
2.2.2 Digital Image Correlation .....	9
2.2.3 Validating DIC Strain Data .....	13
2.3 Iso-Thermal Setup .....	18
2.4 Thermal Imaging Camera .....	22
<b>CHAPTER 3 MATERIAL BEHAVIOR</b> .....	<b>24</b>
3.1 Stress Strain Curves .....	24
3.2 Determination of material properties for modeling .....	39
<b>CHAPTER 4 NUMERICAL MODELING</b> .....	<b>45</b>
4.1 Model Setup.....	45
4.1.1 Geometric Imperfection.....	46
4.1.2 Mesh Reduction and Refinement using Symmetry .....	49
4.2 Model inputs for numerical simulation.....	54
4.2.1 Displacement Control.....	54
4.2.2 Inelastic Heat Fraction .....	54
4.2.3 Input curves .....	55

4.2.4 Rate-Dependence.....	59
4.2.5 Other constants .....	61
4.3 Results.....	63
<b>CHAPTER 5 CONCLUSIONS .....</b>	<b>71</b>
<b>Bibliography.....</b>	<b>73</b>
<b>APPENDIX A: Iso-thermal Stress Strain Curves at 25, 30, 35, 60, 100, and 150°C....</b>	<b>76</b>
<b>APPENDIX B: List of all SS304 experiments .....</b>	<b>82</b>

# LIST OF TABLES

Table 3-1: Representative Experiments .....	25
Table 4-1: Data used to determine the Cowper-Symonds strain rate dependence. ....	60
Table 4-2: Yield ratios from isothermal tension experiments .....	62
Table 4-3: Material properties input to the numerical model .....	62

# LIST OF FIGURES

Figure 2-1: SS304 Sheet with coupon layout .....	4
Figure 2-2: ASTM E8 tensile specimen end-milling fixture. ....	5
Figure 2-3: ASTM E8 tensile specimen geometry. ....	6
Figure 2-4: Extensometer with extension arms.....	7
Figure 2-5: Extensometer with extension arm calibration and linearity .....	8
Figure 2-6: Extensometer noise, Blue = w/o extension arms, purple=w/ ext. arms. ....	9
Figure 2-7: Lagrangian major strain field.....	10
Figure 2-8: Tensile specimens prepared for DIC with extensometer line outlined in red.....	11
Figure 2-9: VIC-2D reference image .....	12
Figure 2-10: Virtual extensometer line.....	13
Figure 2-11: a) DIC speckles and extensometer knife edge rubber bands and, b) traditional extensometer extended arms and scribed lines 2mm apart.....	14
Figure 2-12: Comparison of scribed strain lines, DIC extensometer and traditional extensometer (with extension arms) .....	15
Figure 2-13: Specimen with scribed lines 2mm apart .....	17
Figure 2-14: DIC and scribed line engineering strain (SS-29).....	18
Figure 2-15: Heat exchanger attached to specimen, and the internals of the heat exchanger ...	19
Figure 2-16: Static mixer initially used to induce turbulent flow in the cooling channels of the heat exchanger .....	20
Figure 2-17: Iso-thermal tensile testing .....	21
Figure 2-18: Iso-thermal temperature validation, experiment # SS-97 .....	23
Figure 3-1: Stress–strain responses of 304 stainless steel.....	27
Figure 3-2: Strain-rate dependence of elongation to fracture.....	28

Figure 3-3: a) Lagrangian strain field SS-29, b) Strain evolution along gage length at different overall deformation.....	29
Figure 3-4: Strain aging of stainless steel 304.....	30
Figure 3-5: Temperature development in the tensile specimen during monotonic testing.....	32
Figure 3-6:(a) axial engineering strain, and (b) temperature, along the specimen during monotonic testing .....	33
Figure 3-7: Axial engineering strain.....	35
Figure 3-8: Temperature along the specimen during pulsed testing .....	35
Figure 3-9: Stress-strain response from Figure 3-1 with the equal time test added .....	37
Figure 3-10: Temperature evolution along the monotonic, pulsed and equal time .....	38
Figure 3-11: Duration of testing vs. elongation to fracture .....	39
Figure 3-12: Stress-strain curves of SS304 at various strain rates .....	40
Figure 3-13: Isothermal tests at various levels of strain, a) 35°C and b) 100°C. These images indicate that the specimen is maintained at a fix temperature.....	42
Figure 3-14: Isothermal stress-strain response at various temperatures .....	43
Figure 3-15: Dependence of the UTS and the elongation-to-fracture on the temperature of the isothermal tension experiments, for 3 different strain-rates.....	44
Figure 4-1: Schematic of the finite element model of the uniaxial experiments and the coordinate system adopted in this work .....	46
Figure 4-2: Linear notch size and the effect on numerical simulation of failure .....	47
Figure 4-3: Equation-driven imperfection, shown here greatly exaggerated for ease of visualization.....	48
Figure 4-4: Full model of tensile specimen, using 11016 elements.....	50
Figure 4-5: Quarter model with dense mesh of 2736 elements .....	50
Figure 4-6: Quarter model with coarse mesh of 912 elements .....	51



Figure 4-7: Comparison of the numerical simulation results from the full model (10944 elements), quarter model (2736 elements) and the coarse quarter model (912 elements)	52
Figure 4-8: Kinematic coupling boundary condition with "load cell" control point	53
Figure 4-9: Numerical input curves for both the simple notch and the equation driven notch	56
Figure 4-10: Engineering stress–strain curves of the isothermal tension experiments and their simulations.	58
Figure 4-11: Simple notch numerical model and the effect of strain rate on the output curve	59
Figure 4-12: Flow stress at various strain rates and at two levels of plastic strain, for the calibration of the Cowper-Symonds viscoplastic powerlaw.	60
Figure 4-13: Engineering stress-strain response, numerical vs experimental	63
Figure 4-14: Magnification of one unloading–reloading loop. Included are experiments and numerical simulations.	65
Figure 4-15: Axial engineering strain development along the specimen during a monotonic tension experiment and its numerical prediction	66
Figure 4-16: Comparison of the predicted temperature distribution along the monotonic	67
Figure 4-17: Numerical simulation of the dependence of the overshooting during reloading on the heat transfer between the specimen and the still air	69
Figure 4-18: Numerical predictions of the dependence of the elongation-to-fracture on the duration of the experiment, plotted with multiple experimental data.	70

# ABSTRACT

## Ductility of 304 Stainless Steel under pulsed uniaxial loading

by

Graham W Cullen

University of New Hampshire, December, 2016

The enhanced ductility that 304 stainless steel is exhibited under pulsed loading (Zhang, 2009) is investigated here using a combination of experiments and analysis. The simplest loading case, i.e., uniaxial tension, was selected to avoid the complicating effects of multiaxial stress states and/or contact and friction with a rigid die. Three types of tensile tests were performed: monotonic, pulsed and hold. For a range of strain rates, the pulsed and the hold tests exhibited different elongation-to-fracture from the monotonic tests. Digital image correlation and infrared thermography were employed to further probe this behavior. It was discovered that since the pulsed tests lasted longer than the corresponding monotonic ones (i.e., those with the same loading speed) but the total plastic work expended was comparable, milder deformation-induced heating developed in the pulsed tests. Since the resulting temperature gradients act as imperfections that trigger the localization of deformation, the enhanced elongation-to-fracture in the pulsed tests was attributed to the milder gradients that developed. Subsequently, a special isothermal tension test was used to de-couple the mechanical from the thermal behavior of the material and was repeated at various strain rates and temperatures. The material properties determined from these tests were used as input to coupled, thermomechanical finite element simulations of the experiments. Despite numerous simplifications, such as constant thermal properties with temperature, the simulations captured

the essential physics of the problem and yielded very close predictions of the elongation-to-fracture observed in the experiments.

# CHAPTER 1

## INTRODUCTION

Recent experimental findings suggest that enhanced ductility (elongation-to-fracture) can be achieved in a variety of material forming processes when the loads are applied in a slow, pulsed fashion as opposed to the more commonly used monotonic increase (Banabic D. a., 1994) (Banabic D. a., 2005) (Mori K. M., 2007) (Mori K. P., 2004) (Zhang, 2009). At the same time, the lightweight materials (aluminum, magnesium) and the advanced high strength steels that currently find increasing applications (e.g., in the automotive industry) suffer from limited ductility in comparison to the mild steels that they are meant to replace. Hence, this enhancement of ductility is of interest even for well-established processes, such as sheet and tube hydroforming.

The slow variation of the pulsed load (order of a few Hz or less) distinguishes these processes from the ultrasonically-assisted ones. It has been postulated among other reasons that the enhancement could be due to microstructural modifications of the work material by the pulsed load and/or better loading paths and/or strain-rate effects. Furthermore, it is conceivable that the enhanced formability shown in real parts (e.g., in Fig. 2 of (Mori K. P., 2004)) is due to tribological reasons: the pulsed application of the load leads to a repetitive opening and closing of the gap between the tube and the die in the areas where the two are in contact. This aids in the effective tube-die lubrication and thus it reduces the unfavorable effect of friction on formability (Korkolis, 2011). However, experiments on freely inflated (i.e., without the presence of a die) mild steel tubes also exhibited enhanced elongation-to-fracture (Mori K. M., 2007) (Mori K. P., 2004). In those experiments, the internal pressure was ramped and then oscillated, while the end-displacement of the tube was increasing monotonically throughout the deformation.

That led the tube to alternate between freely bulging and axially wrinkling depending on the value of the pressure, thus effectively increasing the axial feed of material in the burst-prone central zone of the tube. Hence the enhanced ductility was in that case due to the selection of a beneficial loading path. (Zhang, 2009) performed both pulsed tube hydroforming and pulsed uniaxial tension tests on 304 stainless steel. In both cases, an increase in the deformation before failure was observed. The authors attributed this enhancement to microstructural modification of the material. While these works have proved that the pulsed application of the load can enhance the elongation-to-fracture, both in simple and in complex loading cases, it appears that this is due to a variety of mechanisms, different for each loading case and for each work material.

There is significant literature on deformation-induced heating and thermal phenomena during mechanical straining. It is well known that the majority of the plastic work is converted into heat. (Gao Y. and Wagoner, 1991) (Farren & Taylor, 1925) (Kim, 1987) (Lin, 1987) (Raghavan K.S. and Wagoner, 1987) (Tugcu, 1995) (Rusinek, 2009) (Andrade-Campos, 2010) (Dumoulin, 2010) (Sung, 2010), (Knysh & Korkolis, 2015). At the same time, a variety of physical processes that occur during, and due to, mechanical straining involve the additional generation or absorption of heat. Such examples are the thermoelastic cooling and heating (Bottani, 1982) and the martensitic transformation (Meyers, 1998). In cases of spatially non-uniform heat generation and thermal boundary conditions, heat transfer by conduction to the grips or tools and by convection and radiation to the ambience occurs. This leads to a spatially and temporally non-uniform temperature distribution inside the specimen. As the material properties are affected by the temperature, this distribution can often trigger the localization of deformation and the eventual failure of the specimen. Therefore, if the pulsed application of the load can affect this distribution, it could effectively alter the apparent elongation-to-fracture of the material.

The enhanced elongation-to-fracture observed under pulsed loading is investigated in this thesis using a combination of experiment and analysis. The simplest possible case, i.e., uniaxial tension, is considered, to avoid the complications of multiaxial loading and contact and friction with a die. The material used is 304 stainless steel (abbrev. SS-304, also known as 18-8 stainless steel), with a basic element composition of 18% Cr and 8% Ni (and less than 0.08% C), as there is existing evidence of its enhanced ductility under pulsed loading ([Zhang, 2009](#)). This behavior is probed in this thesis by uniaxial experiments under various loading conditions. These experiments disclosed the mechanism that induced and regulated the enhanced elongation-to-fracture in the pulsed uniaxial loading of SS-304. The experiments are subsequently simulated using Abaqus/Standard. However, successful modeling requires the use of proper material properties, which in the case of SS-304 cannot be trivially extracted (e.g., from conventional tension tests) because of the coupling of the mechanical and thermal behavior. This required the development of a simple custom isothermal tension test which is described in [Chapter 2.3](#). Informed of these material properties, the coupled thermomechanical finite element modeling of the problem is discussed in [Chapter 4](#). The features and level of detail that is required for the modeling to accurately predict the enhanced elongation-to-fracture are also described in that chapter.

# CHAPTER 2

## EXPERIMENTAL

### 2.1 Tensile Specimen Manufacturing

The material used for the aforementioned tensile tests was obtained from McMaster-Carr and came in the form of an 457 x 457 x 3 mm sheet of stainless steel 304. The sheet was able to provide 28 longitudinal, and 2 transverse to the rolling direction specimens, the layout of which can be seen in [Figure 2-1](#). The sheets used were not obtained at the same time and were denoted batches 1-6 to keep any material lot variations grouped together.

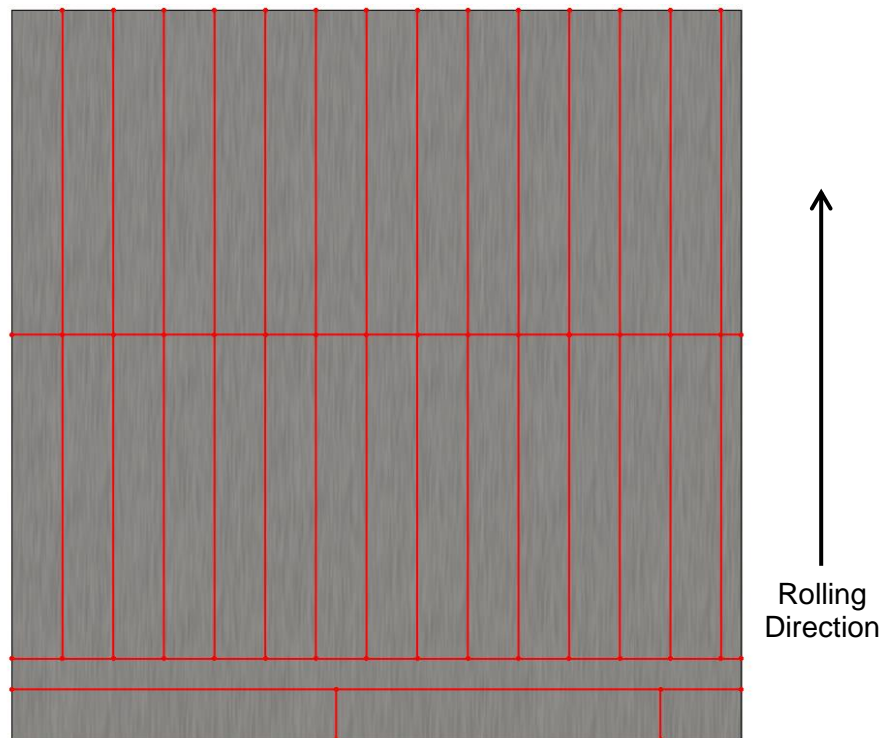


Figure 2-1: SS304 Sheet with coupon layout

In order for the sheets of stainless steel 304 to be used in the uniaxial tensile testing, coupons conforming to the ASTM E8 standard needed to be made. This involved saw-cutting the sheet of SS304 into eight inch long strips, one and one quarter inch wide along the rolling direction of the sheet (

Figure 2-1), deburring and placing them into a custom mill fixture shown in Figure 2-2, with the specimen shown in red.

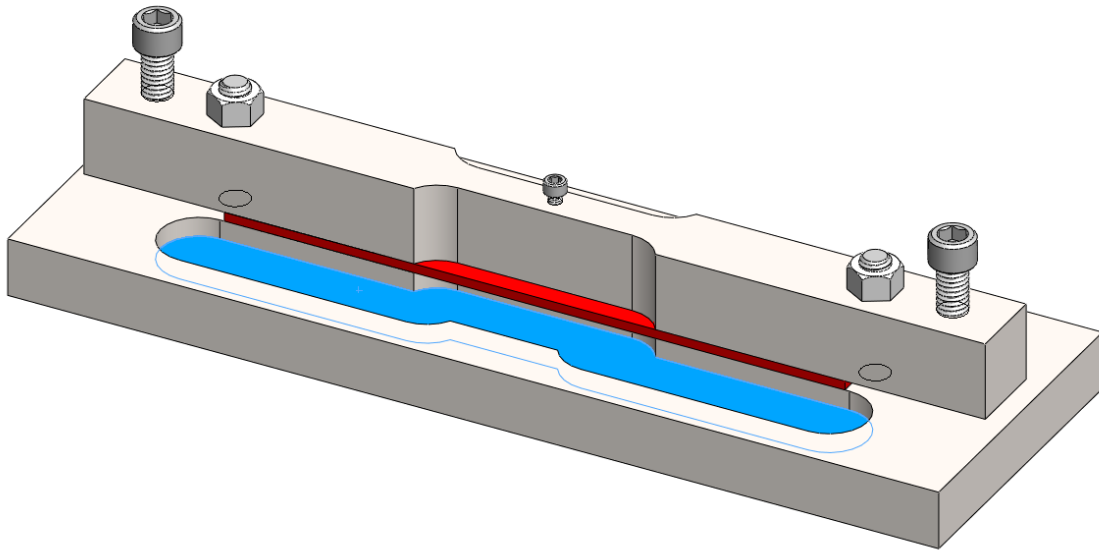


Figure 2-2: ASTM E8 tensile specimen end-milling fixture.

The fixture was designed to clamp the strip of metal with uniform pressure so that chattering of the end mill would be eliminated and no stress raisers would be created in the area of the specimen where plastic deformation occurs. The fixture was placed into a CNC mill, centered and a one inch diameter end mill ran along both sides of the specimen strip following the contour of the fixture shown in blue. Once the milling was complete a light deburring was performed and the specimens visually checked for machining imperfections. If any large variations were present along the gage length (GL) of the specimen, it was discarded. The



specimens were produced in batches to reduce variation, and cataloged by material lot. The final specimen with the extensometer gage length of 40mm is shown in [Figure 2-3](#).

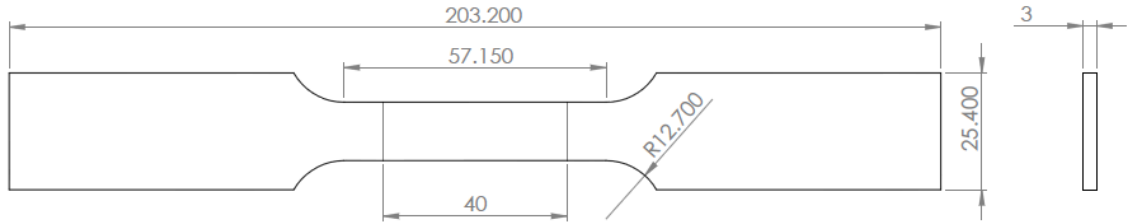


Figure 2-3: ASTM E8 tensile specimen geometry.

## 2.2 Strain Measurements

In order to obtain accurate strain data from tensile testing, the strain across the gage length of the specimen needed to be measured during the tensile test. This is normally accomplished with an extensometer with a gage length of 50 mm as per the standard but for these experiments a non-standard gage length of 40mm was used. This non-standard gage length was dictated by the use of a custom, large strain range mechanical extensometer in preliminary experiments of this type and has been kept constant since. In later experiments the mechanical extensometer was replaced with random pattern of black speckled dots on a white background, applied to one side of the specimen and recorded with a camera during the tensile test. The images were post processed with VIC-2D from Correlated Solutions, Inc. to compute the strain ([Sutton, 2009](#)) at the 40mm gage length throughout the tensile test.

### 2.2.1 Extended Extensometer Arms

The few first tensile tests conducted utilized a standard extensometer with a one inch (25.4 mm) gage length. It was soon discovered that the inherent ductility of the SS-304 was such that the range of the standard extensometer was exceeded and in order to obtain accurate information a modification to the extensometer would be needed. This took the form of

extension arms (Figure 2-4) which would allow for a greater linear motion where they attached to the specimen, but at the cost of added noise.

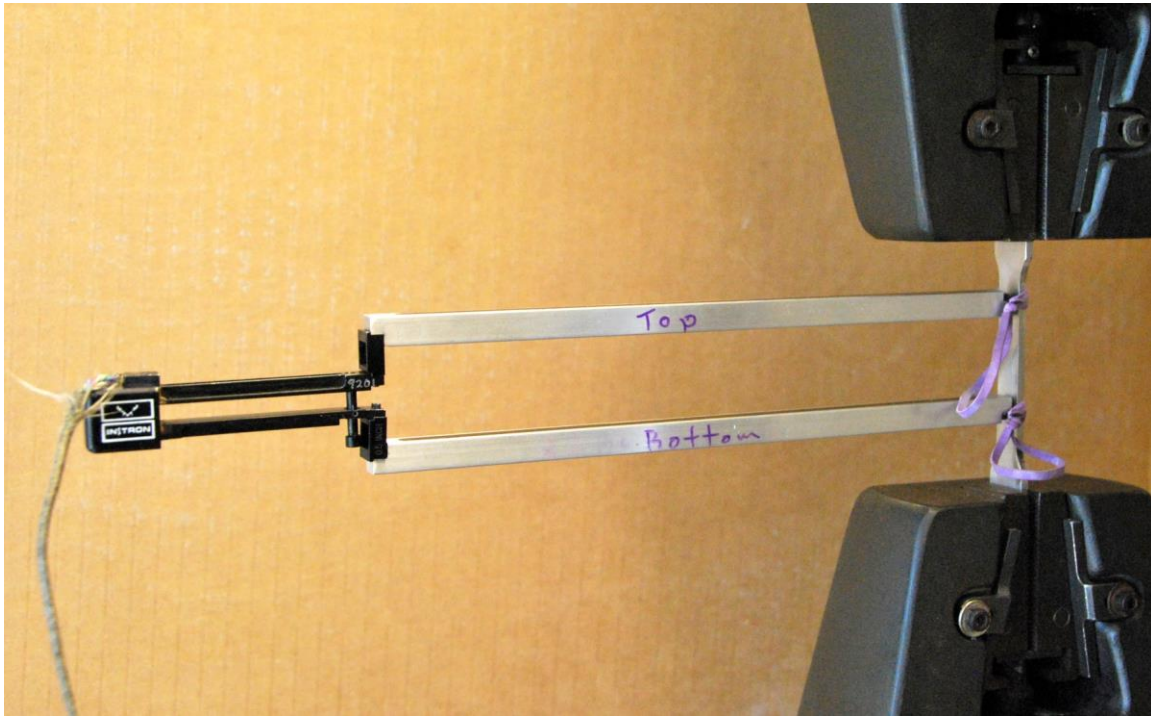


Figure 2-4: Extensometer with extension arms

The length of the arms was designed so that -40% to 90% strain with a gage length of 40 mm could be realized. The final length of the extension arms was 293 mm, and the extensometer recalibrated using a micrometer calibration fixture. The results from the calibration show near perfect linearity (Figure 2-5) and thus the arms were validated for experimental strain measurement.

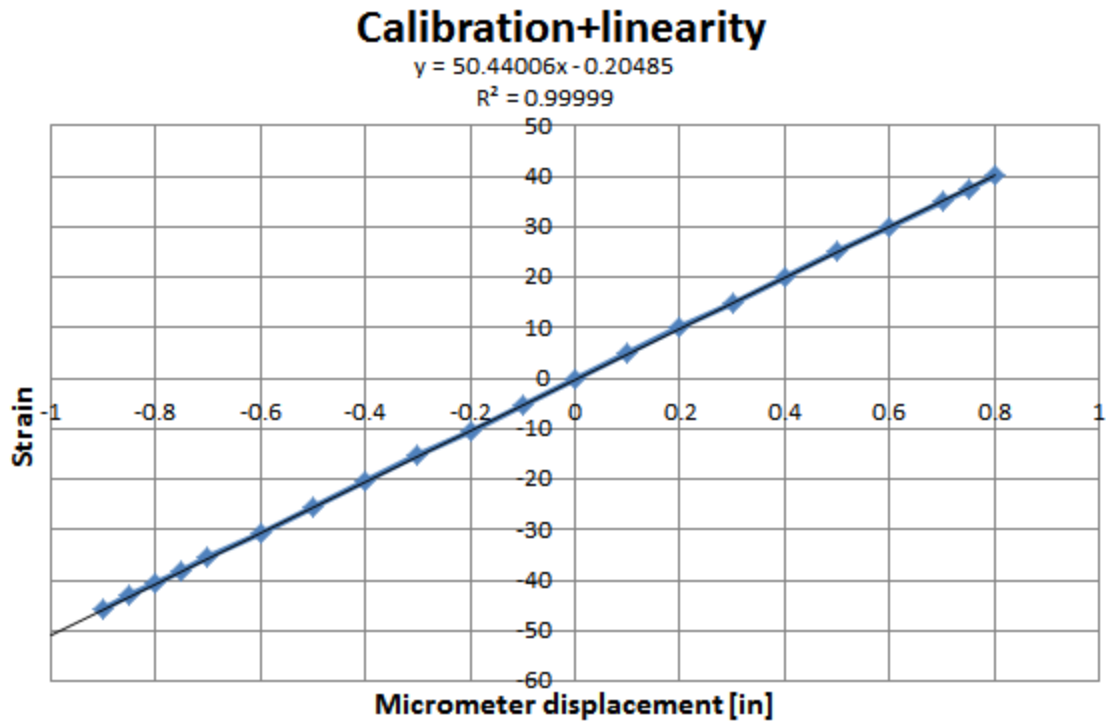


Figure 2-5: Extensometer with extension arm calibration and linearity

The extensometer with the extension arms showed a significant increase in noise shown in [Figure 2-6](#) as the purple line, compared with the standard arms shown in blue. The noise was a result of the vibrations from the hydraulic system in the servo-hydraulic uniaxial load frame used for the experiments. An attempt was made to reduce the noise with the use of increasing arm mass, sprung supports and rubber damping material added to the internals of the extension arms. None of these gave satisfactory solutions and so alternative methods were used to obtain the strain data needed during the tensile test, namely digital image correlation. It should be noted that much after the noise reduction testing discussed here, it was discovered that analog filtering was present on the input from the extensometer to the servo-hydraulic machine that could only be adjusted by the manufacturer and needed to be altered in order to obtain an acceptable noise level.

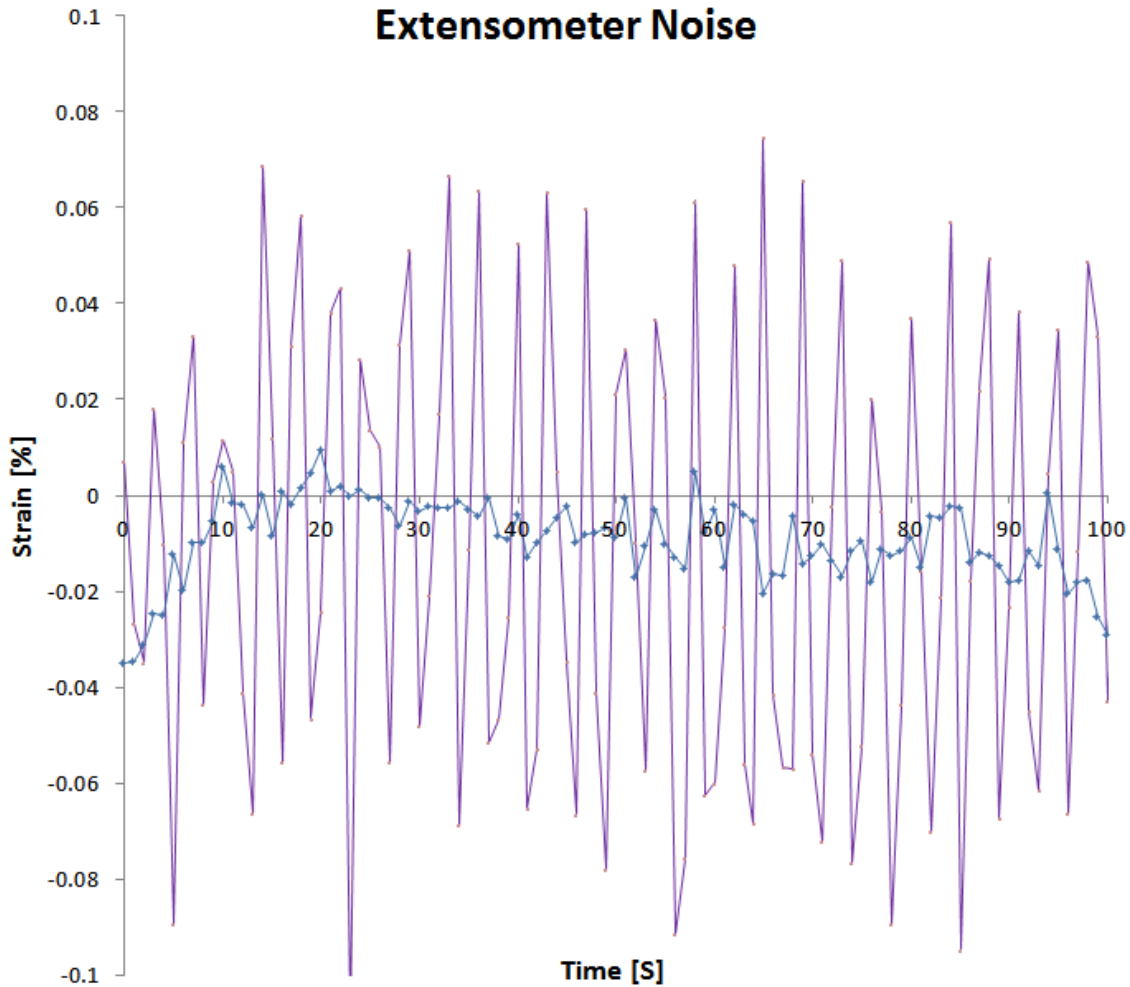


Figure 2-6: Extensometer noise, Blue = w/o extension arms, purple=w/ ext. arms.

### 2.2.2 Digital Image Correlation

Digital image correlation abbreviated to DIC from here on, is the method of using a random pattern of highly contrasting speckles that can be easily and very accurately tracked using software. The DIC system used was VIC-2D from Correlated Solutions, Inc., coupled with the VIC-Snap Image Acquisition software. A single, 2.0 Megapixel digital camera (Point Grey Research, Inc.) with 17 mm Schneider lens was sufficient, as the out-of-plane displacement of the specimens was limited and within the depth of field of that lens. After experimental validation

of the DIC “virtual extensometer” (Chapter 2.2.3), the use of the mechanical extensometer was discontinued in order to simplify the experimental setup and reduce noise. The DIC system is not only able to calculate the strain measured at the 40mm gage length that the mechanical extensometer does, it can also calculate the Green-Lagrange strain field over the entire surface of the specimen (Figure 2-7).

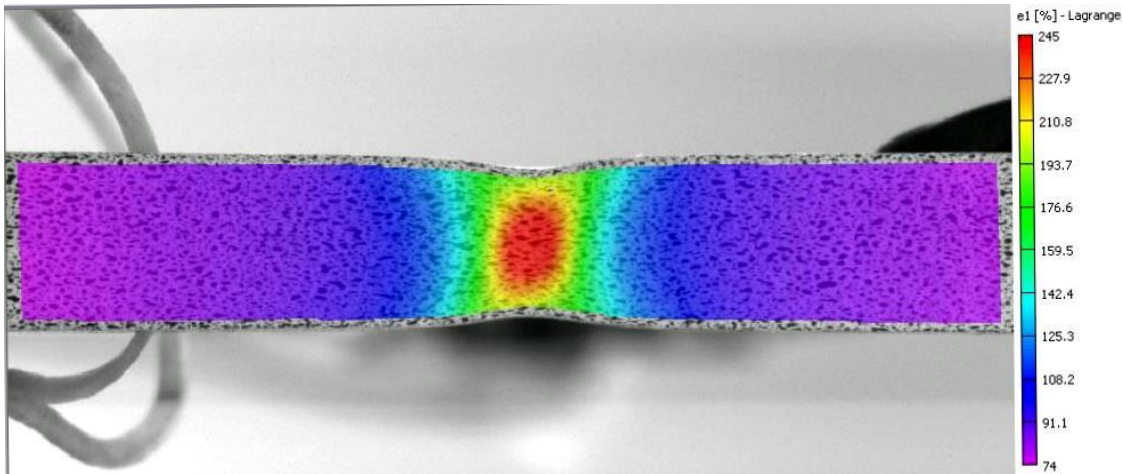


Figure 2-7: Lagrangian major strain field

### 2.2.2.i Painting the specimens

The specimens needed to have a highly concentrated random pattern of dots on their surface, so that the DIC system would be able to calculate the desired strain. Initially the paint used would start to flake off at the higher strains seen in the SS-304, and the strain data would be lost from that point onward. Among the speckling methods tried were white acrylic paint for the background with acrylic black paint or ink used for the speckles, ink alone, ink sprayed from an air brush and finally the use of Rustoleum® specialty high temperature paint. The high temperature paint does not cure to a smooth shiny finish like normal paint and will not flake off at the high strains (>70%), seen in the SS304.

The finish-machined and deburred specimens were first cleaned with acetone and a paper towel to remove any oils or particles that may prevent the adhesion of the paint. Without touching the prepared surface, the specimen was placed in an area designed for spray painting and a uniform layer of white spray paint applied according to the manufacturer's directions. Once the white paint had dried, the black paint was sprayed on with very light pressure being applied to the spray nozzle. This created a fine spray of black that when applied in a fast sweeping motion created a random and yet fairly uniform speckle pattern (Figure 2-8).

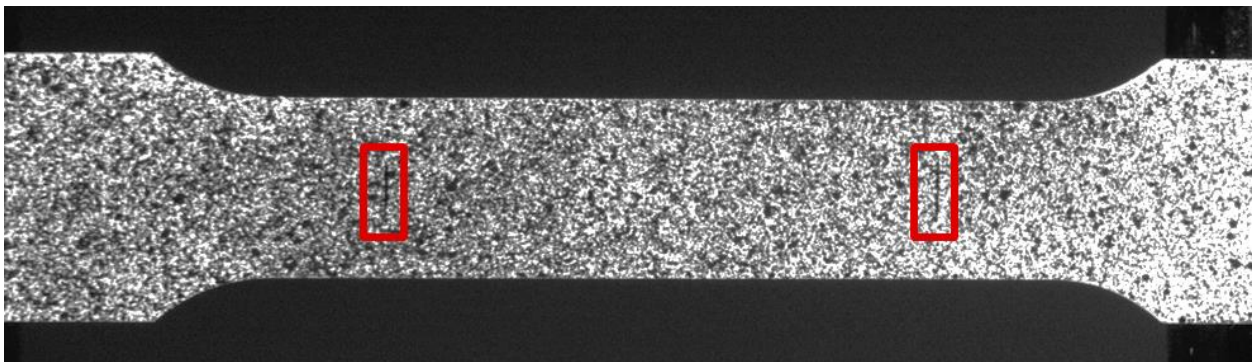


Figure 2-8: Tensile specimens prepared for DIC with extensometer line outlined in red

Once the specimens had fully dried they were ready for use, except that without a calibration scale in the image the 40mm gage length needed could not be accurately determined. An easy way to overcome this issue, was to scribe 0.2mm lines onto the center of the gage length of the specimen using a pair of calipers, and a mechanical drafting pencil. These marks are small enough to no disturb the strain calculation during post processing, but are large enough to be easily recognizable in the post processing software (Figure 2-8).

### 2.2.2.ii DIC Camera Setup

The camera used for the DIC measurements was a single, 2.0 Megapixel digital camera (Point Grey Research, Inc.) with 17 mm Schneider lens, which was mounted to the servo-hydraulic machine. The camera was mounted to be normal to the surface of interest on the



tensile specimen, and focused to produce the largest reasonable depth of field. This was accomplished by illuminating the tensile specimen with two 125 Watt halogen spot lamps, setting the aperture of the lens to be fully open and reducing the exposure time in VIC-Snap Image Acquisition software until the contrast on the speckle pattern could be easily seen. A section in the middle of the tensile specimen was selected and magnified in VIC-Snap, and the aperture opened all the way. This had the effect of minimizing the depth of field to make it easy to find the optimal focus. The focus was then adjusted until the image was as clear as possible. The aperture was then closed down 90% of the way and the exposure increased until just below the saturation point of the imaging sensor. Using this procedure will set the focus in the center of the depth of field, and keep the specimen in focus as its thickness is decreasing with strain.

### *2.2.2.iii DIC VIC-2D Software*

While the VIC-Snap software is used to acquire the images and force data from the servo-hydraulic machine during testing, VIC-2D is used to process the images and output the strain data. A typical reference image for the strain calculation is shown in [Figure 2-9](#).

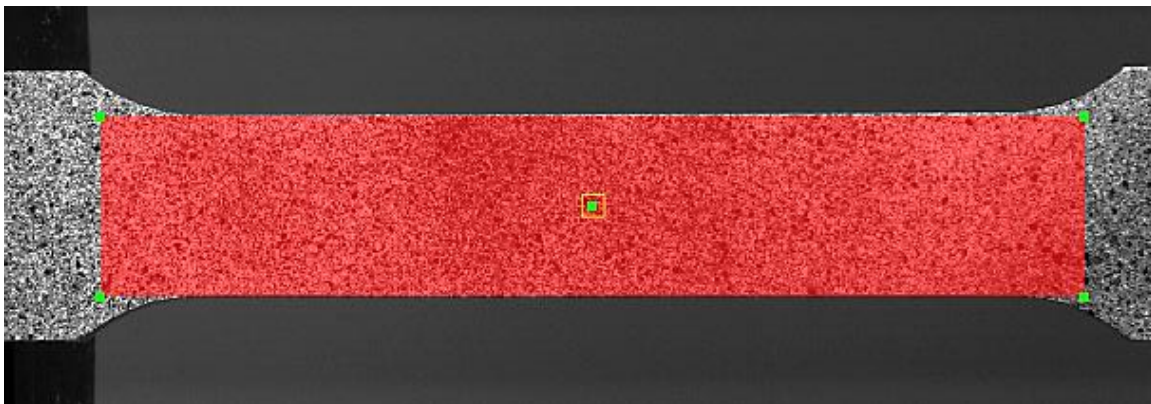


Figure 2-9: VIC-2D reference image

Since the VIC-2D software can only track the pixels in the speckled image, a reference image must be selected that represents the initial state of the specimen. The software also needs to have a defined area in which the strain information is to be calculated, this area is highlighted in red in [Figure 2-9](#). The software will use the reference image to calculate the new pixel location for each pixel in the selected region and for each subsequent image. Now that each pixel's original and final locations are known, the software is able to calculate various strain tensors for each pixel and can combine each of those pixels into a strain field. An example of this can be seen in [Figure 2-7](#), where the specimen is about to break. The Lagrangian strain field that is output from the VIC-2D software cannot be easily resolved into engineering strain and compared with the previous results using the mechanical extensometer. The VIC-2D software has a virtual extensometer function which can be used in place of the mechanical extensometer by placing the inspect extensometer line between the 40 mm gage lines already scribed on the tensile specimen, as shown in [Figure 2-10](#).

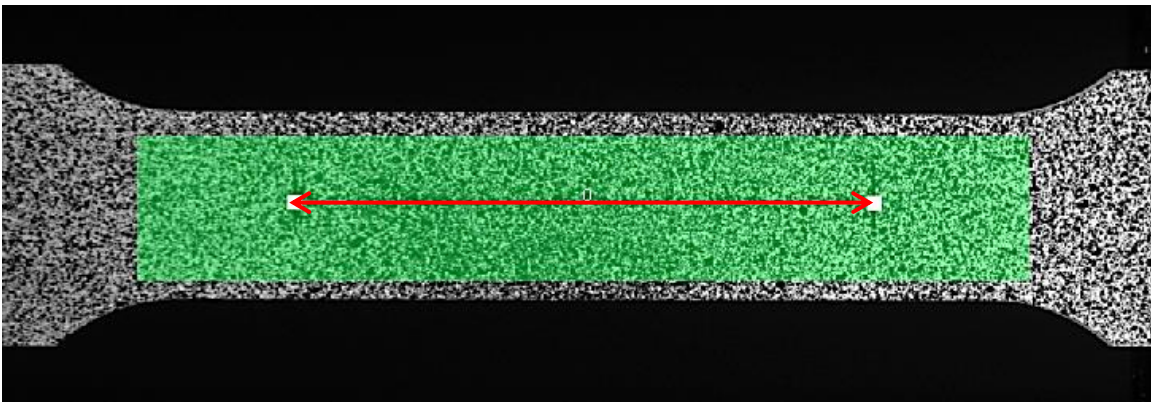


Figure 2-10: Virtual extensometer line

### 2.2.3 Validating DIC Strain Data

The data obtained from the DIC system needed to be validated for both the strain field and the virtual extensometer. This was done with a series of experiments that were instrumented



with both the mechanical extensometer, speckled specimen with DIC camera, and precision scribed lines (described later in this section) and DIC camera. The results were compared and the DIC data determined to be accurate and consistent.

### *2.2.3.i Scribed Lines, DIC and Mechanical Extensometer*

The comparison of the virtual extensometer created using VIC-2D to that of the mechanical extensometer was a simple matter and a number of experiments were performed to validate it. A sample of this comparison can be seen in (Figure 2-12) from experiment SS-37 where two cameras simultaneously captured the speckled side of the specimen used for DIC and the back side of the specimen where precision scribed lines (Chapter 2.2.3.ii) were placed (Figure 2-13).

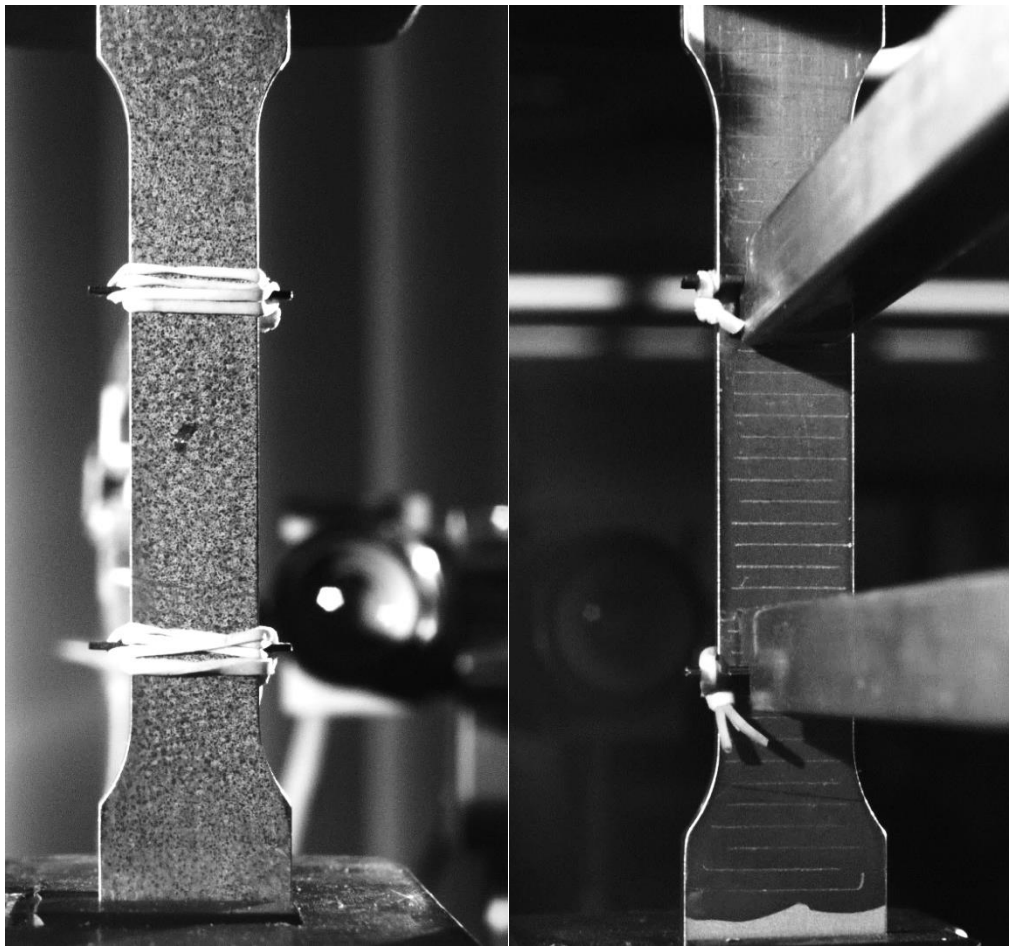


Figure 2-11: a) DIC speckles and extensometer knife edge rubber bands and, b) traditional extensometer extended arms and scribed lines 2mm apart

The mechanical extensometer was attached to the specimen on the back side, and all the data was recorded. The mechanical extensometer covered the specimen at the 40mm gage length used for the strain calculations, thus the scribed lines and DIC extensometer used a smaller gage length. Since for the majority of the experiment the strain is uniform across the specimen, the comparison can be made for smaller values of strain; but as the strain field along the specimen becomes non-uniform at higher strain values the engineering strain will be lower for a larger initial gage length. The plot in [Figure 2-12](#) shows that the strain measured by the DIC extensometer is virtually identical to the mechanical extensometer for smaller values of strain but starts to deviate past 20% strain. The strain lines were measured for a number of images and the strain totaled for approximately the same gage length as used by the DIC extensometer and are shown as points on the plot. These points perfectly follow the DIC extensometer indicating that although the mechanical extensometer deviates due to non-uniform strain above 20%, the values obtained as accurate.

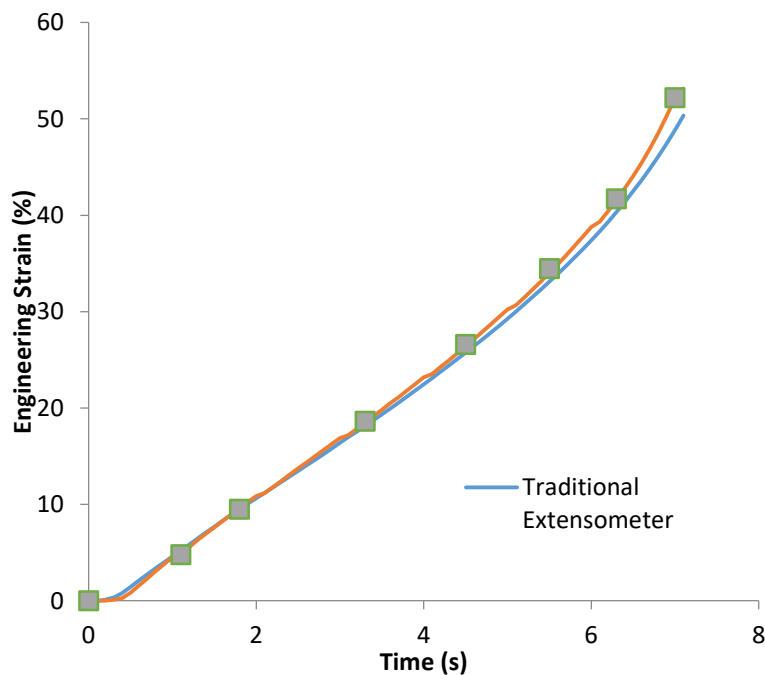


Figure 2-12: Comparison of scribed strain lines, DIC extensometer and traditional extensometer (with extension arms)

### 2.2.3.ii DIC Strain Field versus Scribed Lines

The DIC systems can output full field strain data over the observed surface of the specimen, and a simple validation of this data was conducted. Blue layout fluid was applied to the back side of the specimen, and a needle placed into a CNC mill chuck was used to scribe lines exactly 2mm apart along the entire gage length of the specimen (Figure 2-11).

The scribed lines were recorded during the test so that they could be compared with the DIC output data. Note that the DIC system used reports Lagrangian strains (Figure 2-7), but these can be routinely converted to engineering strains. Denoting the position vector of a material point in the undeformed configuration with respect to the material coordinate system as  $\mathbf{X}$ , the displacement vector as  $\mathbf{u}$  and the deformation gradient as  $\mathbf{F}$ , the Green-Lagrange strain tensor  $\mathbf{E}$  is defined as (Bower, 2009):

$$\mathbf{E} = \frac{1}{2}[\mathbf{F}^T \mathbf{F} - \mathbf{I}] \quad (2.1)$$

This can be further expressed in Cartesian component form as:

$$\mathbf{E} = \frac{1}{2} \left[ \frac{\partial \mathbf{u}}{\partial \mathbf{X}} + \left( \frac{\partial \mathbf{u}}{\partial \mathbf{X}} \right)^T + \left( \frac{\partial \mathbf{u}}{\partial \mathbf{X}} \right)^T \frac{\partial \mathbf{u}}{\partial \mathbf{X}} \right] \quad (2.2)$$

Assuming that the 1-axis is along the specimen (x-axis in Figure 2-13), expanding Eq. (2.2) for the 1-1 term and noting that before the onset of necking following Eq. (2.3)

$$\partial u_2 / \partial X_1 = \partial u_3 / \partial X_1 = 0 \quad (2.3)$$

we obtain:

$$E_{11} = \frac{\partial u_1}{\partial X_1} + \frac{1}{2} \left( \frac{\partial u_1}{\partial X_1} \right)^2 \quad (2.4)$$

so that the Lagrangian and the engineering strain along the loading axis are ultimately related by (Sutton, 2009):

$$\varepsilon_x := \varepsilon_{11} = \sqrt{1 + 2E_{11}} - 1 \quad (2.5)$$

Note that this conversion holds only for uniform deformations, due to Eqns. (2.3), hence the post-necking strains described in subsequent chapters should be viewed as approximately correct.

The strain data from SS-29 was extracted using DIC along the specimen at the end of the experiment, just before failure. The resulting Lagrangian strain was converted to engineering strain using equation 2.5, and is shown in Figure 2-14 in blue. On the back side of the specimen, the scribed lines (Figure 2-13) were measured and the resulting engineering strain was calculated and is shown in Figure 2-14 in red. The slight deviation at the center of the specimen is due to the non-uniform strain as discussed previously.

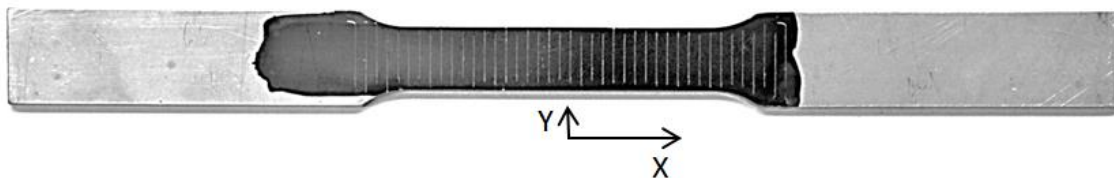


Figure 2-13: Specimen with scribed lines 2mm apart

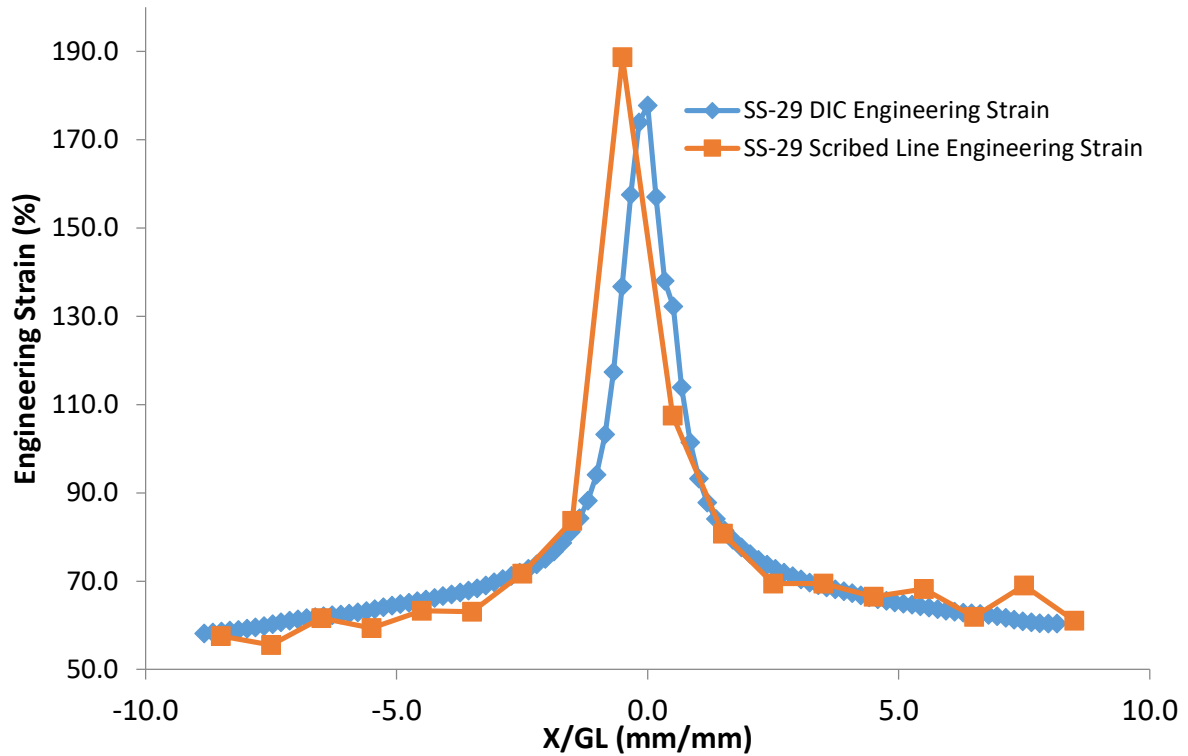


Figure 2-14: DIC and scribed line engineering strain (SS-29)

### 2.3 Iso-Thermal Setup

For the numerical simulations described in [CHAPTER 4](#), it is necessary to decouple the mechanical from the thermal response of the material. A specialized and simple isothermal tension experiment was devised for that purpose. In this experiment, a copper heat exchanger was clamped at the stationary end of the specimen and attached to the back of it with thermal grease (*Arctic Silver® 5*) in between, as shown in [Figure 2-15](#).

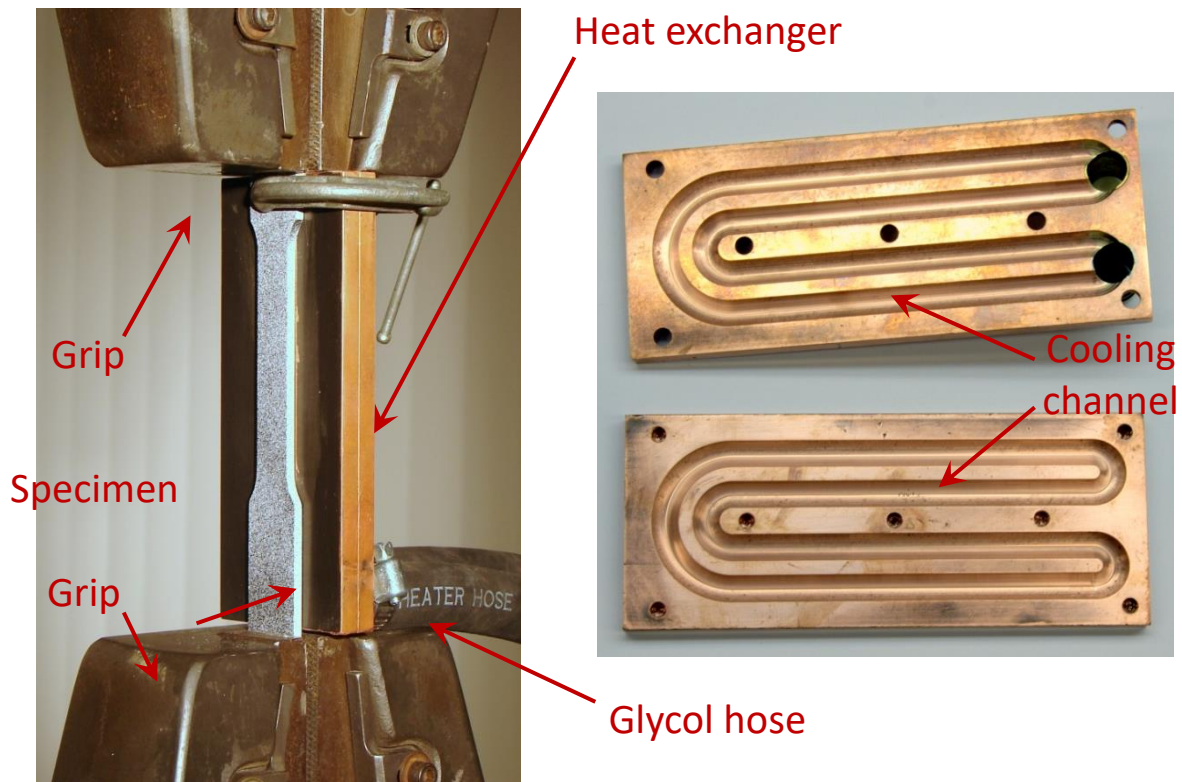


Figure 2-15: Heat exchanger attached to specimen, and the internals of the heat exchanger

The heat exchanger was made from two 120mm x 50.8mm pure copper bars, which had 6.25 mm wide and 3.125 mm deep circular profile cooling channels milled into one of their sides, as shown in the right image in [Figure 2-15](#). Clearance and tapped holes were added to allow the two bars to be fastened together producing two 6.25 mm dia. round cooling channels. At the end of the cooling channels on one of the copper bars, feed and return holes were added and AN-6 male fittings brazed into them. Static mixers ([Figure 2-16](#)) which force the fluid to rapidly alternate rotational direction causing high turbulence where initially added to the cooling channels to aid in the heat transfer between the temperature controlled liquid and the copper. It was soon discovered that they were not needed as the fluid velocity from the constant

temperature bath was sufficient to keep the copper at a constant temperature as shown in Figure 2-18.



Figure 2-16: Static mixer initially used to induce turbulent flow in the cooling channels of the heat exchanger

Thermal grease (*Arctic Silver® 5*) which mainly consists of micronized silver particles suspended in polysynthetic oils was used between the specimen and the heat exchanger to ensure good thermal conductivity even as the specimen thinned-down during plastic deformation. The grease also allowed the tensile specimen to easily move against the heat exchanger so that the material response was not affected.

The heat exchanger was connected to a Neslab RTE 740 constant temperature bath with a temperature range of -40 to 200 °C. When the testing required temperatures from 0 to 100 °C, a 50% by volume solution of ethylene glycol (*Zerex® G05*) and water was the heat transfer medium. If temperatures over 100 °C were needed, pure mineral oil (*Animed®*) was circulated as the heat transfer medium. The heat exchanged is quite simple but very effective and in addition leaves one of the two wide sides of the specimen unobstructed, which is needed for the DIC and IR measurements. The entire iso-thermal setup including the servohydraulic load frame, DIC and thermal imaging cameras, heat exchanger and constant temperature bath are shown in [Figure 2-16](#).



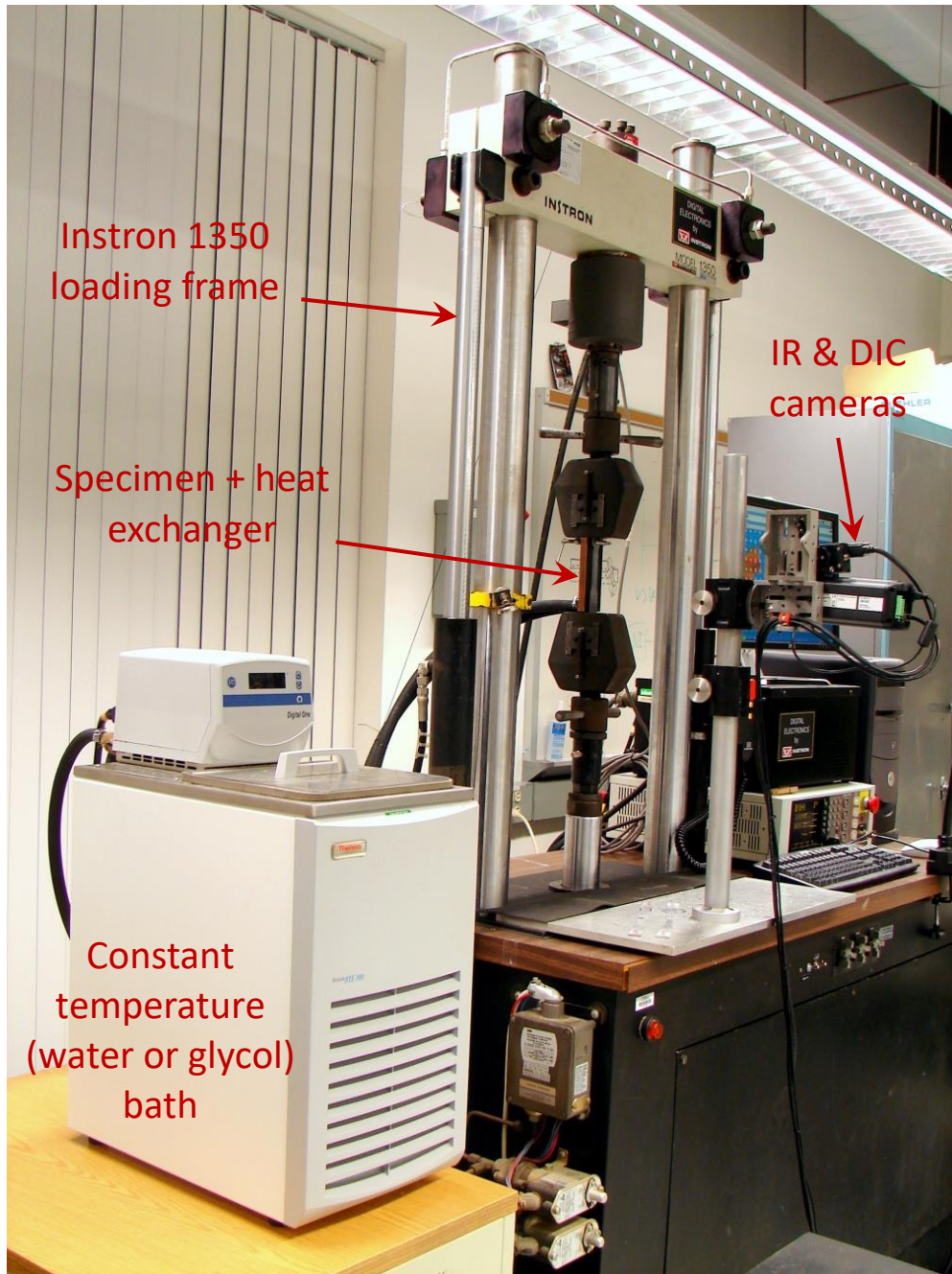


Figure 2-17: Iso-thermal tensile testing



## 2.4 Thermal Imaging Camera

The same side of the specimen that was used for DIC analysis was also used for Infrared Thermography (IR) temperature measurement (Maldague, 2001). A FLIR SC-645 infrared camera, with a range of  $-20\text{ }^{\circ}\text{C}$  to  $650\text{ }^{\circ}\text{C}$ , temperature resolution of  $0.05\text{ }^{\circ}\text{C}$  and spatial resolution of  $640 \times 480$  pixels was used for these measurements. In order to establish that the emissivity variation of the black and white painted surface did not noticeably influence the thermal imaging, the heat exchanger used for the isothermal tests was painted with the same black and white paint as the tensile specimens. Instead of the speckle arrangement used for DIC, the left half of the heat exchange was painted with only white paint and the right side with only black (Figure 2-18). A prepared tensile specimen was placed into the load frame, thermal grease applied to the back of the specimen, and the heat exchanger clamped in place. The calibrated temperature bath was brought to  $30\text{ }^{\circ}\text{C}$ , and several thermal images taken (Figure 2-18). A temperature profile line was taken from the thermal image, marked line one in Figure 2-18, and the resulting temperature profile shown in the graph in Figure 2-18. It can be seen that the white paint had a slightly higher temperature reading of around  $30.1\text{ }^{\circ}\text{C}$  while the black had a slightly lower temperature reading of  $29.8\text{ }^{\circ}\text{C}$ , with the tensile specimen reading approximately  $30\text{ }^{\circ}\text{C}$ . This noise is on the order of 0.1 degrees, so it can be concluded that the emissivity of the paint is approximately 0.95 and the results obtained from the camera are accurate within two tenths of a degree.

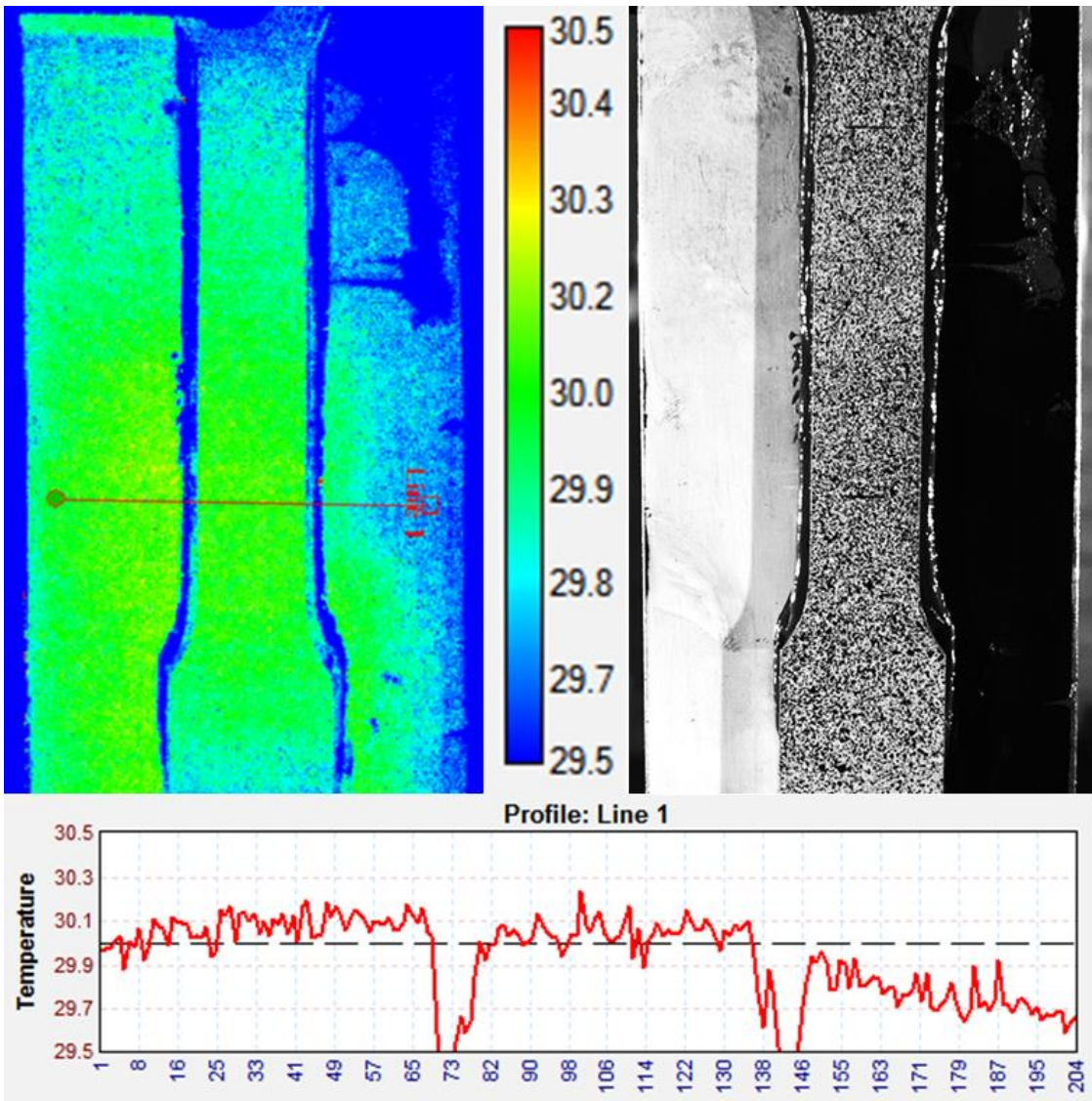


Figure 2-18: Iso-thermal temperature validation, experiment # SS-97

# CHAPTER 3

## MATERIAL BEHAVIOR

### 3.1 Stress Strain Curves

The experiments were carried out under displacement control for a variety of strain-rates (crosshead velocities) using a standard, 100 kN servohydraulic testing machine (Instron 1350 with a FastTrack 8800 controller and data acquisition system). Four types of uniaxial experiments were performed: standard monotonic (termed “master”), pulsed, hold and equal time monotonic, as detailed in the following sections.

For a given strain-rate (crosshead velocity), a monotonic master experiment was performed first. This was followed by a pulsed experiment: the crosshead velocity was kept the same as in the master monotonic experiment, but after the crosshead had been displaced by 6.35 mm or approximately 7% strain, the specimen was manually unloaded to around 70 N or 2 MPa (in order to avoid the load train from becoming slack). The ~7% strain limit was chosen to correspond to approx. 1/10 of the elongation-to-fracture of SS-304 under monotonic testing. This procedure was then repeated, requiring eight to eleven such strain pulses to fail the specimen ([Table 1](#)). The time that was required to unload the specimen, prepare the next pulse and reload to a stress level comparable to that just before unloading, led to the pulsed experiments lasting significantly longer than the associated master monotonic ones (i.e., those performed under the same crosshead velocity). For example, the  $\dot{\epsilon} = 10^{-3}$  /s master monotonic experiment lasted for 858 s, while the corresponding pulsed experiment lasted for 2472 s. [Table 3-1](#) details these time differences for a variety of experiments performed.

#	Specimen	Batch #	Strain Rate [s <sup>-1</sup> ]	Experiment Type	# Pulses	Experiment Duration [s]	$\epsilon_{\text{uts}}$ [%]	$\sigma_{\text{uts}}$ [MPa]	$\epsilon_f$ [%] (GL=40mm)
1	SS-41	4	5 x 10 <sup>-2</sup>	Monotonic	1	14	38	688	53
2	SS-42	4	5 x 10 <sup>-2</sup>	Pulsed	8	142	---	---	52
3	SS-46	4	5 x 10 <sup>-2</sup>	Hold	8	159	---	---	52
4	SS-44	4	5 x 10 <sup>-2</sup>	Equal time	1	141	41	678	52
5	SS-17	2	10 <sup>-2</sup>	Monotonic	1	66	38	645	49
6	SS-18	2	10 <sup>-2</sup>	Pulsed	9	246	---	---	56
7	SS-20	2	10 <sup>-2</sup>	Hold	9	390	---	---	57
8	SS-22	2	10 <sup>-2</sup>	Equal time	1	378	49	662	56
9	SS-10	1	10 <sup>-3</sup>	Monotonic	1	858	50	714	60
10	SS-9	1	10 <sup>-3</sup>	Pulsed	10	2472	---	---	70
11	SS-31	1	10 <sup>-3</sup>	Hold	10	2481	---	---	70
12	SS-15	1	10 <sup>-3</sup>	Equal time	1	2730	61	717	71
13	SS-23	2	4 x 10 <sup>-4</sup>	Monotonic	1	2123	62	666	70
14	SS-27	2	4 x 10 <sup>-4</sup>	Pulsed	11	3665	---	---	74
15	SS-32	2	4 x 10 <sup>-4</sup>	Hold	11	3757	---	---	75
16	SS-29	2	4 x 10 <sup>-4</sup>	Equal time	1	3606	56	665	70
17	SS-52	3	1 x 10 <sup>-4</sup>	Monotonic	1	10495	61	721	75
18	SS-53	3	1 x 10 <sup>-4</sup>	Pulsed	11	14772	---	---	75
19	SS-57	3	1 x 10 <sup>-4</sup>	Hold	11	15242	---	---	74

Table 3-1: Representative Experiments

For the experiments shown (Figure 3-1), the pulsed test showed significantly greater elongation-to-fracture than the master monotonic test (69.7% and 60%, respectively for  $10^{-3}$  strain rate). This seems to contrast the common notion that unloading and reloading during a uniaxial tension experiment does not affect the stress – strain response recorded. Indeed, it is this apparent discrepancy as observed earlier on SS-304 (Zhang, 2009) that prompted the present work. To investigate whether this behavior is due to the repeated loading and unloading, “hold” experiments were performed. In these experiments, after the end of each strain pulse, the crosshead displacement was held constant for the same amount of time as was required for the unloading and reloading in the corresponding pulsed experiment to take place. The next strain pulse was then applied. By way of construction, these experiments lasted approximately the same amount of time as the pulsed ones (2472 s for the pulsed and 2481 s for the hold experiment in Figure 3-1). As is evident in Figure 3-1, relaxation of the material was observed as a result of holding the displacement constant under load. More remarkably however, for the data shown in Figure 3-1, the elongation-to-fracture measured at the hold experiment was identical to that of the pulsed experiment. Hence the increase over the master monotonic case cannot be contributed to the unloading and reloading of the specimens.

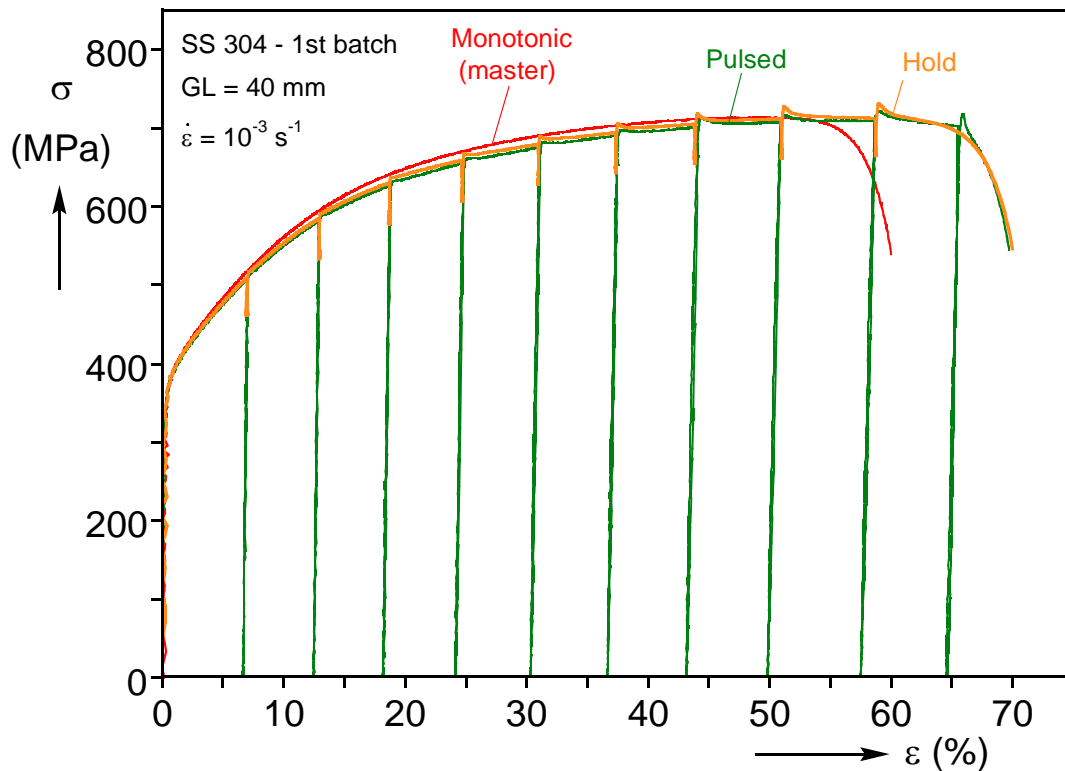


Figure 3-1: Stress–strain responses of 304 stainless steel

These experiments were repeated for a range of strain-rates (i.e., crosshead velocities of the monotonic experiments) and the results are shown cumulatively in [Figure 3-2](#). For a given strain-rate (crosshead velocity), the pulsed and the hold experiments always exhibited approximately the same elongation-to-fracture. For a range of strain-rates, these elongations were distinctly different from those measured from the associated monotonic experiments. Interestingly, this phenomenon is erased by either sufficiently increasing or decreasing the strain-rate.

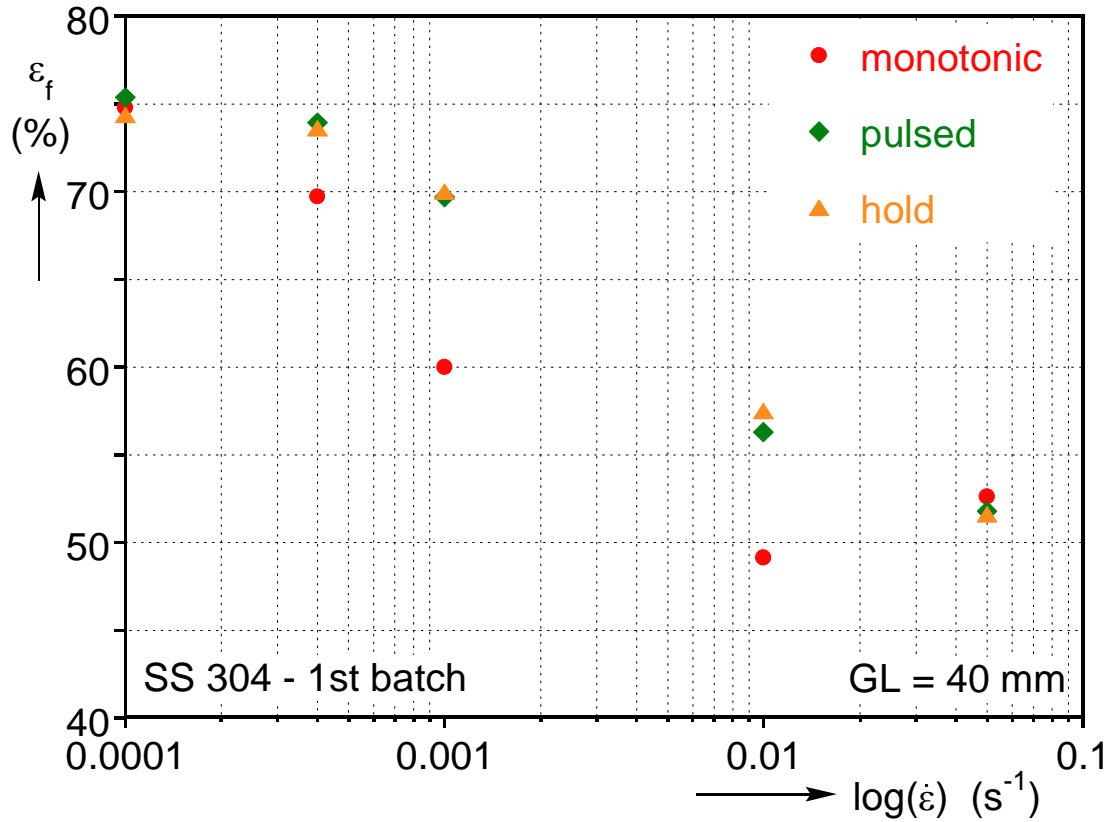


Figure 3-2: Strain-rate dependence of elongation to fracture

The DIC and IR tools were used to probe this behavior and a sample of the DIC measurements are shown in [Figure 3-3](#). The evolution of strain along the gage length is shown in [Figure 3-3b](#) and exhibits the typical behavior of a localization problem: up to the onset of necking, the strain distribution is spatially uniform and equal to the overall normalized elongation  $\delta/L$ . Beyond that point, the deformation localizes at a narrow region and the rest of the specimen unloads elastically. It should be noted that the local values of strain inside the neck ([Figure 3-3b](#)), exceed 120%.

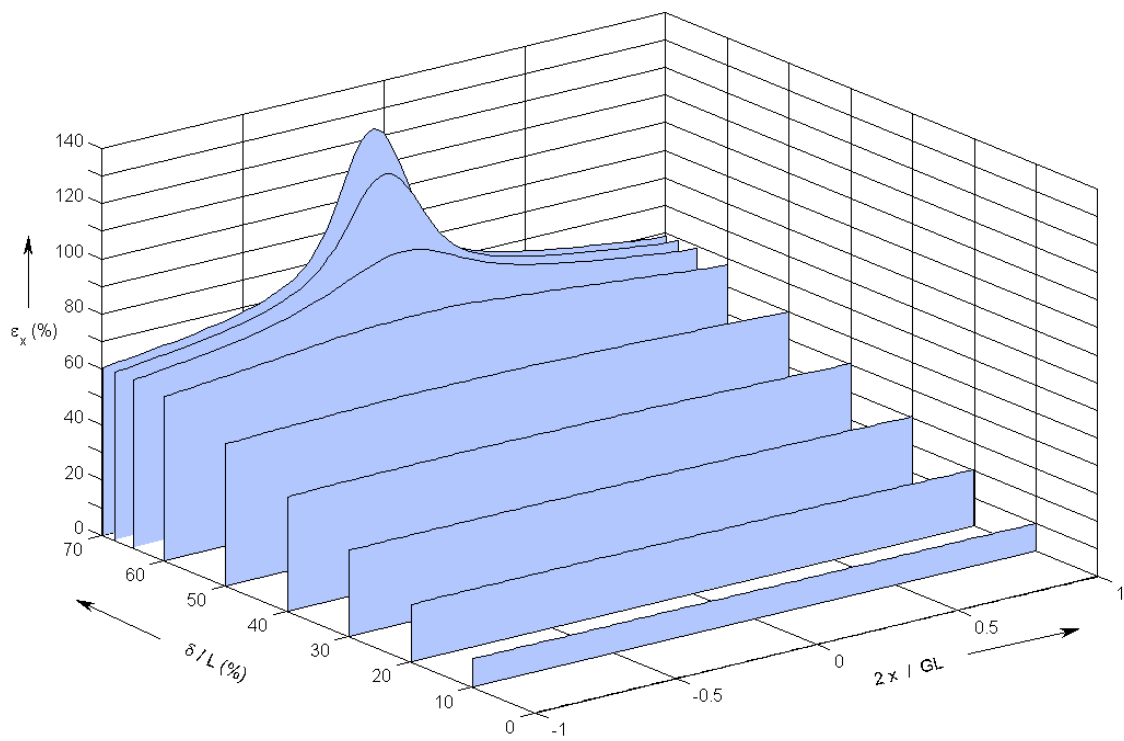
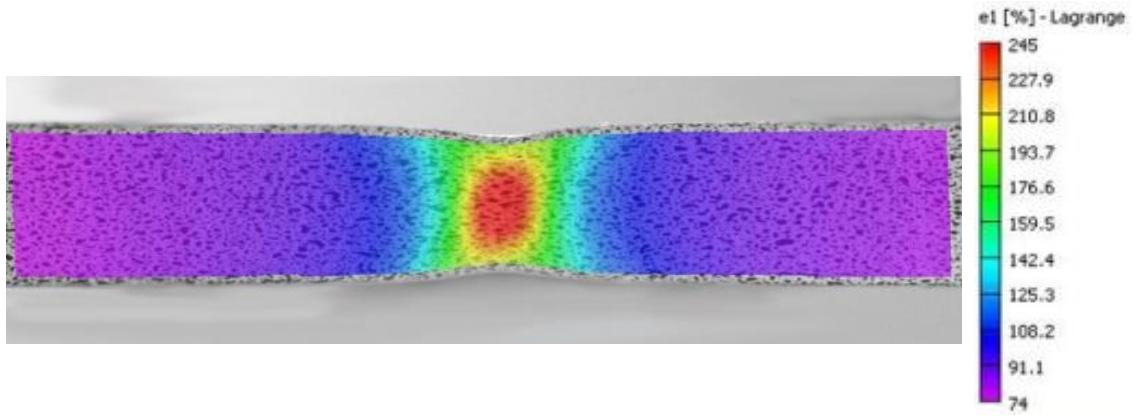


Figure 3-3: a) Lagrangian strain field SS-29, b) Strain evolution along gage length at different overall deformation.



Another phenomenon that was observed during the pulsed and the hold experiments is strain aging. This was manifested by the overshooting of the stress-strain response during reloading (Figure 3-4). The response then returned to the fundamental, monotonic behavior. The overshooting is associated with breaking the energetic barrier for unpinning the dislocations from the interstitial atoms that have surrounded and locked them during the previous unloading (Meyers, 1998). Strain aging is known to be affected by the specimen temperature. Indeed, as the plastic deformation accumulated and the specimen temperature increased, the strain aging was accentuated (Figure 3-4).

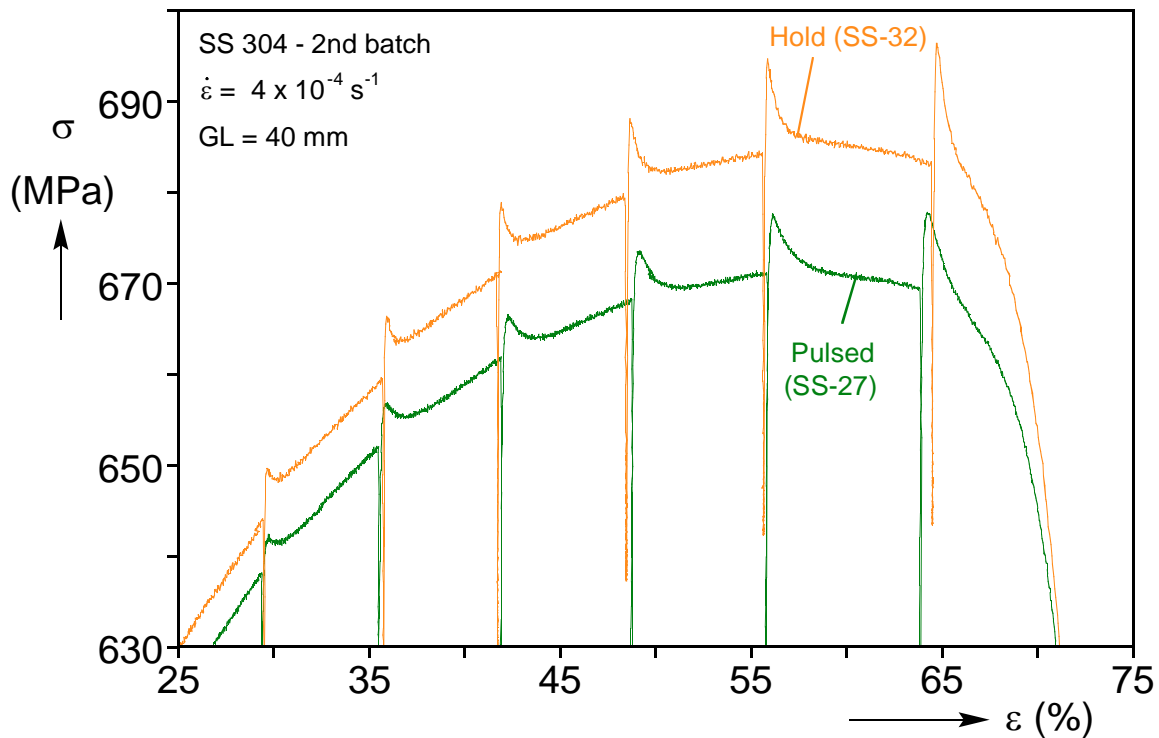


Figure 3-4: Strain aging of stainless steel 304

The temperature evolution inside the specimen was assessed by IR measurements and is shown in Figure 3-5 for a relatively slow ( $\dot{\epsilon} = 10^{-3}$  /s) monotonic experiment. During plastic deformation, the majority of mechanical work is converted into heat (typically, 86.5% for steel

and 93% for aluminum, (Farren & Taylor, 1925)). For the problem at hand, the main mechanism of heat transfer is by conduction through the gage length to the metal grips. (Notice from Figure 3-5 that due to the relatively large thermal mass of the grips, these remained relatively unaffected by the heating of the specimen throughout the experiment.) By comparison, convection to the still surrounding air and radiation are both negligible (Farren & Taylor, 1925). Furthermore, stainless steel is known to have very limited thermal conductivity in comparison to many other metals and alloys ( $k = 16.2$  W/m-K, while carbon steels can have  $k > 50$  W/m-K and aluminum alloys  $k > 200$  W/m-K). As a result of these reasons, the center of the specimen progressively became distinctly warmer than the gripped ends, i.e., a temperature gradient was established along the gage length. This gradient has been shown to promote local softening and thus to trigger a premature localization of deformation in comparison to an idealized, isothermal case (Wagoner). Notice from Figure 3-5 that even in a slow monotonic experiment such as the one shown, the increase in temperature at the center of the specimen is around 35 °C at the onset of necking. The dominance of heat effects on the recorded responses is also indicated by the fact that all specimens failed at or very close to mid-span, which is the warmest region in the specimen.

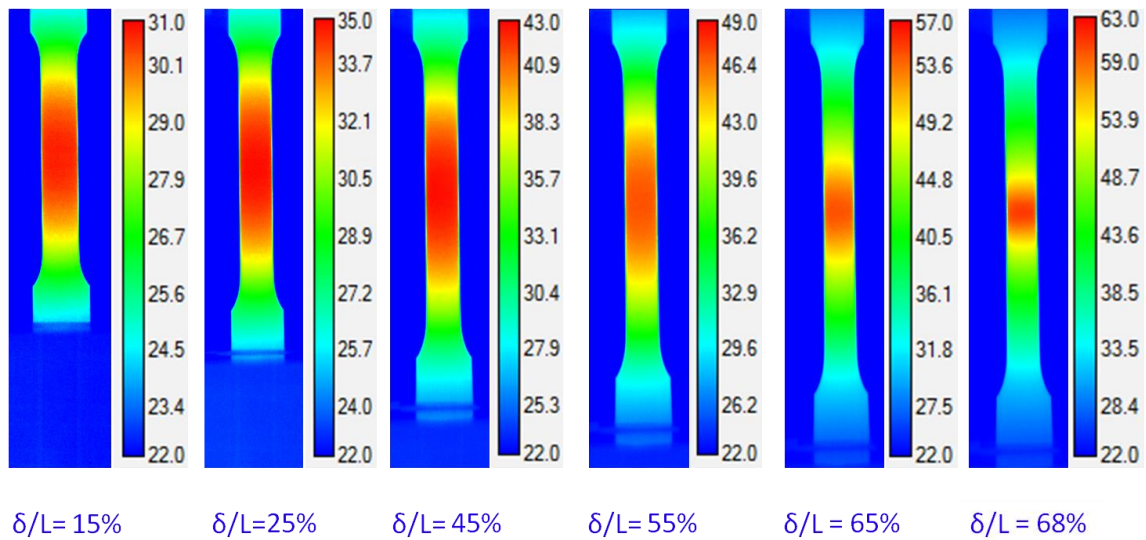


Figure 3-5: Temperature development in the tensile specimen during monotonic testing

In order to establish whether it is the strain or the temperature localization that preceded the other, the DIC and IR measurements are compared in [Figure 3-6](#) at equal levels of overall normalized elongation  $\delta/L$ . Comparing the two fields at  $\delta/L = 40\%$ , it can be seen that while no visible necking is present, the center of the specimen is already 7-9 °C warmer than the gripped ends. Hence, necking was triggered by the temperature and not vice versa.

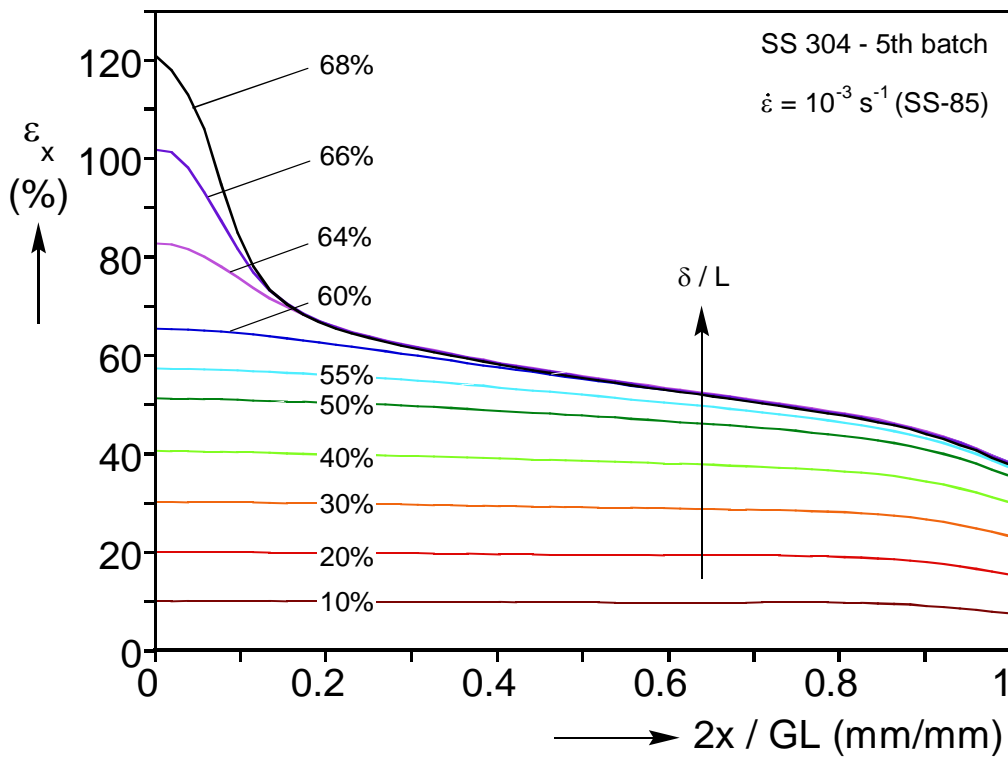
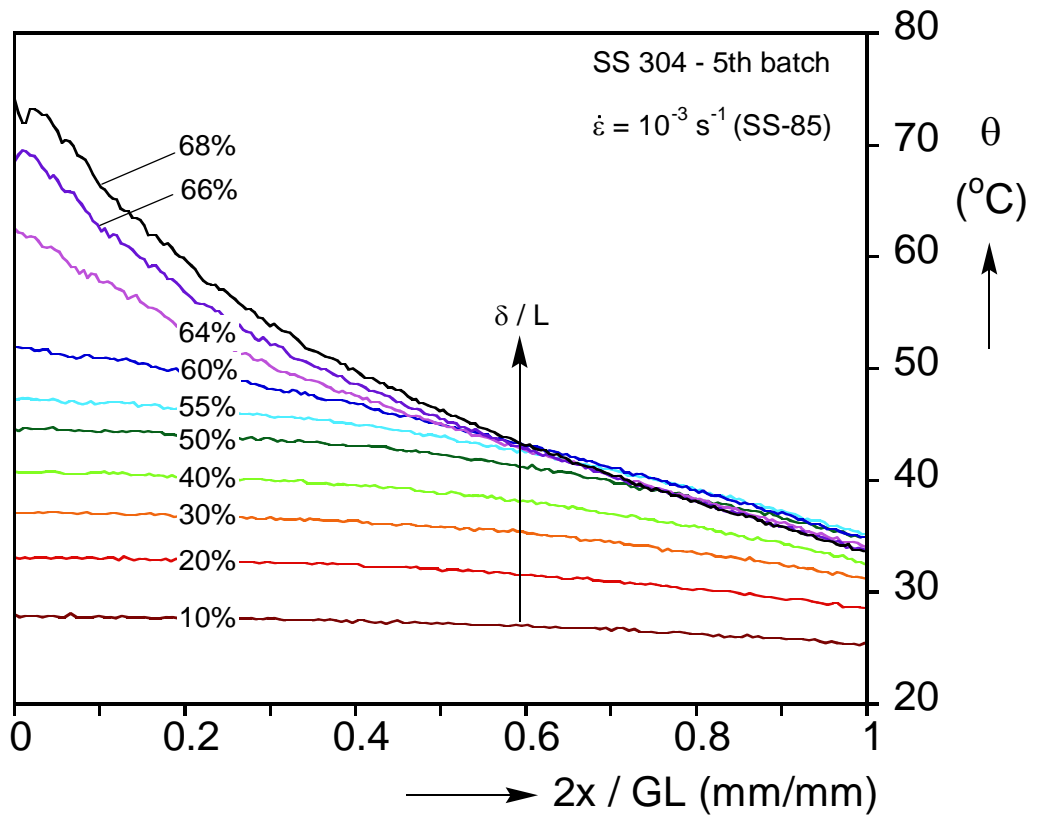


Figure 3-6:(a) axial engineering strain, and (b) temperature, along the specimen during monotonic testing

The full-field DIC and IR measurements can also be used to probe the evolution of localization in the pulsed tension experiments. [Figure 3-6a](#) shows snapshots of the strain distribution along the pulsed experiment SS-75 ( $\dot{\epsilon} = 10^{-3}$  /s) during a given strain pulse. At  $\delta/L = 50.8\%$  (beginning of the pulse) the deformation was already non-uniform, indicating that necking had already begun in the previous pulse, before unloading. (The DIC supplies Lagrangian strains; as discussed in [Section 2.2.3.ii](#), the conversion to engineering strains is only approximately correct past the onset of necking.) Since the necked region had more work-hardening than its immediate neighborhood but a comparable temperature, the deformation shifted upon reloading to just outside of the neck. As a result of deformation-induced heating, the temperature increased in these regions. A double peak in the temperature gradient is visible in [Figure 3-8](#) from  $\delta/L = 53.81\%$  to  $56.28\%$ . (Notice that the temperature gradient at  $\delta/L = 52.74\%$  is lower than at  $50.8\%$  due to thermoelastic cooling during that loading.) This promoted further deformation in these regions and resulted in a more diffuse neck than in the corresponding master monotonic experiment ([Figure 3-7](#)). Ultimately, the deformation shifted back to the center of the specimen and failure occurred there. Notice that the process just described requires that the strain-rate would be non-uniform inside the gage length and around the growing neck.

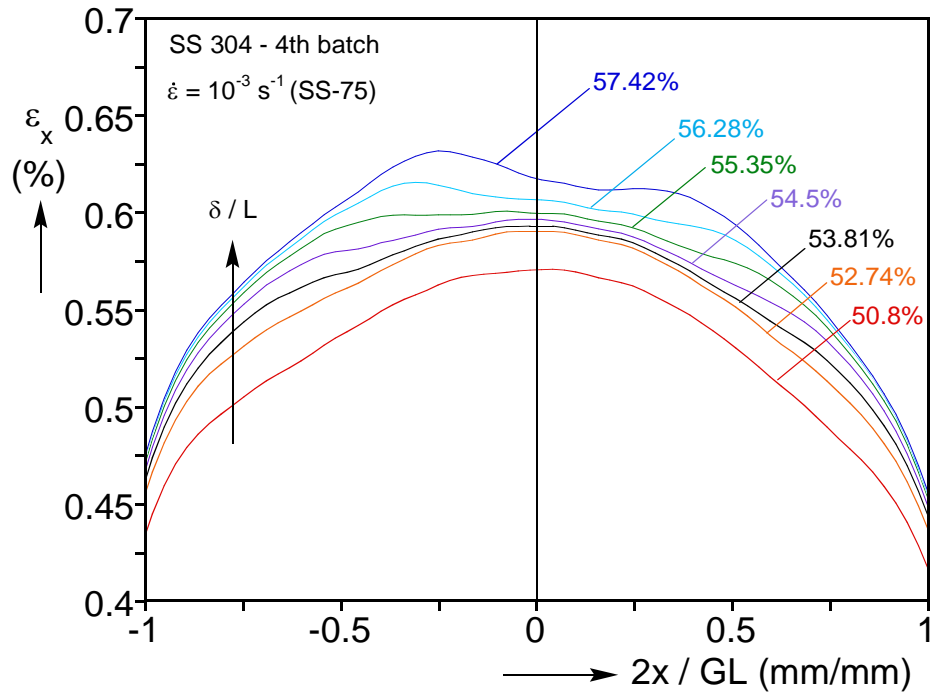


Figure 3-7: Axial engineering strain

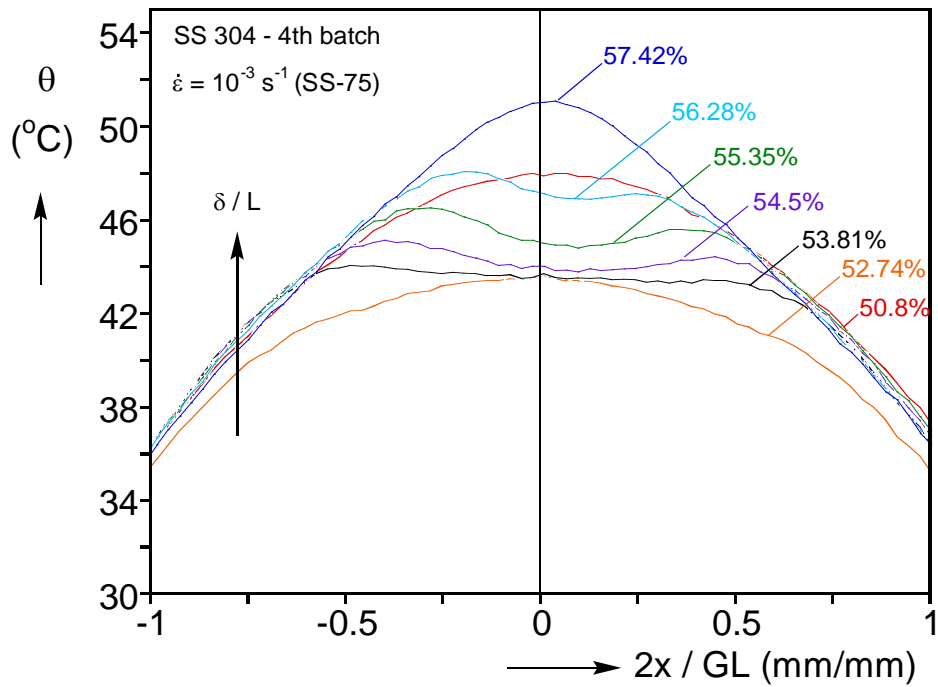


Figure 3-8: Temperature along the specimen during pulsed testing

With the information gathered thus far, a hypothesis for the enhanced elongation-to-fracture of the pulsed experiments can be postulated. The mechanical work and hence the heat generated is comparable between the pulsed and the monotonic experiments (Figure 3-1). Since however the former can last significantly longer than the latter (Table 3-1), the heat generated is given more time to conduct away from the specimen. Hence, milder temperature gradients develop in the pulsed case than the monotonic one, leading to an enhanced elongation-to-fracture. By the same token, if the experiments are performed too fast, then all loading cases approach the adiabatic conditions irrespectively of the type of loading; while if they are performed too slowly, they all approach the idealized isothermal case. In either of these extremes, the difference in elongation-to-fracture for different loading types should be erased if it was solely due to the temperature gradients.

The results plotted in Figure 3-2 corroborate this hypothesis. Furthermore, the hypothesis was verified by conducting additional monotonic experiments, where the crosshead velocities were adjusted to be such that these experiments would last the same amount of time as the pulsed ones. These experiments will be termed “equal time”. A comparison of the recorded stress-strain response to the monotonic and the pulsed experiments, extracted from Figure 3-2 shows that the elongation-to-fracture of an equal time experiment is now the same as the pulsed case (Figure 3-9). Furthermore, a direct comparison of the temperature gradients that develop in the monotonic, pulsed and equal time experiments (Figure 3-10) reveals that at the same time instances during these tests, the pulsed and the equal time experiments have developed identical or very similar temperature gradients. In contrast, the monotonic experiment has developed a sharper gradient than the other two, since by then it has already accumulated much more plastic strain. For example, at  $T = 60$  s, the axial strain during the monotonic experiment is 36% and the plastic work accumulated is 620.37 MPa, while for the pulsed

experiment these numbers are 14.85% and 530 MPa and for the equal time one they are 12.99% and 506.2 MPa, respectively.

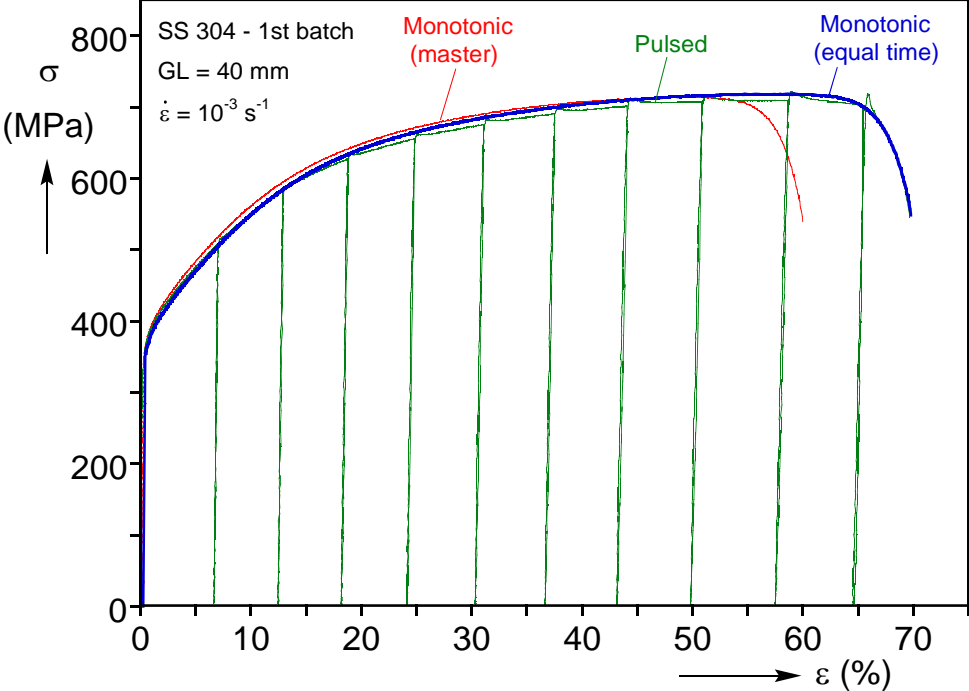


Figure 3-9: Stress-strain response from Figure 3-1 with the equal time test added



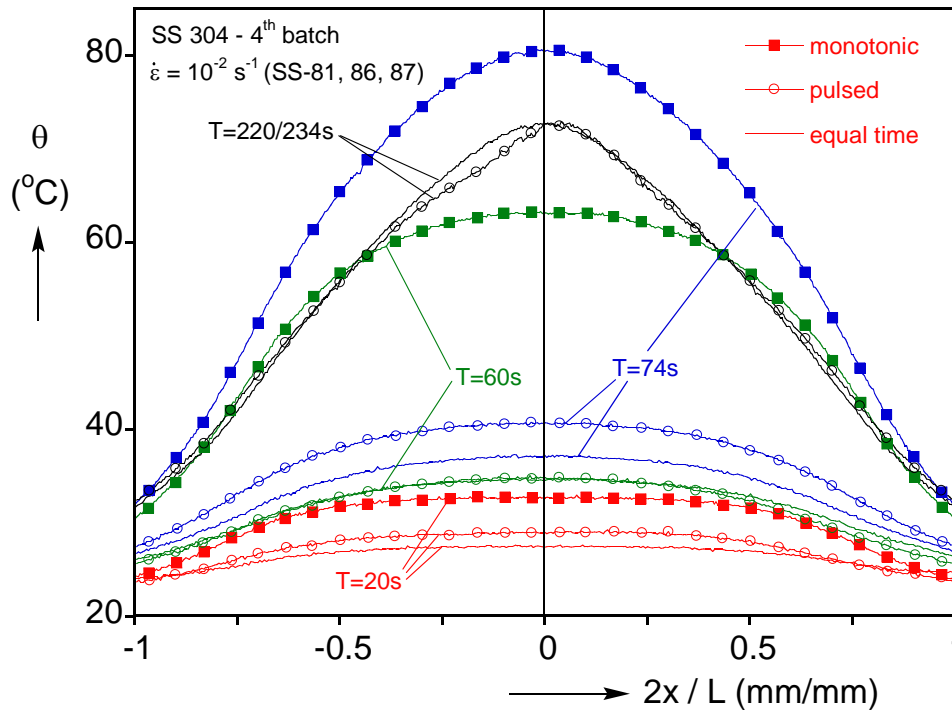


Figure 3-10: Temperature evolution along the monotonic, pulsed and equal time

Thus, recasting the elongation-to-fracture in terms of the duration of the experiment yields the strong correlation shown in Figure 3-11. Experiments which last the same amount of time can be expected to show similar elongation-to-fracture, irrespectively of the way the load is applied (monotonic, pulsed or hold), as they develop similar temperature gradients. Hence the enhancement reported in Figure 3-1 and Figure 3-2 is due to, and regulated by, these gradients. In that sense, the extended duration of the pulsed experiments leads to the development of less severe temperature gradients than in the corresponding monotonic experiments, somewhat negating the detrimental effects of these gradients on the elongation-to-fracture.

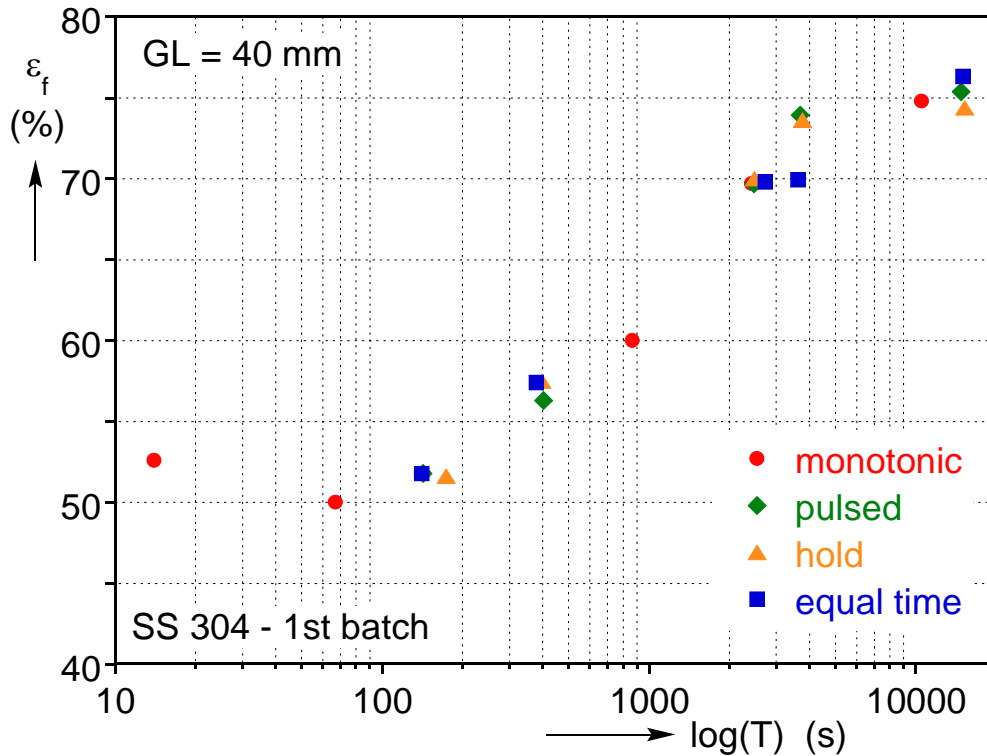


Figure 3-11: Duration of testing vs. elongation to fracture

### 3.2 Determination of material properties for modeling

The major challenge in developing a reliable numerical simulation of the experiments described is in the proper measurement of the material properties. Stainless steel 304 is a material that is strongly rate- and temperature-dependent and prone to martensitic transformation (De, Murdock, Mataya, Speer, & Matlock, 2004); (Lee, Kim, & Han, 2010) (Beese & Mohr, 2011) (Moser, Gross, & Korkolis, 2014). In addition, its low thermal conductivity and the temperature gradient that develops during the experiment as a result of deformation-induced heating lead to the mechanical and thermal responses being tightly intertwined. This is illustrated in Figure 3-12, which shows 6 uniaxial tension experiments with strain-rates ranging from  $10^{-1}$  /s (which is approximately the upper limit of our servohydraulic equipment for this specimen size) to  $10^{-4}$  /s. These responses cascade as expected at low strain levels, with the

flow stress increasing with the strain-rate (Meyers, 1998) (Meyers and Chawla, 1998). However, as the plastic deformation accumulates the specimens heat up and in a spatially non-uniform way, with the faster ones developing sharper temperature gradients which in turn trigger the localization of deformation. Hence, as shown in Figure 3-12, the flow stress at the faster experiments begins to saturate and the specimens fail earlier than they do in the slower experiments.

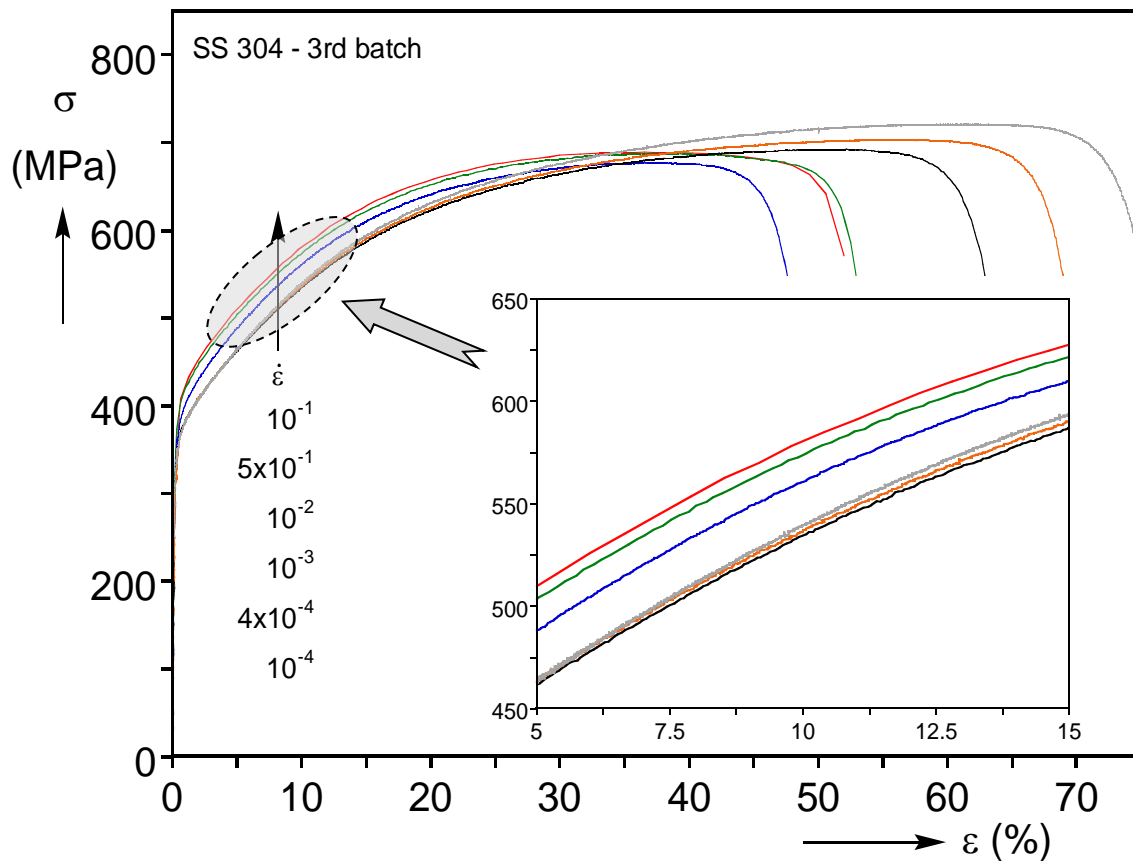


Figure 3-12: Stress-strain curves of SS304 at various strain rates

As discussed in Section 2.3, in order to create an accurate numerical simulation described in Section 4, it was necessary to decouple the mechanical from the thermal responses of the material. As shown in the infrared images in

Figure 3-13, a very uniform temperature field was maintained along the specimen throughout the experiments (compare the temperature scale in

Figure 3-13a to that of Figure 3-5). Indeed, just before failure the temperature difference between the center and the rest of the isothermal specimen did not exceed 3 °C, in contrast to more than 35 °C in the  $\dot{\epsilon} = 10^{-3}$  /s conventional experiment shown in Figure 3-5. As shown in Figure 2-18, the different emissivities of SS-304 and that of copper heat exchanger do not affect these measurements because of the black and white paint applied to its surface.

With the aid of the isothermal device, isothermal tension experiments have been performed at six temperatures (25, 30, 35, 60, 100, 150 °C) at strain-rates of  $10^{-4}$ ,  $4 \times 10^{-4}$ ,  $10^{-3}$  and  $10^{-2}$ /s. The plots of these tests are shown in Appendix A. The responses for  $\dot{\epsilon} = 10^{-3}$  /s are shown in Figure 3-14, along with a conventional tension experiment at the same strain-rate plotted with a dashed line. Initially, the conventional tension response matched the isothermal experiment performed at 25 °C (approx. room temperature). However, after the development of additional plastic strain (less than 10%), the conventional experiment exhibited a reduced flow stress as a result of the deformation-induced heating. This induced a temperature gradient (shown in Figure 3-5) that lead to a premature localization of deformation and an early failure in comparison to the 25 °C isothermal tension experiment.

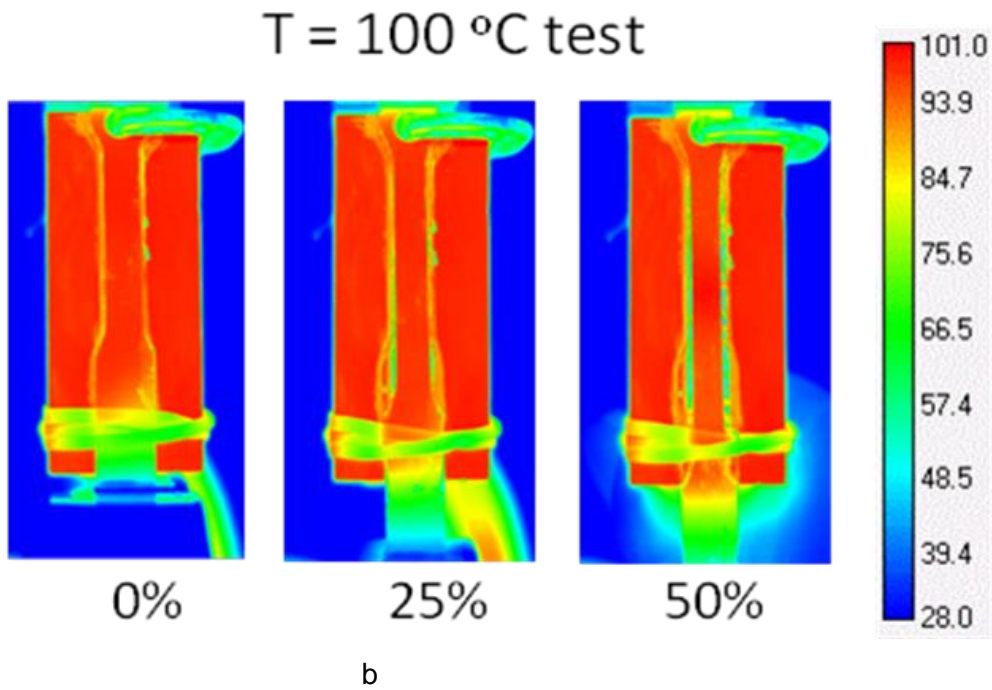
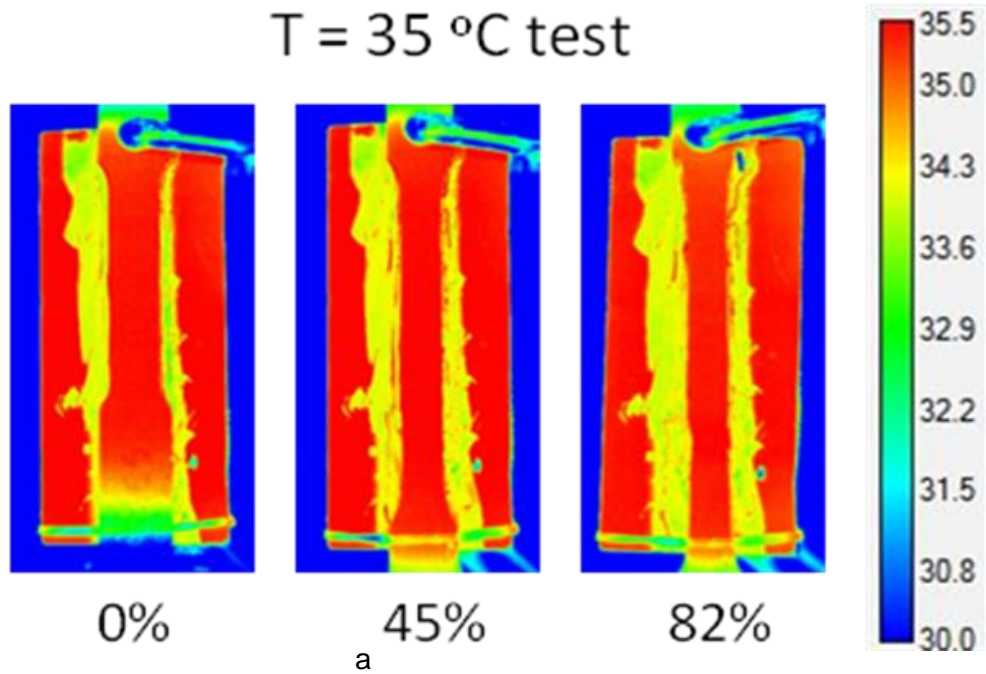


Figure 3-13: Isothermal tests at various levels of strain, a) 35°C and b) 100°C. These images indicate that the specimen is maintained at a fix temperature

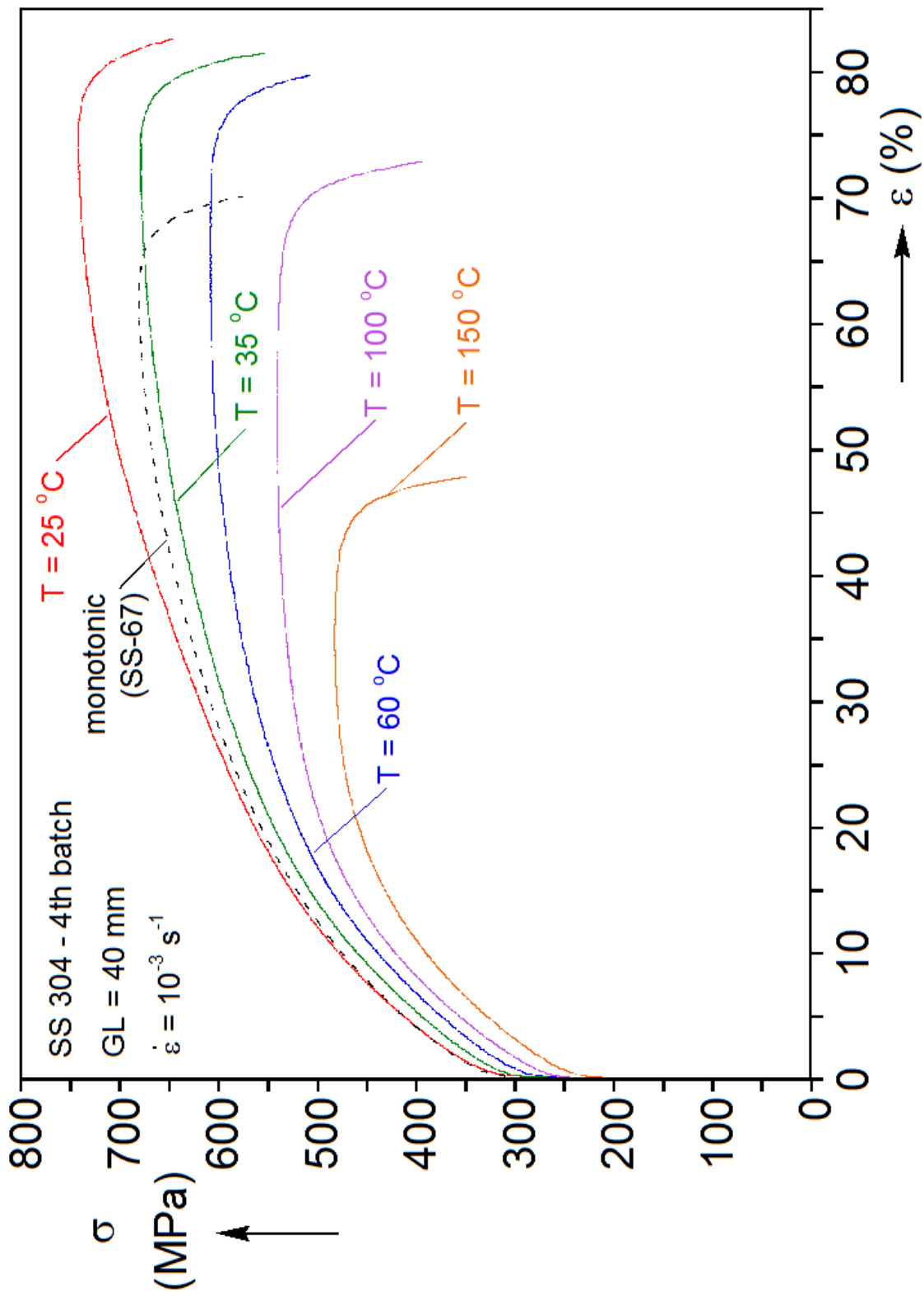


Figure 3-14: Isothermal stress-strain response at various temperatures

The effect of the temperature on the ultimate tensile strength and the elongation-to-fracture (for 40 mm gage length) for different strain-rates is summarized in Figure 3-15. The ultimate tensile stress is seen to drop monotonically with the increase in temperature and the decrease in the strain-rate. The elongation-to-fracture follows a similar trend, even though the sensitivity to the strain-rate is quite mild for the rates examined. The anomaly observed between 25 and 35 °C is related to the martensitic transformation that takes place at that temperature range; (Cho, Yoo, & Jonas, 2000); (De, Murdock, Mataya, Speer, & Matlock, 2004); (Lee, Kim, & Han, 2010) (Beese & Mohr, 2011) (Moser, Gross, & Korkolis, 2014)

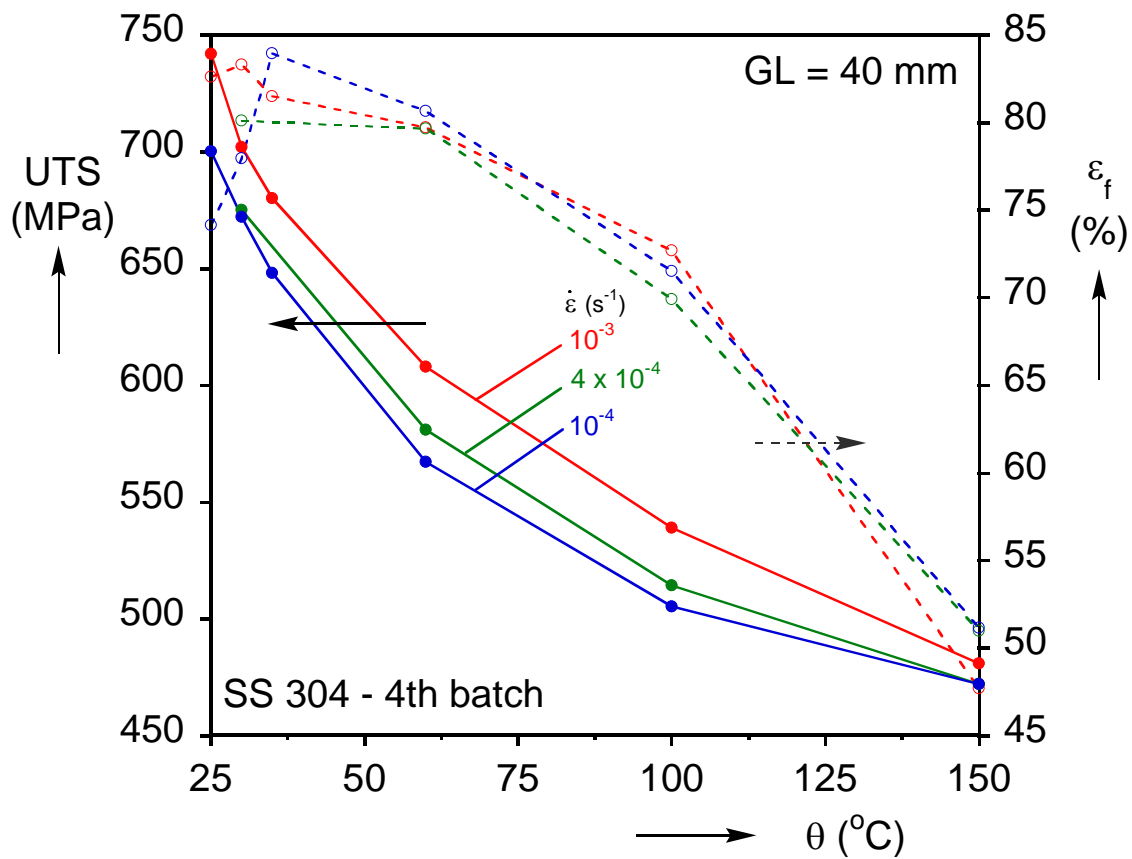


Figure 3-15: Dependence of the UTS and the elongation-to-fracture on the temperature of the isothermal tension experiments, for 3 different strain-rates.

# CHAPTER 4

## NUMERICAL MODELING

The experimental data obtained in [Section 3](#), were used to create a numerical model which can predict the material behavior, not only for the simple case of uniaxial tension described here but also for more complex loading predictions as well. The model uses the inputs from the physical experimentation, such as specimen geometry, mechanical deformation, heat generation and transfer, along with the material behavior at different temperatures and strain rates. This chapter describes in detail how these were incorporated in the numerical simulation software, and then compares the predictions of the model to the experimental observations.

### 4.1 Model Setup

The experiments were simulated using the nonlinear finite element code Abaqus/Standard. Isotropic hardening with an associated flow rule based on the von Mises yield surface is assumed throughout. The mesh consisted of C3D20RT continuum, 20-node, reduced integration elements capable for large deformations and coupled temperature-displacement analysis. These elements have quadratic shape functions for the displacement and linear for temperature. The model utilized yield stress and plastic strain input curves for different temperatures for its material data, and film coefficients for conductive and convective heat transfer, as described in detail in this section. The final model made use of the symmetries present, and only 1/8 of the specimen geometry was discretized ([Figure 4-1](#)).



### 4.1.1 Geometric Imperfection

Despite the deformation-induced heating which results in a temperature gradient along the specimen, it was found necessary to aid the triggering of the necking instability by adding a geometric imperfection at mid-span. At first a linear slope was used to produce the imperfection, starting with the nominal width and reducing it linearly toward the center of the specimen. The notch sensitivity was explored without rate dependence, starting from the uniform width and increasing the mid-span amplitude of the imperfection in 100 $\mu\text{m}$  increments to 400 $\mu\text{m}$ , which produced the load-displacement plots in [Figure 4-2](#).

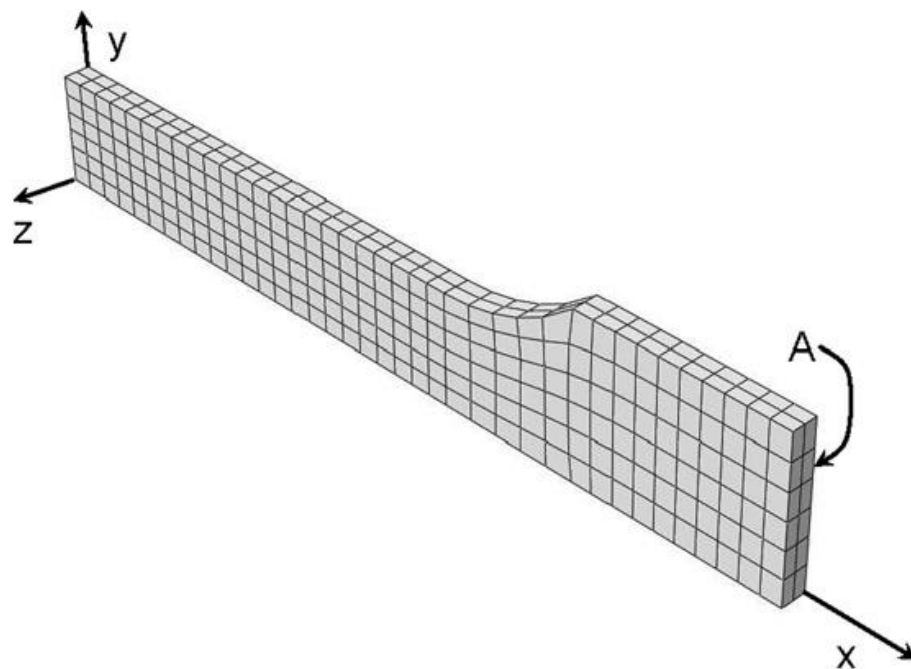


Figure 4-1: Schematic of the finite element model of the uniaxial experiments and the coordinate system adopted in this work

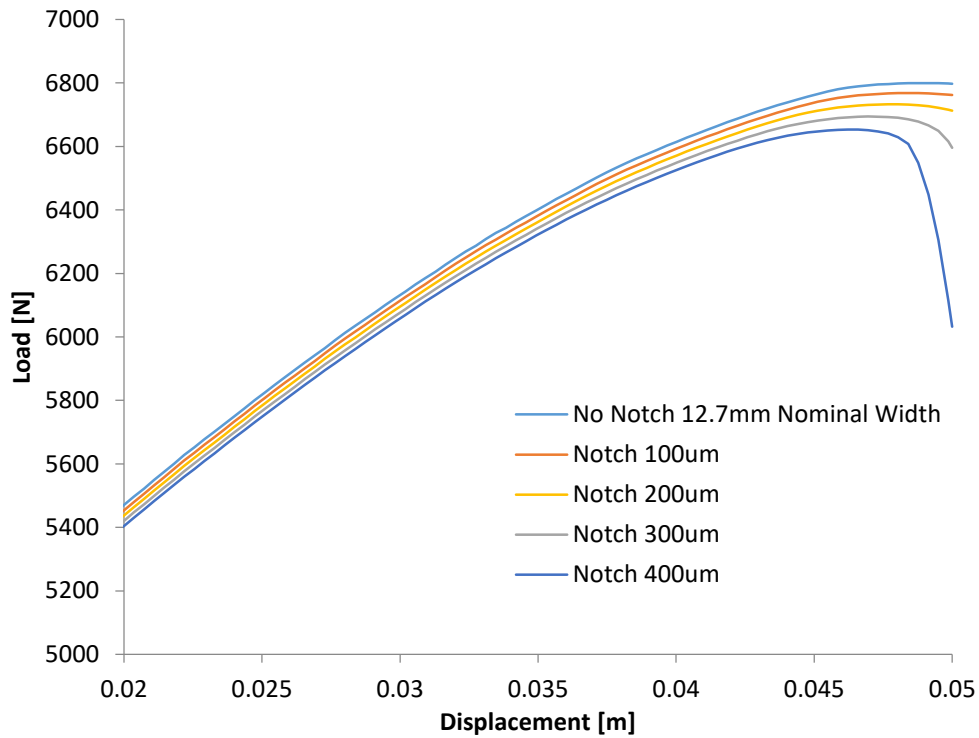


Figure 4-2: Linear notch size and the effect on numerical simulation of failure

It was found that without the notch to trigger the localization, failure would not occur and instead the simulation would abort. A notch with a depth of as little as  $2\mu\text{m}$  was enough to trigger a localization and allow the simulation to process. As would be expected, it can be seen in Figure 4-2 that the size of the notch has a strong effect on the rate of localization and failure. The initial extrapolation of the iso-thermal input curves discussed in Section 4.2.3 used the simple notch model for testing with a notch of  $2\mu\text{m}$ , which was enough to initiate the localization but proved to cause simulation errors for the more complicated not iso-thermal simulations. Furthermore, when the rate dependence was implemented the output no longer matched the experimental data (Figure 4-11). An alternative to the simple notch was to utilize an equation-driven imperfection (Chen, 1971), with the width of the specimen  $w(x)$  made to vary with the axial distance  $x$  measured from mid-span (Figure 4-1) as follows:

$$w(x) = w_0(1 - \alpha e^{-\beta x^2}) \quad (4.1)$$

where  $w_0 = 6.35$  mm is the undeformed nominal half-width,  $\alpha = 0.015$  is a parameter controlling the amplitude of the imperfection at mid-span and  $\beta = 7000$  is the imperfection decay parameter (Figure 4-3). These parameters were adjusted so that the pre-necking region of the numerical output matched the experimental material response but were able to trigger localization. No imperfection was prescribed for the specimen thickness. This new imperfection utilized almost identical input curves that were developed for the simple notch, but did not create the simulation instability of the simple notch.

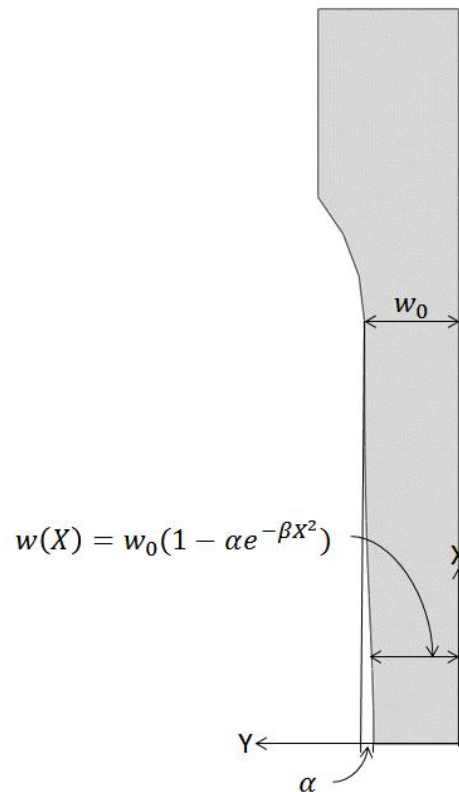


Figure 4-3: Equation-driven imperfection, shown here greatly exaggerated for ease of visualization.

### 4.1.2 Mesh Reduction and Refinement using Symmetry

The mesh of [Figure 4-1](#) was adopted after suitable parametric studies, starting with the full model of the specimen, excluding the ends which were held in the grips and did not deform during the experiment ([Figure 4-4](#)). The full model was constructed of 10994 elements, with 4 elements through the thickness and took almost 3 hours of simulation time on a Dell PowerEdge 2900III, 2X Intel Quad Core Xeon 3.0GHz server, running Linux OS (Ubuntu 11.04 64-bit) with 64GB RAM to complete. It was then determined that a new model could be created that could take advantage of the symmetry and the full model was cut in half through the XY, and XZ planes and consisted of 2736 elements and can be seen in [Figure 4-5](#). Boundary conditions of symmetry were used on the XZ, and XY planes and no heat transfer was permitted at those plane. The processing time for this model was approximately 35 minutes, almost 5 times faster and the results fell on top of those of the dense full model mesh in [Figure 4-4](#).

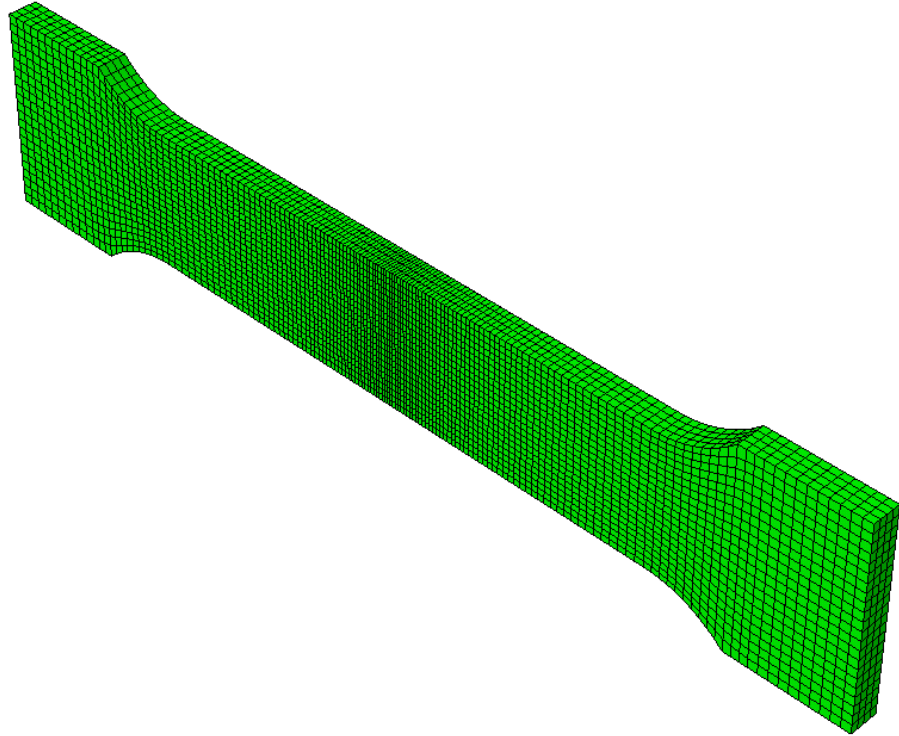


Figure 4-4: Full model of tensile specimen, using 11016 elements

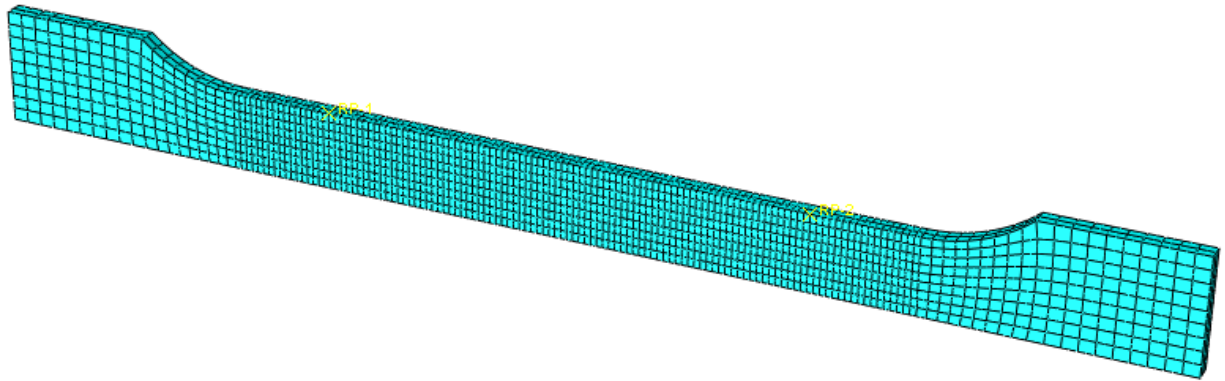


Figure 4-5: Quarter model with dense mesh of 2736 elements

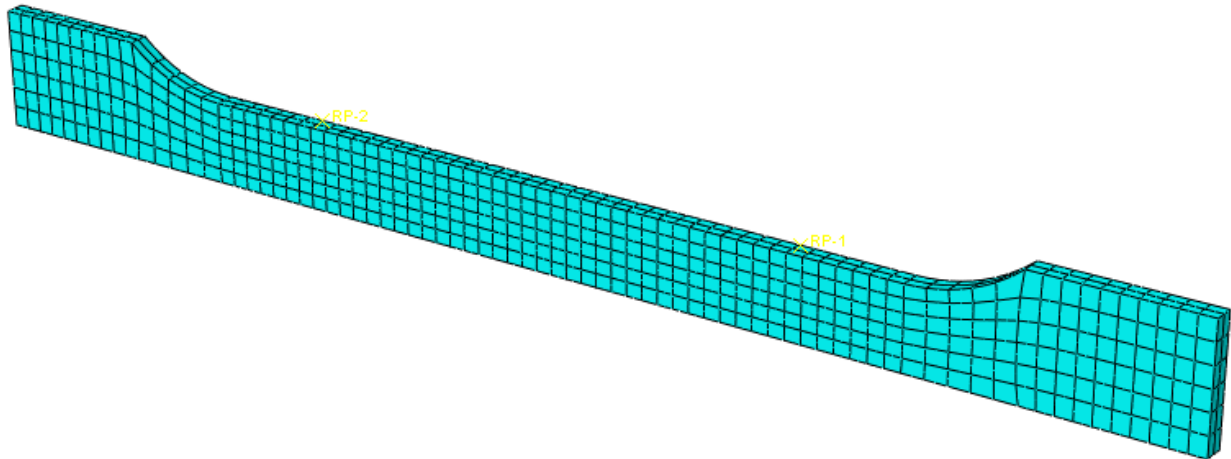


Figure 4-6: Quarter model with coarse mesh of 912 elements

The mesh was further modified with less elements to create a coarse mesh (Figure 4-9) to reduce the computational run time. This mesh was the least dense that did not show any appreciable deviation from the full models results. A comparison of the three different meshes are shown in Figure 4-7 and it can be seen that all three engineering stress-strain responses fall on top of each other.

The symmetry of the model about its center was used to create a one eighth model with 456 elements. The output of this model was identical to that of the quarter model with 912 elements. The use of quadratic elements allows for a minimum of two elements through the model thickness. As such, the model is capable of representing the deformation of the specimen past the onset of necking but it is not suitable for capturing the actual rupture at the end of the experiment, which has less than 1/8 symmetry. This, of course, is beyond the scope of this work and the capabilities of the continuum description adopted here.

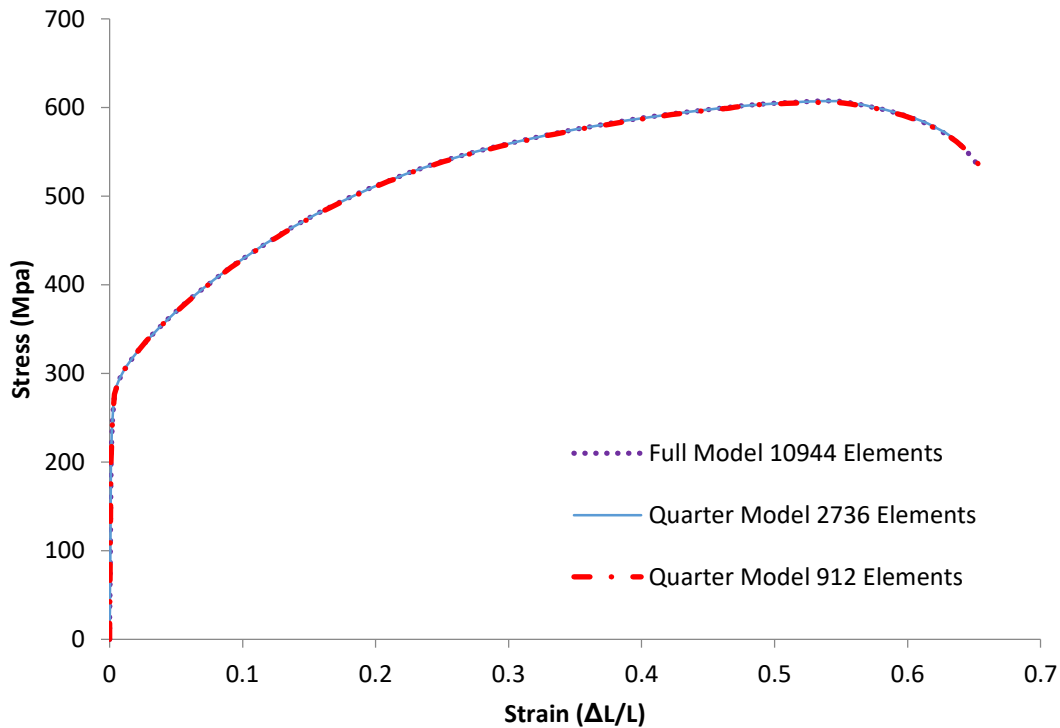


Figure 4-7: Comparison of the numerical simulation results from the full model (10944 elements), quarter model (2736 elements) and the coarse quarter model (912 elements)

#### 4.1.2.i Mechanical Boundary Conditions

Symmetry boundary conditions were prescribed at the  $x = 0$  mm,  $y = 0$  mm and  $z = 0$  mm planes (Figure 4-1) to replicate the full specimen, resulting in the eighth model described above. A uniform displacement was prescribed at plane A (Figure 4-1). This was the location where the shoulder of the specimen emerged from the grips. The boundary condition was implemented with the “kinematic coupling” option available in Abaqus, to facilitate the measurement of the total load applied. The “kinematic coupling” allows for a single control point to be directly tied to all the nodes and elements in a specified region. The degrees of freedom for all directions and rotations can be specified and were all linked to the control point, which is displayed as the load

cell in Figure 4-8. In this way a displacement can be applied to the control point and the resulting load monitored throughout the experiment. Since any constraint applied to the control node is replicated at the node and elements on the model, only a displacement in the x direction was permitted and all other displacements and rotations were set to zero. This resulted in no contraction of plane A in the y- and z- directions, which replicated the gripped end.

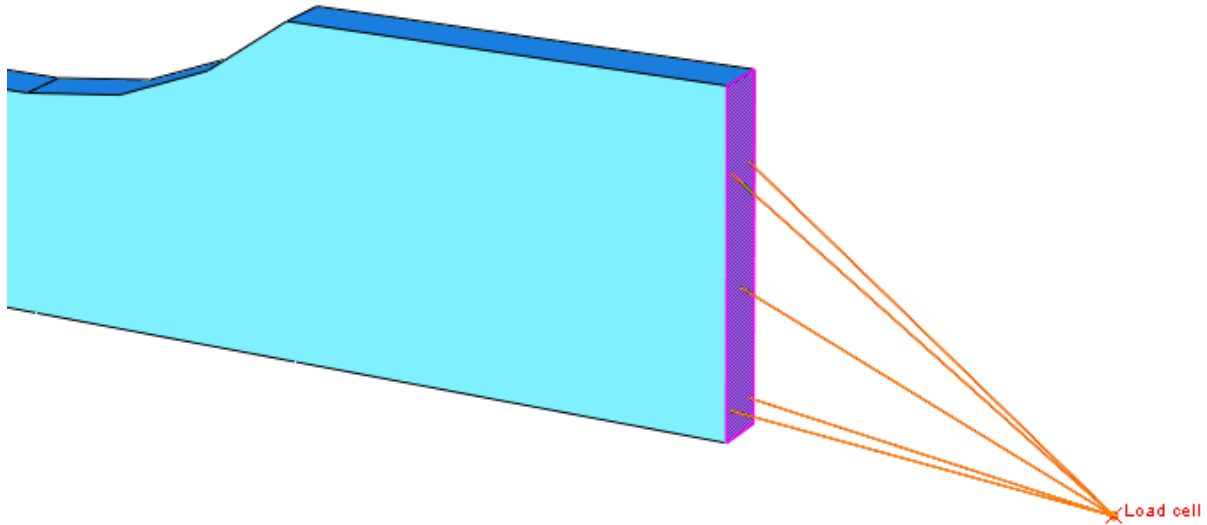


Figure 4-8: Kinematic coupling boundary condition with "load cell" control point

#### 4.1.2.ii Thermal Boundary Conditions

An adiabatic condition at the three symmetry surfaces was used. A film (or convection) coefficient of  $h = 24 \text{ W/m}^2\text{-K}$  was applied to the free sides where convection to the still air would occur. This value was arrived upon after iteratively adjusting the coefficient until the temperature gradient along the gage length of the specimen was very close to that of the corresponding experiment. Due to the uneven contact between the grips and the specimen, the conduction of heat from the end of the specimen to the grips was instead simulated as convection, but using a much higher film coefficient  $h = 200 \text{ W/m}^2\text{-K}$  applied on plane A. As with the convection heat transfer coefficient, this value was adjusted to keep the end of the specimen at the same



temperature seen throughout the corresponding test. The sink temperatures used for the air and the grips were both set to 23°C. The values for film coefficient were arrived at after some trial and error discussed in the results [Section 4.3](#).

Thermal radiation from the specimen to the surrounding ambience was neglected ([Farren and Taylor, 1925](#)). The model was loaded by specifying the displacement and time needed to replicate each step in the corresponding experiment.

## **4.2 Model inputs for numerical simulation**

### **4.2.1 Displacement Control**

The simulations were conducted with a prescribed displacement to correspond to the physical experiments. Since the gripped material in the experimental setup is prone to a small amount of slipping, the displacement prescribed in the model had to be adjusted until the stress at the end of the run was approximately the same as that of the experiment. This was done to keep the testing time the same between the experimental and simulated results since the material behavior is controlled by rate dependent variables. For the pulsed experiments this meant stopping the simulation after each pulse and making very minor changes to the displacement to account for the small amount of slipping in the grips so that the unloading and loading cycling would coincide with that of the experiment.

### **4.2.2 Inelastic Heat Fraction**

The inelastic heat fraction (i.e., the fraction of the plastic work that is converted into heat) was set to 0.93 and kept constant throughout the simulation. This value is not constant and is rate dependent ([Zehnder, Babinsky, & Palmer, 1998](#)) ([Hodowany, Ravichandran, Rosakis, & Rosakis, 2000](#)), which could not be easily simulated with Abaqus.

### 4.2.3 Input curves

In order for the numerical simulation software to accurately predict the material behavior, input data needs to be included, and needs to describe the material behavior for all conditions encountered. Since in the region where necking occurs, the deformation is no longer uniform, the experimental data obtained up to the onset of necking (i.e., where the deformation is uniform) cannot be used. To identify the material behavior beyond necking, the stress-strain hardening curves were extrapolated with the aid of the isothermal experiments. In the finite element model of these experiments, both the temperature- and the rate-dependence were turned off. The localization was triggered with a geometric imperfection (simple notch) discussed in [Section 4.1.1](#). The experimental data from the isothermal experiments at 25, 30, 35, 60, and 100°C at the quasi-static strain rate of  $10^{-4}$  /s were converted from engineering to true stress ( $S$ ) and strain from yield until the point of necking or the ultimate tensile strength. An extrapolation of this data was then performed and the new material data curve was fed into Abaqus to compare the numerical results to the experiments. Initially, the extrapolation of the curve was done with the standard linear, power law, and flat hardening models, but none of these produced accurate material responses in the numerical model after uniform deformation. After testing a number of curve fitting algorithms for extrapolation of the stress-strain curve, the Morgan-Mercer-Flodin (MMF) model ([eqn 4.2](#)) was found to have very low residuals close to the ultimate tensile strength for the experimental data and the numerical simulations produced reasonably close results to that of the experimental data after necking.

$$S = \frac{(a \cdot b + c \cdot e^d)}{b + e^d} \quad (4.2)$$

In this model,  $a$ ,  $b$ ,  $c$  and  $d$  are fitting coefficients (the 1<sup>st</sup> and 3<sup>rd</sup> having units of stress, the other two being unit-less). The MMF model was adopted in this work because it easily allows for a sigmoidal stress-strain relationship (see [Figure 3-14](#)). After a numerical simulation that used

the initial guesses of the MMF coefficients, these were iteratively adjusted so that the output load-displacement (or engineering stress-strain) response from the model very closely matched the one measured experimentally. In order to keep the data from having a large change in slope which would cause instability in the numerical model, a number of data points at the end of the experimental data where the MMF model was used for extrapolation were manually altered to keep the changes from data point to data point small. This was repeated for all temperatures for which isothermal data existed and resulted in a set of extrapolated hardening curves, covering the temperatures used for the isothermal experiments. The final input curves for the simple notch discussed in Section 4.1.1 are shown in Figure 4-9 and the stress-strain output from the numerical modeling shows excellent agreement is shown in Figure 4-10.

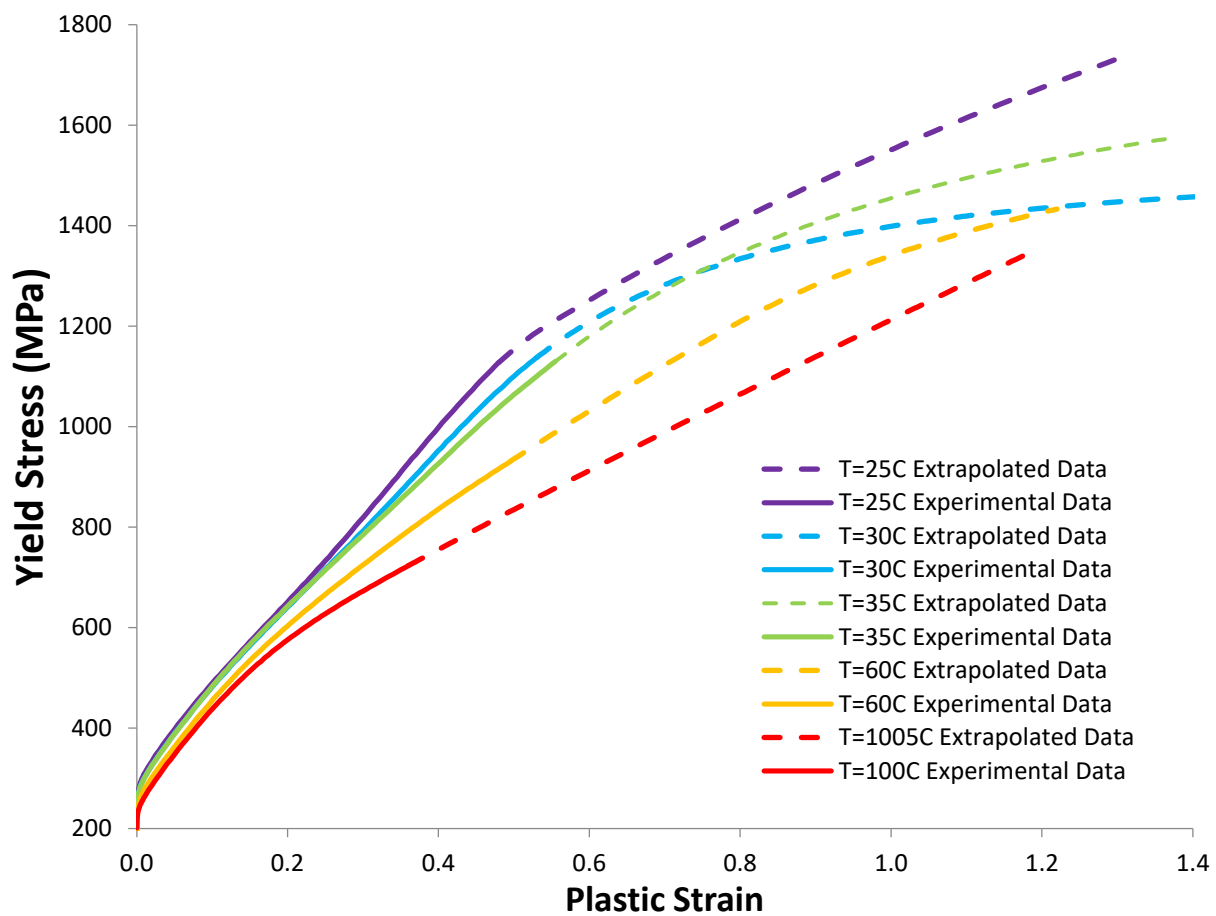


Figure 4-9: Numerical input curves for both the simple notch and the equation driven notch

It was found that after the rate dependence ([Section 4.2.4](#)) was turned on for the simple notch imperfection model, the output did not follow the experimental data any longer. It can be seen in Figure 4-11 that the non-rate dependent output matches the experimental data well but after the rate dependence (RD), and simulation time which controls the strain rate ( $10^{-4}$  to  $10^{-7}$  s<sup>-1</sup>) are increased the output deviates drastically from the experimental. In order to overcome this issue the equation-driven notch was then implemented ([eqn. 4.1](#)) and the imperfection adjusted until the rate dependent output from the simulation matched that of the experimental data, which yielded the results that were shown in Figure 4-10.

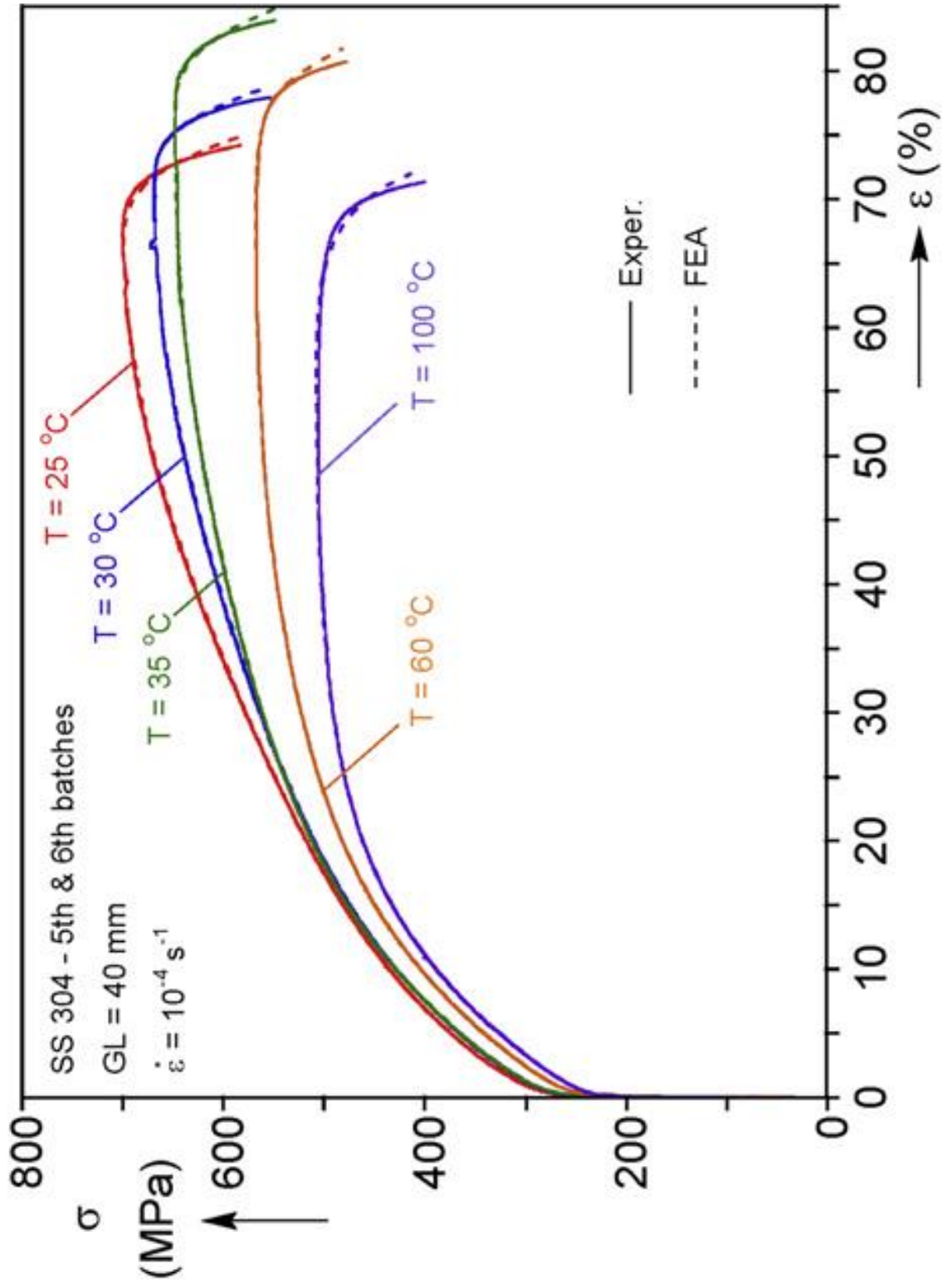


Figure 4-10: Engineering stress–strain curves of the isothermal tension experiments and their simulations.

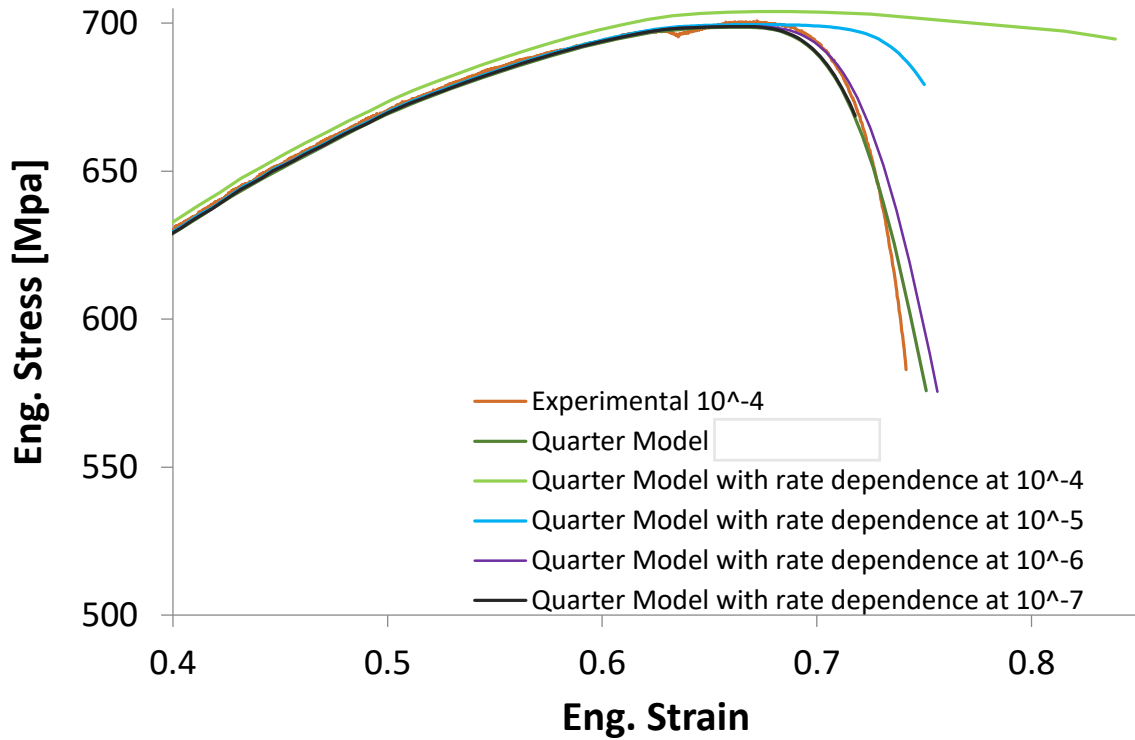


Figure 4-11: Simple notch numerical model and the effect of strain rate on the output curve

#### 4.2.4 Rate-Dependence

Abaqus allows for three different commonly used rate-dependence options to be applied to the model. Initially the [Cowper-Symonds \(1957\)](#) option was used to describe the rate-dependence behavior of the material with constants determined for the values of the yield stress at 1% and 5% strain for standard non-isothermal tests ([Table 4-1](#)). The [Cowper-Symonds \(1957\)](#) model is shown in [equation 4.3](#) which describes the dynamic stress ( $\sigma_d$ ) as a function of the static stress ( $\sigma_s$ ), the strain rate ( $\dot{\epsilon}$ ) and two constants C and P. The constant calculated from the data in [Table 4-1](#) are C of 500 and 600 with a P of 4.8 and 4.4 for 1% and 5% strain respectively.

$$\sigma_d = \sigma_s \cdot \left( 1 + \left( \frac{\dot{\epsilon}}{C} \right)^{\frac{1}{P}} \right) \quad (4.3)$$

Strain Rate [1/s]	Yield Stress [MPa] @ 1% strain	Yield Stress [MPa] @ 5% strain
0.0001	392	490
0.0004	392	490
0.001	393	493
0.01	412	515
0.05	432	537
0.1	439	543

Table 4-1: Data used to determine the Cowper-Symonds strain rate dependence.

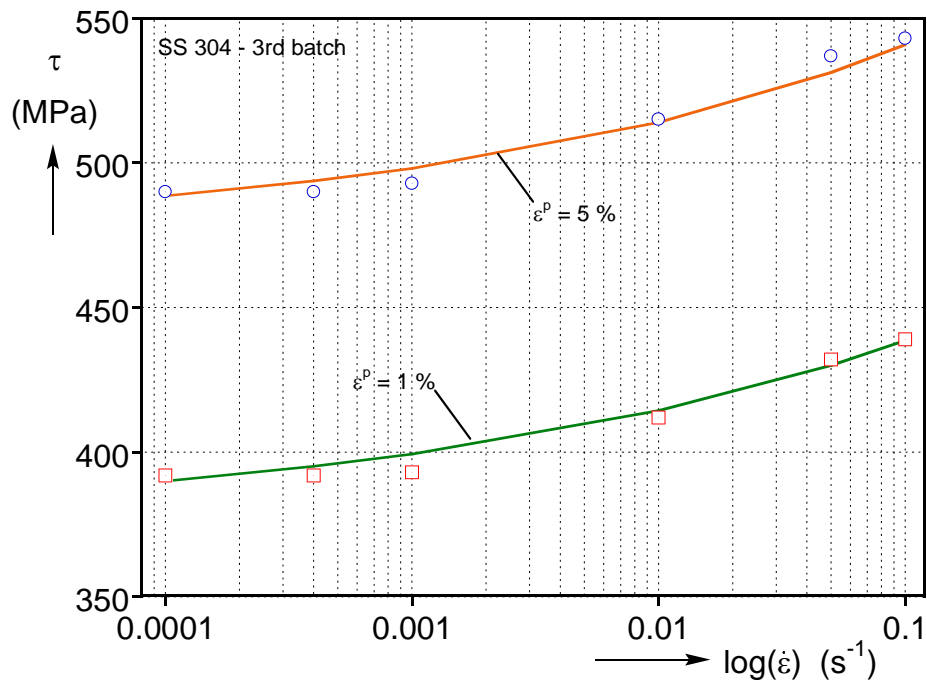


Figure 4-12: Flow stress at various strain rates and at two levels of plastic strain, for the calibration of the Cowper-Symonds viscoplastic powerlaw.

To better account for the temperature effects on rate-dependence in Abaqus, the “yield-ratio” option was used [Anon., 2009](#), which captured the behavior of SS-304 for the strain-rate range in hand more accurately than the [Cowper-Symonds \(1957\)](#) model. At a specific strain, the yield-ratio is defined as the flow stress at a given strain-rate over that of the quasistatic experiment. In our case, the  $\dot{\epsilon} = 10^{-4}$  /s experiment was chosen as the quasistatic limit. This procedure can be repeated for various temperatures and ultimately populate a table with multiple combinations of strain-rates and temperatures. In the present work, the yield ratios (see [Table 4-2](#)) were obtained from the various isothermal experiments at a strain of 10.5%. As the yield ratios change with plastic strain, this value was selected as the best representation of the behavior in this family of experiments. With the input curves thus extrapolated and the rate-dependence also included in the numerical models, the amplitude of the imperfection ( $\alpha = 0.015$ ) in [Eq. 4.1](#) was fine-tuned to trigger the localization at the same strains as observed in the experiments.

#### **4.2.5 Other constants**

The other inputs used for the numerical modeling are the density, specific heat and coefficient of thermal expansion which were set to the published values of 8030 kg/m<sup>3</sup>, 508 J/kg-°C and 1.69 10<sup>-5</sup> m/m-°C respectively ([Table 4-3](#)). Poisson’s ratio was set to 0.3 and Young’s modulus set to a non-standard 187 GPa to help match the experimental data where the unloading and reloading follows a hysteresis like loop discussed in the results.



Temperature [°C]	Strain rate [1/s]	Yield ratio
25	0	1
25	5.00E-05	1
25	0.000208	1.029
25	0.0049	1.07
30	0	1
30	5.00E-05	1
30	0.0002	1.03
30	0.0048	1.073
35	0	1
35	5.00E-05	1
35	0.00022	1.03
35	0.00537	1.075
60	0	1
60	5.00E-05	1
60	0.000203	1.037
60	0.052	1.09
100	0	1
100	5.00E-05	1
100	0.00022	1.025
100	0.00564	1.054
150	0	1
150	5.00E-05	1
150	0.00022	1
150	0.00555	1.036

Table 4-2: Yield ratios from isothermal tension experiments

**Mechanical properties**

Young's modulus	$\epsilon$	187MPa
Poisson's ratio	$\nu$	0.3
Strain-rate dependence	See table 4-2	
Hardening curves	See section 4.2.3	

**Physical and thermal properties**

Density	$\rho$	8030kg/m <sup>3</sup>
Thermal conductivity	$\kappa$	16.2W/(m K)
Inelastic heat fraction	$\eta$	0.93
Coefficient of linear thermal expansion	$\alpha$	1.69x10 <sup>-5</sup> 1/K
Specific heat	$C_p$	508J/(g K)

Table 4-3: Material properties input to the numerical model

### 4.3 Results

The model described above was used to simulate the entire family of monotonic, pulsed, hold and equal time experiments. The main characteristics of these results will now be discussed through some representative examples. The engineering stress-strain curves from the experiment and the numerical model of a monotonic and a pulsed test at  $\dot{\epsilon} = 10^{-3} /s$  are shown in Figure 4-13.

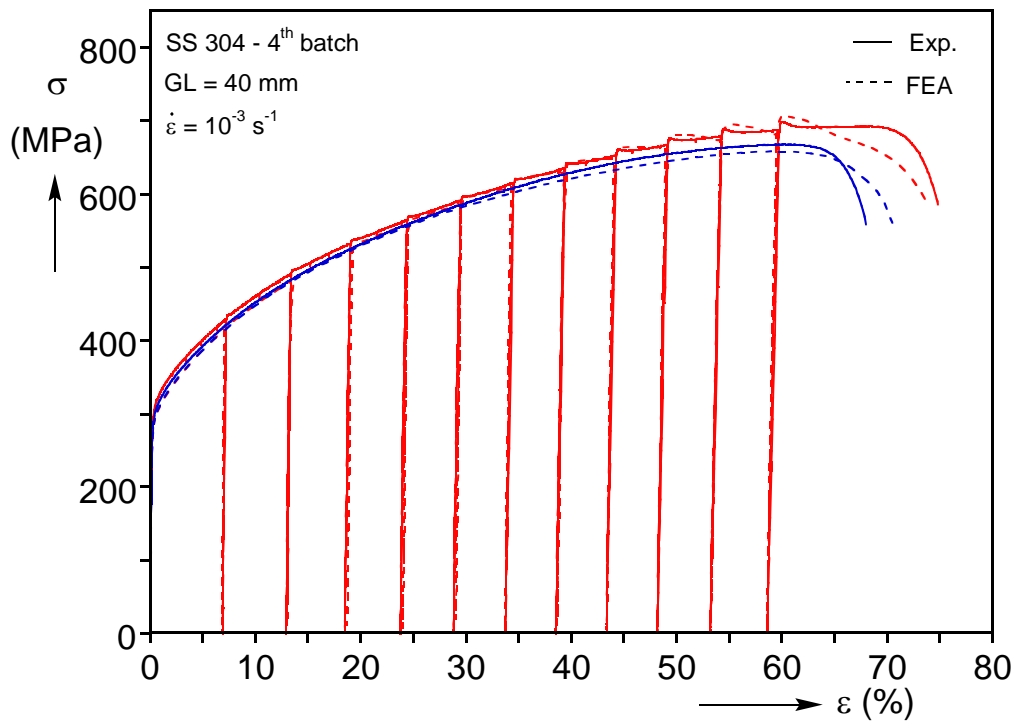


Figure 4-13: Engineering stress-strain response, numerical vs experimental

The numerical model is able to reproduce the flow stress with increasing plastic deformation due to both mechanical and thermal effects very well. Recall that the model is only informed of the isothermal and rate dependent data for SS-304 and not of the response of this specific monotonic experiment directly. A deficiency of the model predictions is observed after the onset

of necking, where the simulated responses do not drop as sharply as the experimental ones do. This is attributed to the lack of experimental data at the higher temperatures and strain-rates which prevail inside the neck ([Chapter 3](#)). However, the elongation-to-fracture is reproduced very well, as is the difference between the monotonic and the pulsed loading. A departure of the model from reality is in the simulation of the unloading and reloading after each strain pulse. This is shown in [Figure 4-14](#), where the rather complex nonlinear unloading and reloading of the real material is represented by the model as a linearly elastic response exhibiting the Young's modulus of the undeformed material. This is a direct consequence of adopting isotropic hardening in the simulations. The slope of each of the unloading and loading cycles changes with the amount of accumulated strain and so a non-standard Young's modulus was chosen. While the unloading behavior after finite strain is an active area of research (e.g., for studies of spring back in sheet metal forming, see ([Cleveland, 2002](#)); ([Yoshida, 2002](#)); ([Khan, 2010](#)); ([Sun, 2011](#))) and was initially a concern, the strain inaccuracy created by linearizing this behavior is rather minute (less than 0.5% over the entire simulation) in comparison to the overall strain at failure. Hence this deficiency of the model does not noticeably affect the predictions.

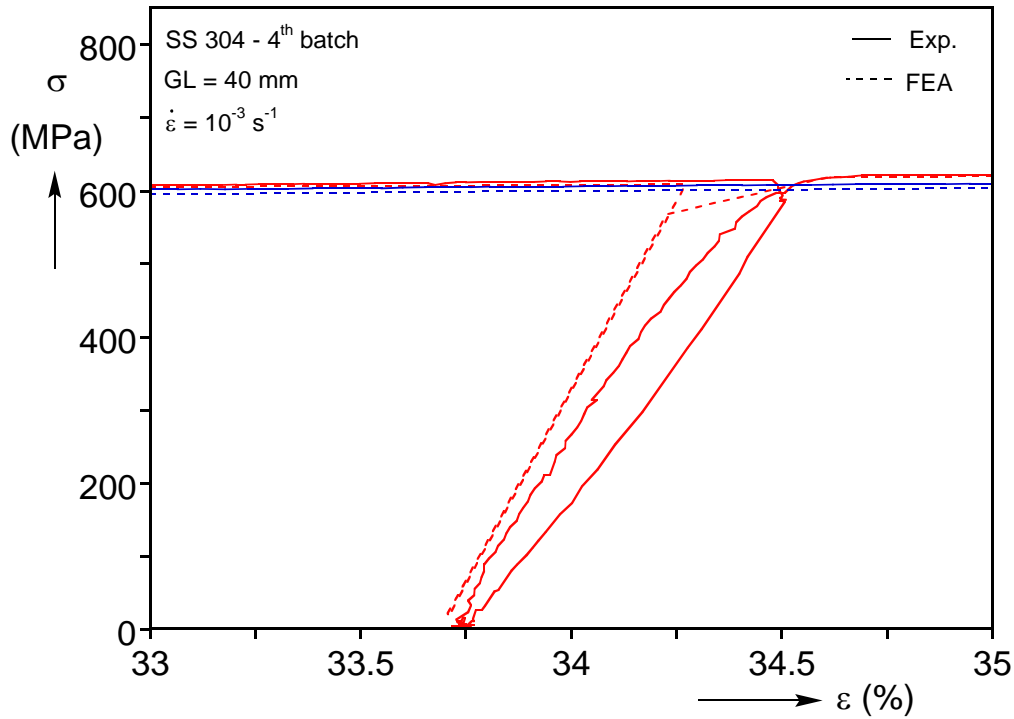


Figure 4-14: Magnification of one unloading–reloading loop. Included are experiments and numerical simulations.

As a result of the agreement shown in [Figure 4-13](#), the numerical model can capture the strain evolution during the experiment very accurately (see [Figure 4-15](#)). Notice that this experiment is included in [Figure 4-13](#) as the monotonic case. Interestingly, towards the end of the loading the strain localization is predicted to be spread over a larger distance around the location of the actual rupture. This is because the strain-rates and temperatures that prevail inside the neck are higher than what we were able to reproduce experimentally and input to the model. Hence the model predicts a less abrupt localization of deformation than is observed in reality. This more-diffuse-than-the-real neck is partly responsible for the discrepancy observed at the tails of the curves in [Figure 4-13](#).

While the mechanical aspects of the problem have been accurately captured by the modeling, the prediction of the temperatures that developed in the experiments shows much poorer agreement. This is shown in Figure 4-16, which compares the temperature fields developed in the same monotonic loading case as shown in Figure 4-13 and 4-15.

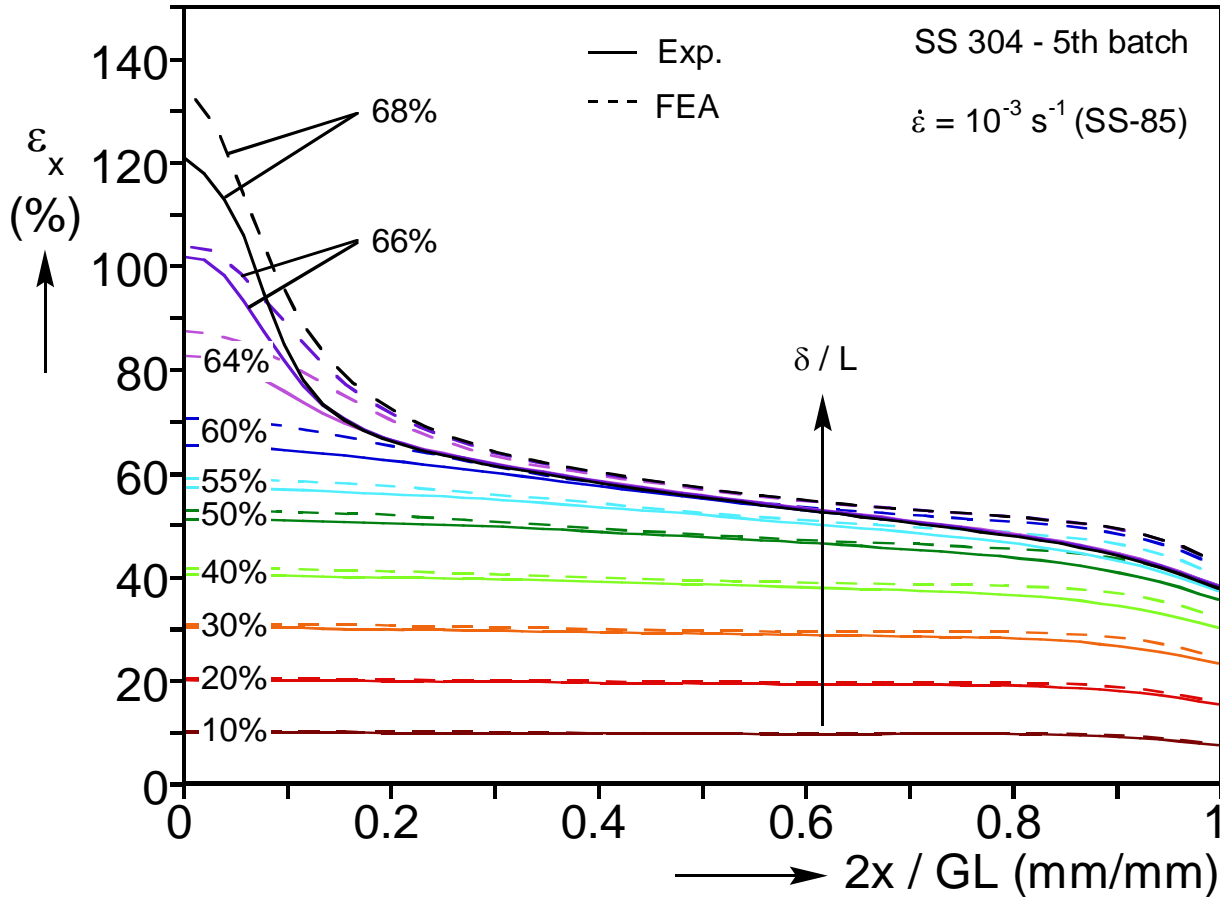


Figure 4-15: Axial engineering strain development along the specimen during a monotonic tension experiment and its numerical prediction

Apparently, the continuum description adopted here misses a series of phenomena that affect the heat balance, and as a result the induced temperature field. In summary, these include: a) the inelastic heat fraction, b) the martensitic transformation, and c) the thermoelastic

cooling. The inelastic heat fraction has been kept constant throughout the simulation, while there is evidence in the literature that this is not accurate (Knysh & Korkolis, 2015). In addition, the inelastic heat fraction changes with the strain-rate, which becomes relevant after the onset of necking.

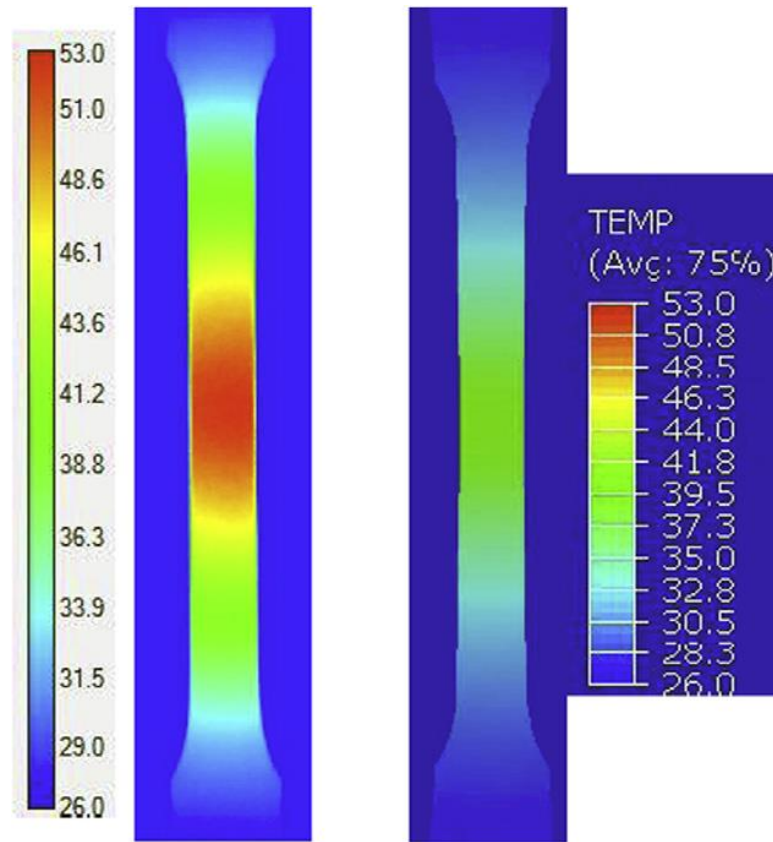


Figure 4-16: Comparison of the predicted temperature distribution along the monotonic tension specimen SS-85  $\sigma_{e \frac{1}{4} 10_{-3} = sP$  at  $e = 60.5\%$  to the infrared image recorded during the experiment.

These observations would alter the amount of heat that is generated for a given increment in the plastic work, and hence alter the temperature distribution. Furthermore, 304 stainless steel is susceptible to martensitic transformation ( (Meyers, 1998); (Cho, Yoo, & Jonas, 2000); (De, Murdock, Mataya, Speer, & Matlock, 2004); (Papatriantafillou, Agoras, Aravas, &

Haidemenopoulos, 2006) (Lee, Kim, & Han, 2010) (Beese & Mohr, 2011) (Moser, Gross, & Korkolis, 2014)), which is triggered by an appropriate combination of plastic deformation and temperature. The latent heat of this transformation has been neglected here. However, the mechanical aspects of the transformation are implicitly included in the modeling (see  $T = 25$  °C curve in Figure 4-11), Lastly, while the thermoelastic cooling (during loading) and heating (during unloading) is typically a fraction of a degree Celsius, in these experiments we have measured at large plastic strains cooling or heating temperature differences that exceeded 4-5 °C, including the heat transfer effects (see Figure 3-8). In contrast, no thermoelastic cooling or heating was included in the simulations. Finally, all the material thermal properties (specific heat, heat conductivity, etc.,) were kept constant with temperature, which is another departure from reality. In addition to these theoretical shortcomings, it was practically impossible to control the ambient temperature and air flow during the experiments and from specimen to specimen. As an indication of the sensitivity of the results to the convection to the surrounding air, Figure - 17 shows the dependence of the overshooting during reloading on the film coefficient. To allow direct comparison of the amount of overshooting between the different cases, the responses were shifted in strain (by less than 1% strain) so that the linear unloading overlapped in all simulations. Then, each stress response was normalized with the stress at the onset of the previous unloading. The “clipped” behavior for  $h > 20$  W/m<sup>2</sup>-K is not due to some numerical deficiency but due to the lack of experimental data for the flow curve and strain-rate dependence at the relevant temperatures and strain-rates. It can be seen from Figure 4-17 that relatively small changes in that boundary condition can markedly affect the intensity of the peak. This overshooting, which is physically associated with strain aging and is beyond the capabilities of the constitutive model adopted, is alternatively shown here to be regulated by the convection of heat to the surrounding air.

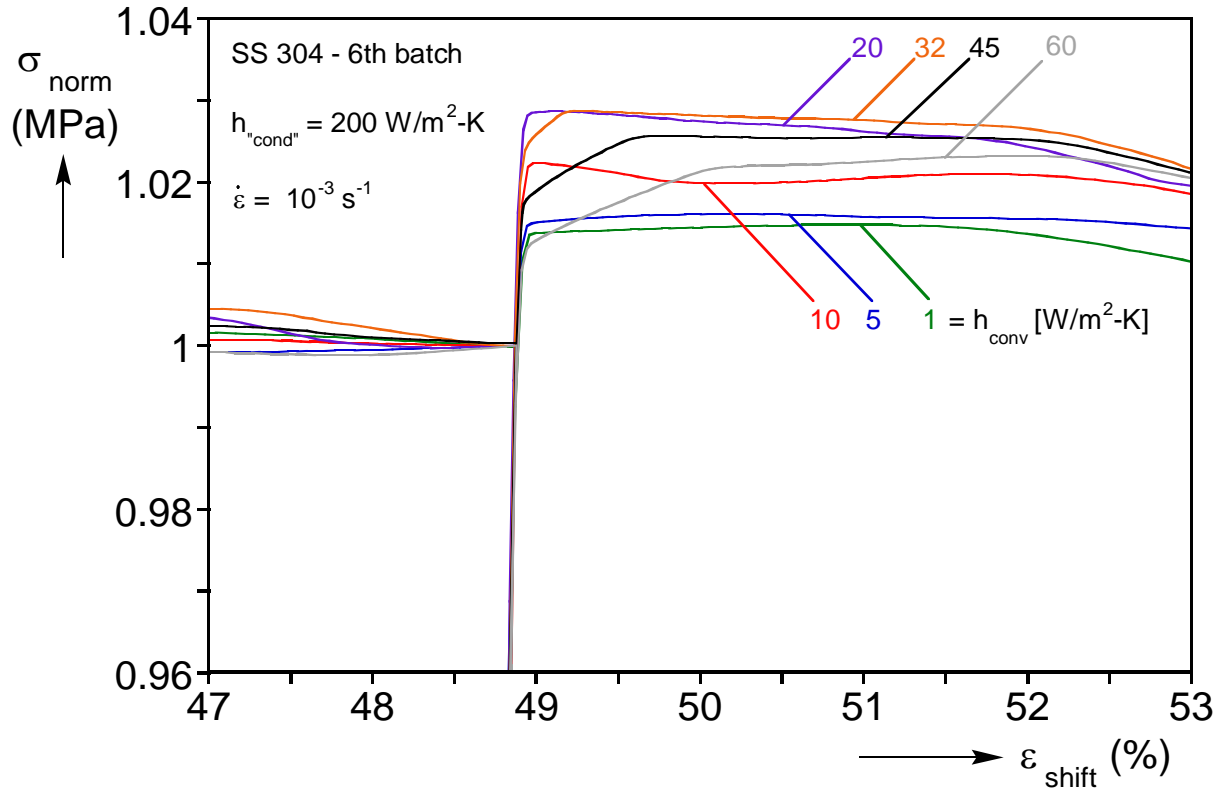


Figure 4-17: Numerical simulation of the dependence of the overshooting during reloading on the heat transfer between the specimen and the still air

Figure 3-12 which showed the correlation between experiment duration and elongation-to-fracture observed in the experiments can be now updated with the numerical predictions (see Figure 4-18). Notice that this plot contains all loading cases (e.g., monotonic, pulsed, etc.), which are not explicitly identified in the plot to simplify the presentation. Experimental results from two batches of SS-304 are included, which yielded slightly different elongations-to-fracture. The numerical model was calibrated from specimens from batches 4 to 6; hence the numerical predictions are closer to these results. The model reproduces the trends and values observed in the experiments very well. The transition to the adiabatic (at short experiment durations) and isothermal (at very large experiment durations) asymptotes is also well reproduced. It can be concluded that enough features of the problem have been represented by the material



characterization and the numerical modeling to quantitatively capture the behavior observed in the experiments.

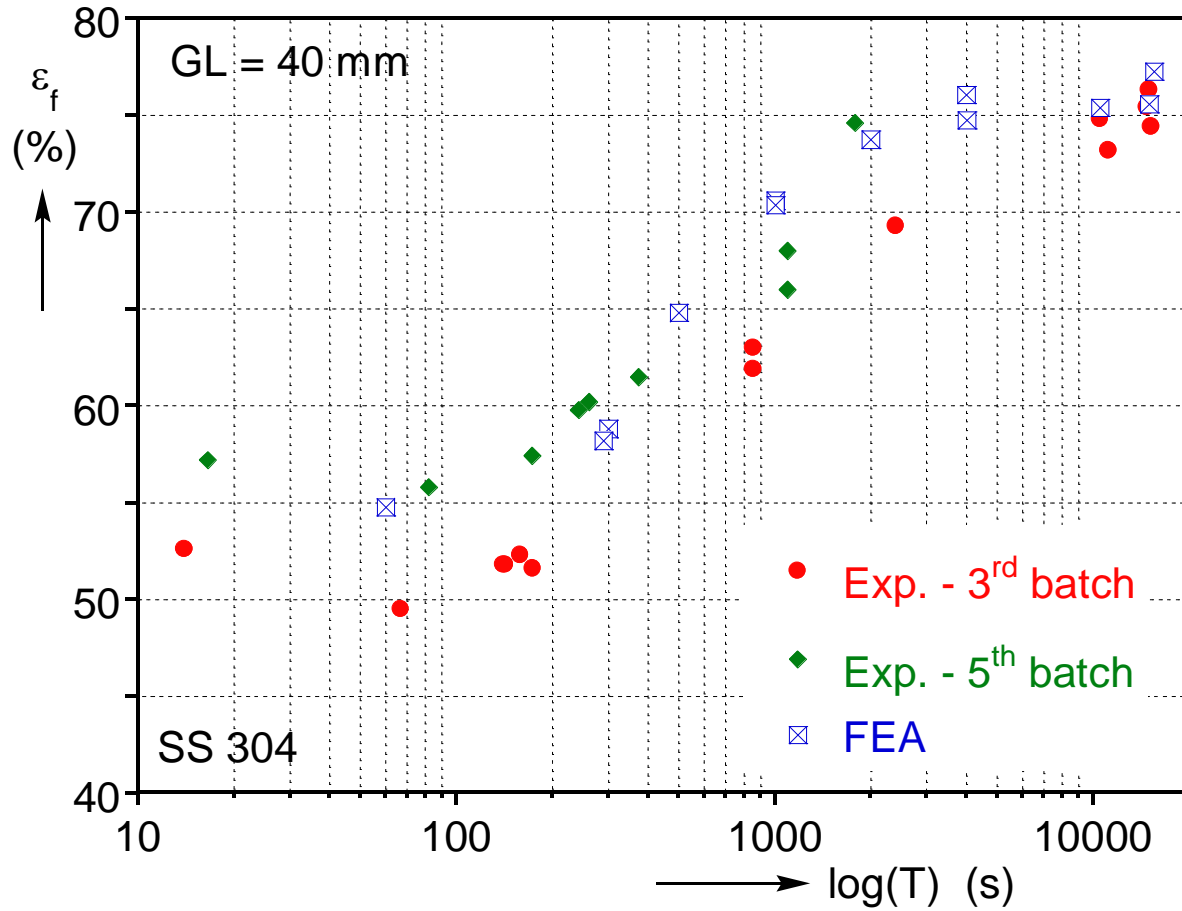


Figure 4-18: Numerical predictions of the dependence of the elongation-to-fracture on the duration of the experiment, plotted with multiple experimental data.

## CHAPTER 5

### CONCLUSIONS

A combined experimental/numerical approach was used to investigate the enhanced elongation-to-fracture of 304 stainless steel under pulsed uniaxial tension. Three types of experiments were performed: standard monotonic (master and equal time), pulsed and hold. It was observed that for this material, the pulsed application of the load for a range of strain-rates enhances the elongation-to-fracture over the monotonic case. This phenomenon is erased if the experiment is performed sufficiently fast ( $\dot{\epsilon} > 5 \times 10^{-2}$  /s) or slowly ( $\dot{\epsilon} < 10^{-4}$  /s). Hold experiments were performed to disclose if this phenomenon is due to the repeated unloading and reloading. These experiments yielded the same elongation-to-fracture as the pulsed ones, precluding the unload-reload mechanism from being a plausible explanation for this effect.

It was observed that SS-304 heated up significantly during the experiments (e.g., anywhere between 35 and 100 °C), due to the combination of deformation-induced heating and the low thermal conductivity of this material. This established a temperature gradient along the specimens, which acted as an imperfection and triggered an earlier localization of deformation in comparison to the corresponding isothermal case. Subsequently, monotonic experiments were designed so as to have the same duration as the pulsed and hold ones. These experiments exhibited the same elongation-to-fracture as their equally timed pulsed and hold counterparts. Hence it was established that the enhanced elongation-to-fracture is induced and regulated by the temperature gradients. Indeed, this elongation correlates directly to the duration of the experiment, irrespectively of the way the load is applied (monotonically, pulsed, etc.).

The importance of the temperature gradients in the behavior observed dictated the use of a coupled (temperature-displacement), rate-dependent numerical model. The simulations were performed with the nonlinear code Abaqus/Standard. The greatest challenge in this part of the work was the material modeling, i.e., the decoupling of the thermal and the mechanical behaviors observed in a conventional material characterization experiment. This was achieved by the use of a specially devised, simple isothermal tension experiment, which allowed the measurement of mechanical properties under controlled isothermal conditions. These properties were then input to the fully-coupled numerical model. The picture was complicated further because 304 stainless steel is susceptible to martensitic transformation around room temperature. The mechanical aspect of this was input to the model in a purely phenomenological way (see  $T = 25\text{ }^{\circ}\text{C}$  experiment in [Figure 3-14](#) and [4-11](#)), while the heat due to the transformation was omitted. In the simulations, isotropic hardening (which yielded the linearized unloading and reloading behavior), constant thermal (e.g., thermal conductivity, specific heat, etc.) and thermomechanical (e.g., inelastic heat fraction) properties and yield-ratios for the strain-rate dependence (instead of the actual curves) were adopted. In addition, the thermoelastic cooling and heating were omitted. Despite these features, the simulations were very successful in accurately predicting the elongation-to-fracture in every case simulated (see [Figure 4-18](#)). However, the induced temperature fields were found to deviate from the experimental ones.

# BIBLIOGRAPHY

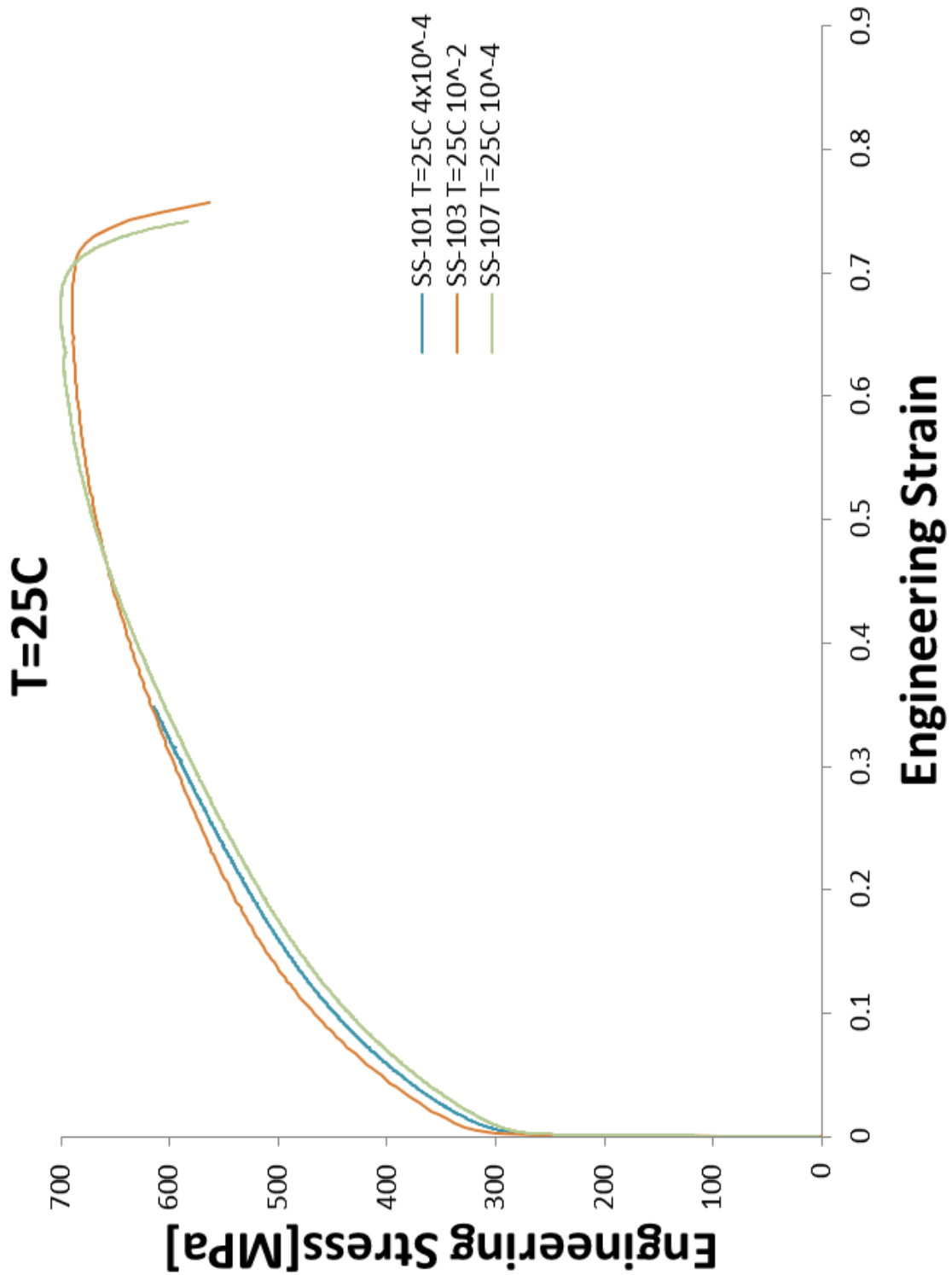
- Andrade-Campos, A. T.-D. (2010). Effect of strain rate, adiabatic heating and phase transformation phenomena on the mechanical behavior of stainless steel. *Stain*, 283-297.
- Anon. (2009). Abaqus Ver. 6.9 Documentation. Simulia Central.
- Banabic, D. a. (1982). Thermoelactic Instabilities in Metals. *Physica Scripta(T1)*, 65-70.
- Banabic, D. a. (1994). Prediction of forming limit diagrams in pulsatory straining. *Journal of Material Processing Technology*, 45(1-4), 551-556.
- Banabic, D. a. (2005). Bulge testing under constant and variable strain rates of superplastic aluminum alloys. *CIRP Annuals*, 54, 205-208.
- Beese, A. M., & Mohr, D. (2011). Identification of the direction-dependency of martensitic transformation in stainless steel using in situ magnetic permeability measurements. *Experimental Mechanics*, 667-676.
- Bottani, C. a. (1982). Thermoelactic Instabilities in Metals. *Physica Scripta, T1*, 65-70.
- Bower, A. (2009). *Applied Mechanics of Solids*. Boca Raton, Florida: CRC Press.
- Chen, W. (1971). Necking of a bar. *International Journal of Solids and Structures*, 685-717.
- Cho, S. H., Yoo, Y. C., & Jonas, J. J. (2000). Static and Dynamic strain aging in 304 austenitic stainless steel at elevated temperatures. *Journal of Material Science Lett.*, 2019-2022.
- Cleveland, R. a. (2002). Inelastic effects on springback in metals. *International Journal of Plasticity*, 18, 769-785.
- Dablij, M. a. (1997). Portevin-Le Chatelier Plastic Instabilities: Characteristics of Deformation Bands. *Materials Science and Engineering*, 1-5 Web.
- De, A. K., Murdock, D. C., Mataya, M. C., Speer, J. G., & Matlock, D. K. (2004). Quantitative measurement of deformation-induced martensite in 304 stainless steel by X-ray diffraction. *Scripta Materialia*, 1445-1449.
- Dumoulin, S. L. (2010). Heat sources, energy storage and dissipation in high-strength steels: experiments and modeling. *European Journal of Mechanics-A/Solids*, 29(3), 461-474.
- Farren, W. S., & Taylor, G. I. (1925). The heat developed during plastic extension of metals. *Proceeding of the Royal Society of London*, 107, pp. 422-451. London.
- Gao Y. and Wagoner, R. (1991). A simplified model of heat generation during the uniaxial tensile test. *Metallurgical Transactions A*, 18(6), 1001-1009.

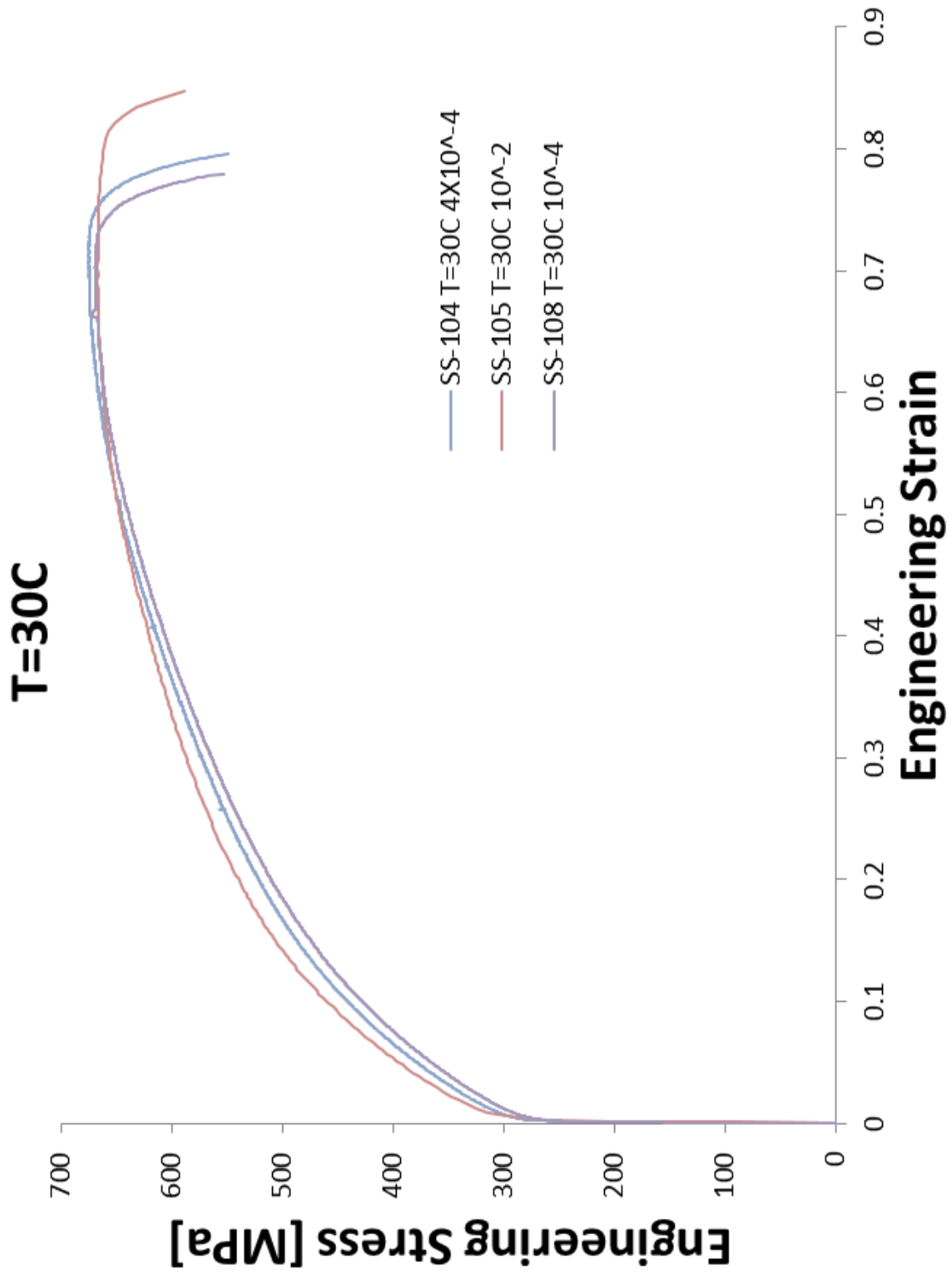
- Hodowany, J., Ravichandran, G., Rosakis, A. J., & Rosakis, P. (2000). Partition of plastic work into heat and energy in metals. *Exp. Mech.*, *40*, 113-123.
- Khan, A. P. (2010). Evolution of subsequent yield surfaces and elastic constants with finite plastic deformation. Part III: Yield surface in tension–tension stress space (Al 6061–T 6511 and annealed 1100 Al). *International Journal of Plasticity*, *26*, 1432-1441.
- Kim, Y. a. (1987). An analytical investigation of deformation-induced heating in tensile testing. *International Journal of Mechanical Sciences*, *29*(3), 179-194.
- Knysh, P., & Korkolis, Y. P. (2015). Determination of the fraction of plastic work converted into heat in metals. *Mechanics of Materials*, *86*, 71-80.
- Korkolis, Y. a. (2011). Hydroforming of anisotropic aluminum tubes. Part I: Experiments. *International Journal of Mechanical Sciences*, *53*, 75-82.
- Lee, M. -G., Kim, S. -J., & Han, H. -N. (2010). Crystal plasticity finite element modeling of mechanically induced martensitic transformation (MIMT) in metastable austenite. *International Journal of Plasticity*, 688-710.
- Lin, M. a. (1987). An experimental investigation of deformation-induced heating during tensile testing. *Metallurgical Transactions A*, *18*, 1035-1042.
- Maldague, X. (2001). *Theory and practice of infrared technology for nondestructive testing*. New York: Wiley-Interscience.
- Meyers, M. a. (1998). *Mechanical behavior of materials*. Englewood Cliffs, New Jersey: Prentice-Hal.
- Mori, K. M. (2007). Mechanism of improvement of formability in pulsating hydroforming of tubes. *International Journal of Machine Tools and Manufacturing*, *47*, 978-984.
- Mori, K. P. (2004). Improvement of formability by oscillation of internal pressure in pulsating hydroforming of tubes. *CIRP Annals*, *53*, 215-218.
- Moser, N. H., Gross, T. S., & Korkolis, Y. P. (2014). Martensite formation in conventional and isothermal tension of 304 austenitic stainless steel measured by x-ray diffraction. *Metallurgical and Materials Transactions*, 4891-4896.
- Papatriantafillou, I., Agoras, M., Aravas, N., & Haidemenopoulos, G. (2006). Constitutive modeling and finite element methods for TRIP steels. *Computational Methods Applied Mechanical Engineering*, 5094-5114.
- Raghavan K.S. and Wagoner, R. (1987). Combined influence of geometric defects and thermal-gradients on tensile ductility. *Metallurgical Transactions A*, *18*(12), 2143-2150.
- Rusinek, A. a. (2009). Experiments on heat generated during plastic deformation and stored energy for TRIP steels. *Materials & Design*, *30*(1), 35-48.

- Sun, L. a. (2011). Complex unloading behavior: nature of the deformation and its consistent constitutive representation. *International Journal of Plasticity*, 27, 1126-1144.
- Sung, J. K. (2010). A plastic constitutive equation incorporating strain, strain-rate, and temperature. *International Journal of Plasticity*, 26, 1746-1771.
- Sutton, M. O.-J. (2009). *Image correlation for shape, motion and deformation measurements: basic concepts, theory and applications*. New York: Springer.
- Tugcu, P. (1995). Heat-conduction effects on strain localization in plane-strain tension. *International Journal for Numerical Methods in Engineering*, 38(12), 2083-2099.
- Yoshida, F. U. (2002). Elastic–plastic behavior of steel sheets under in-plane cyclic tension–compression at large strain. *International Journal of Plasticity*, 18, 633-659.
- Zehnder, A. T., Babinsky, E., & Palmer, T. (1998). Hybrid method for determining the fraction of plastic work converted to heat. *Exp. Mech.*, 38, 295-302.
- Zhang, S. a. (2009). Research on mechanism of formability improvement in pulsating hydroforming of tubes. 4th Int'l Conference on Tube Hydroforming. *TubeHydro 2009*. Kaohsiung, Taiwan.

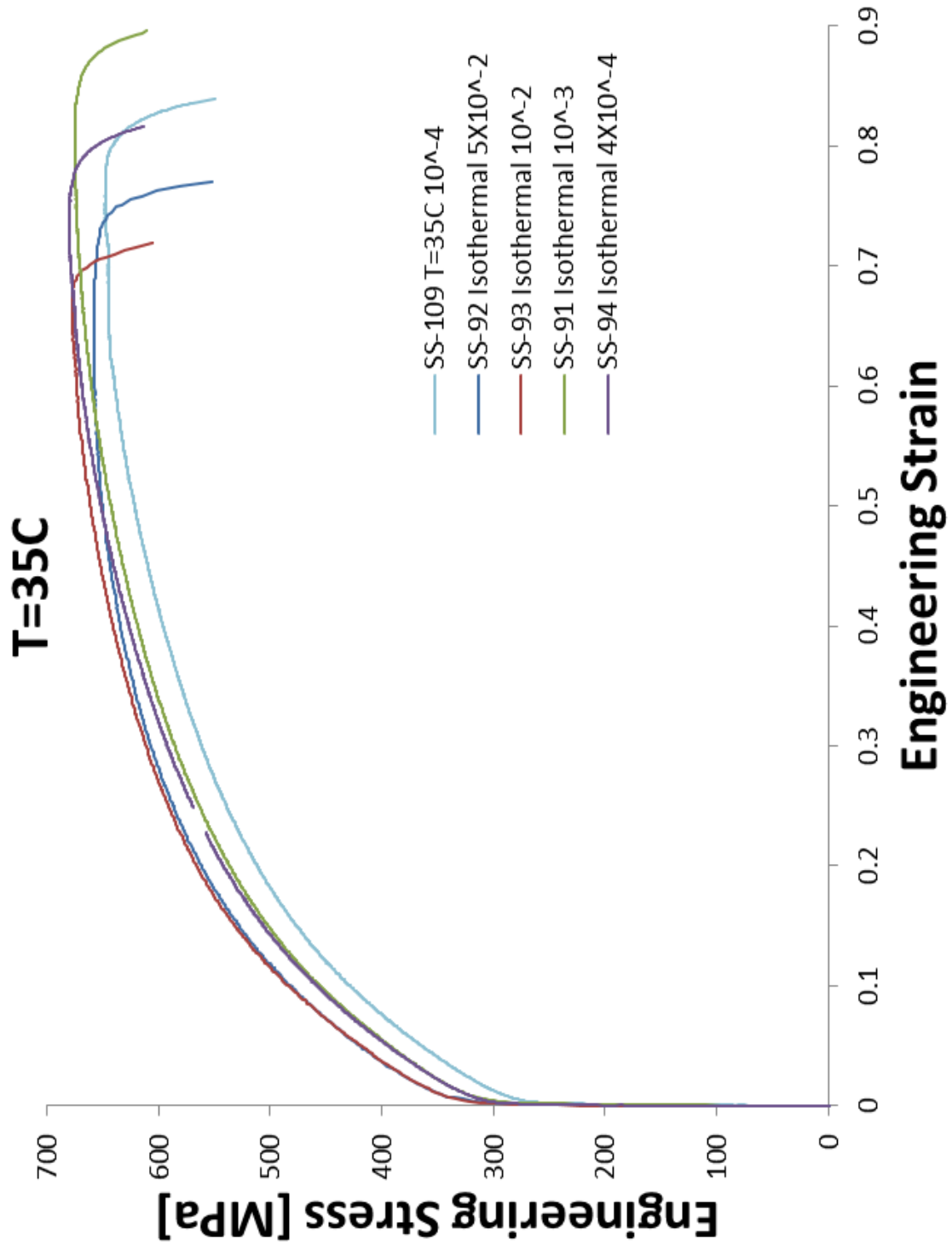
# APPENDIX A

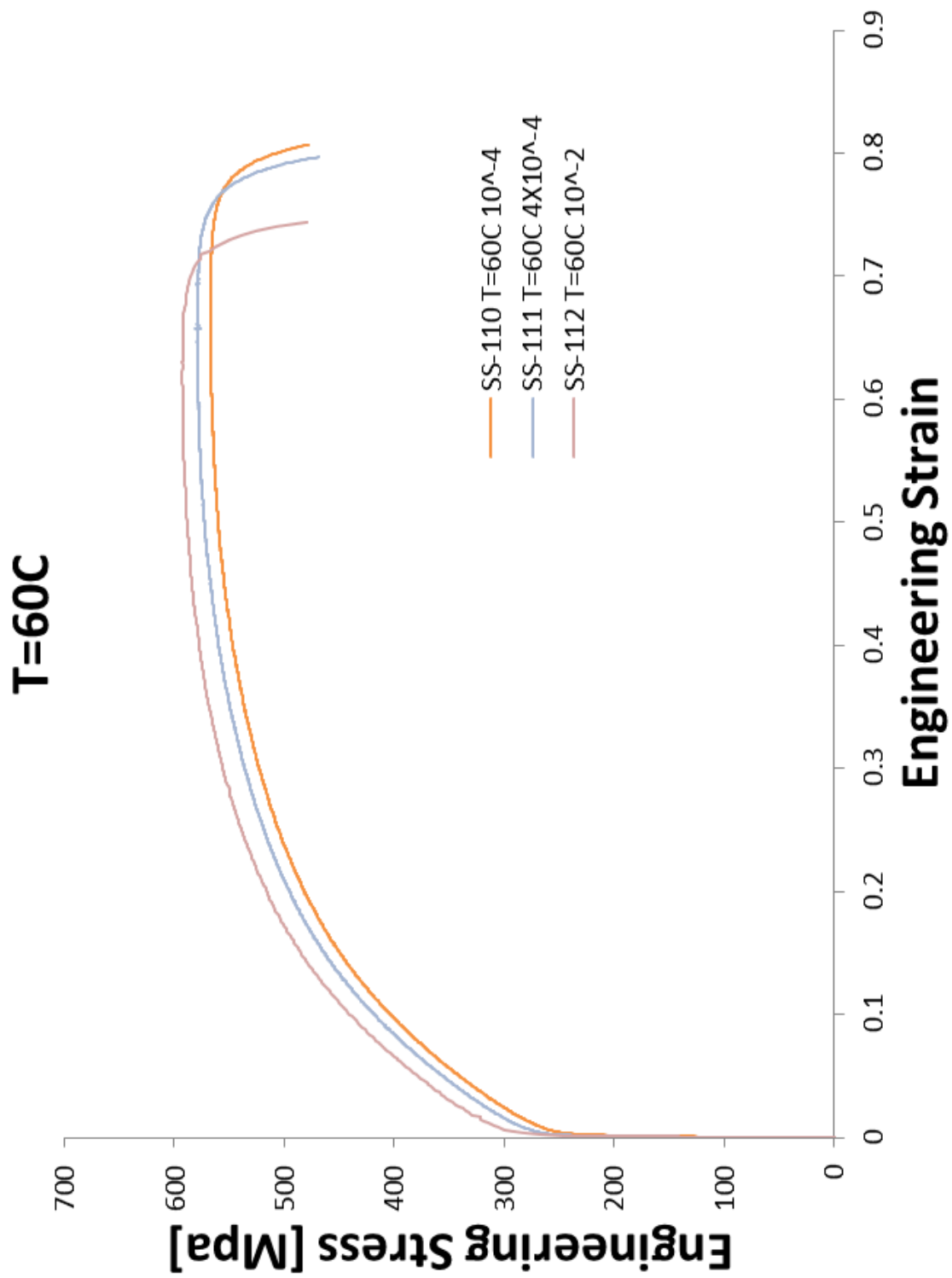
Iso-thermal Stress Strain Experimental Curves at 25, 30, 35, 60, 100, and 150°C



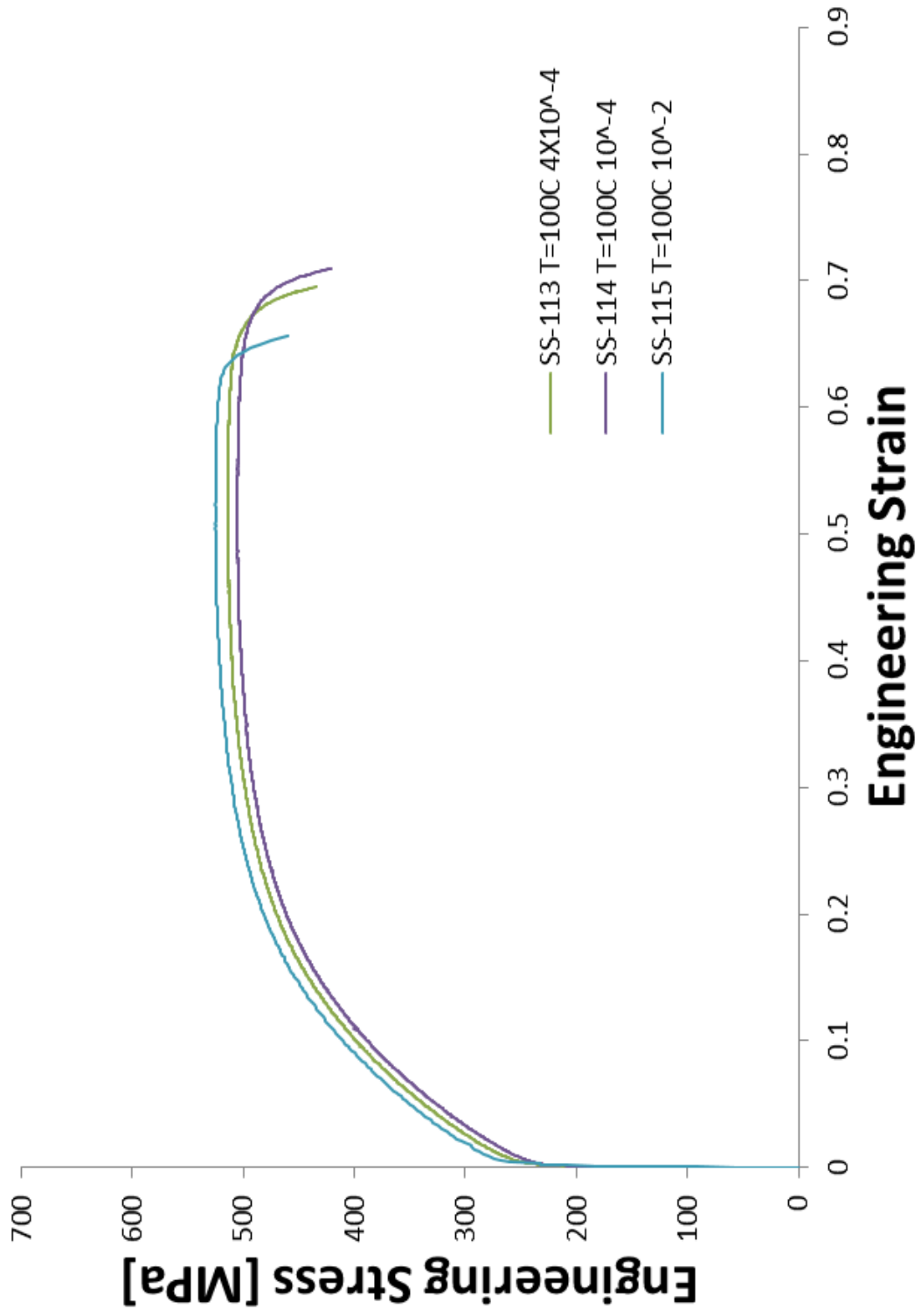




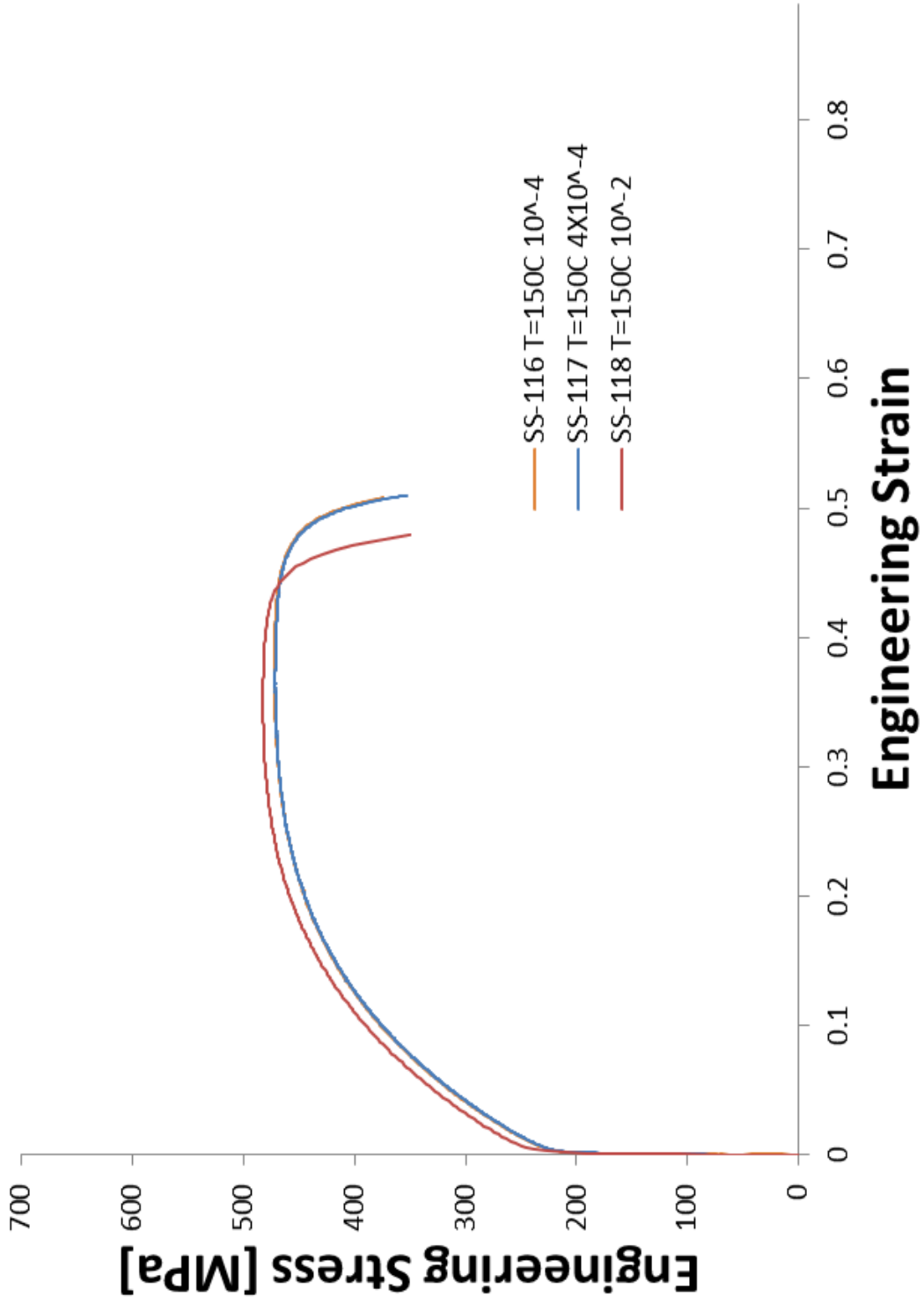




**T=100C**



**T=150C**



## APPENDIX B: List of all SS304 experiments

Specimen	Strain Rate		Material	Description	Data	Comments
	[1/Sec]	[mm/min]				
SS-8	10 <sup>-3</sup>	00003	SS304 Dec 09	Monotonic	No DIC	No Measurements Taken
SS-9	10 <sup>-3</sup>	3.05	SS304 Dec 09	Pulsed	DIC 1Hz, DAX 2Hz	GL Reset at ~65% to 49.64% No measurements
SS-10	10 <sup>-3</sup>	3.05	SS304 Dec 09	Monotonic	DIC 1Hz, DAX 3Hz	Repeat of SS-8, No Measurements
SS-11	10 <sup>-3</sup>	3.05	SS304 Dec 09 90°	Monotonic	DIC 1 Hz, DAX 3Hz	Some Anisotropy
SS-12	10 <sup>-3</sup>	3.05	SS304 Feb 10	Monotonic	DIC 1 Hz, DAX 3Hz	
SS-13	10 <sup>-3</sup>	3.05	SS304 Dec 09	Monotonic with Hold	DIC 1/2Hz, DAX 1Hz	Holding and Relative Ramp changed to match the unloading points of SS-9
SS-14	10 <sup>-3</sup>	3.05	SS304 Dec 09	Monotonic with Hold	DIC 1Hz, DAX 1Hz	Same as SS-13 but with holding times that better reflect the time it took to unload during SS-9
SS-15		1.08	SS304 Dec 09	Monotonic with total time equal to the pulsed test SS-9	DIC 1Hz, DAX 1Hz	
SS-16	10 <sup>-2</sup>	30.5	SS304 Feb 10	Monotonic	DIC 2Hz, DAX 1Hz	DIC failed (Vic Snap 2009)
SS-17	10 <sup>-2</sup>	30.5	SS304 Feb 10	Monotonic	DIC 2Hz, DAX 1Hz	DIC failed (Vic Snap 2009)
SS-18	10 <sup>-2</sup>	30.5	SS304 Feb 10	Pulsed	DIC 2Hz, DAX 1Hz	Using Vic Snap 2008
SS-19	10 <sup>-2</sup>	30.5	SS304 Feb 10	Monotonic with Hold	DIC 2Hz, DAX 1Hz	Holding and Relative Ramp changed to match the unloading points of SS-18
SS-20	10 <sup>-2</sup>	30.5	SS304 Feb 10	Monotonic with Hold	DIC 2Hz, DAX 1Hz	Same as SS-19 but with holding times that better reflect the time it took to unload during SS-18
SS-21	10 <sup>-2</sup>	30.5	SS304 Feb 10	Failed		

SS-22		6.133	SS304 Feb 10	Monotonic with total time equal to the pulsed test SS-18	DIC 2Hz, DAX 1Hz	Using the SS-18 total length at breaking and the time it took to reach that point the Strain rate was calculated. 36.8mm in 360s
SS-23	4x10 <sup>-4</sup>	1.22	SS304 Feb 10	Monotonic	DIC 1/2Hz, DAX 1Hz	A lot of noise in the system and extensometer A heat sink with fan was added to help keep the specimen at ambient temperature. Specimen broke at the point furthest from the HS and grip, not in the middle. Extensometer was not able to capture the necking as it occurred outside of its GL.
SS-24	4x10 <sup>-4</sup>	1.22	SS304 Feb 10	Monotonic-Isothermal	No DIC	
SS-25	10 <sup>-3</sup>	3.05	SS304 Dec 09	Failed		
SS-26	10 <sup>-3</sup>	3.05	SS304 Dec 09	Pulsed	DIC 1/2Hz, DAX 1Hz	Repeat of SS-9
SS-27	4x10 <sup>-4</sup>	1.22	SS304 Feb 10	Pulsed	DIC 1/2Hz, DAX 1Hz	Holding and Relative Ramp changed to match the unloading points of SS-27
SS-28	4x10 <sup>-4</sup>	1.22	SS304 Feb 10	Monotonic with Hold	DIC 1/2Hz, DAX 1Hz	Using the SS-27 total length at breaking and the time it took to reach that point the Strain rate was calculated. 51.12mm in 3665s
SS-29	4x10 <sup>-4</sup>	0.837	SS304 Feb 10	Monotonic with total time equal to the pulsed test SS-27	DIC 1/3Hz, DAX 1Hz	
SS-30	10 <sup>-3</sup>	3.05	SS304 Feb 10	Monotonic	No DIC	Test to get a graph to compare the three monotonic strain rates but with the same material
SS-31	10 <sup>-3</sup>	3.05	SS304 Feb 10	Monotonic with Hold	No DIC	Used to give a more accurate overall time for the Hold specimen
SS-32	4x10 <sup>-4</sup>	1.22	SS304 Feb 10	Monotonic with Hold	No DIC	Used to give a more accurate overall time for the Hold specimen

SS-33	10 <sup>-3</sup>	3.05	SS304 Feb 10	Monotonic	DIC 1Hz, DAX 1Hz, Thermal Imaging	Ramp endpoint not set far enough, Thermal Imaging information not fully recorded
SS-34	10 <sup>-2</sup>	30.5	SS304 Feb 10	Monotonic	DIC 1Hz, DAX 1Hz, Thermal Imaging 1/3Hz	All Data recorded and compared 8/10/10
SS-35	10 <sup>-1</sup>	305	SS304 Feb 10	Monotonic	DIC 2Hz, DAX 5Hz	Ramp endpoint not set far enough, First new SS comparison between lines and DIC
SS-36	10 <sup>-1</sup>	305	SS304 Feb 10	Monotonic	DIC 5Hz, DAX 10Hz	Scribed Strain lines could not be followed after ~ half way though the test Successful comparison of Strain Lines and DIC
SS-37	10 <sup>-1</sup>	305	SS304 Feb 10	Monotonic	DIC 10Hz, DAX 10Hz	8/10/10
SS-38	10 <sup>-3</sup>	3.05	SS304 Feb 10	Monotonic	DIC 1Hz, DAX 1Hz	No Measurements Taken
SS-39	10 <sup>-3</sup>	3.05	SS304 Feb 10	Monotonic	DIC 1Hz, DAX 1Hz	IsoThermal
SS-40	5x10 <sup>-2</sup>	152.5	SS304 Aug 10	Monotonic		Recalling user state turned off the instron breaking the specimen
SS-41	5x10 <sup>-2</sup>	152.5	SS304 Aug 10	Monotonic	DIC 5Hz, DAX 5Hz	
SS-42	5x10 <sup>-2</sup>	152.5	SS304 Aug 10	Pulsed	DIC 5Hz, DAX 5Hz	
SS-44	5x10 <sup>-2</sup>	152.5	SS304 Aug 10	Equal Time	DIC 5Hz, DAX 5Hz	
SS-45	5x10 <sup>-2</sup>	152.5	SS304 Aug 10	Hold	DIC 5Hz, DAX 5Hz	DIC failed (Vic Snap 2009)
SS-46	5x10 <sup>-2</sup>	152.5	SS304 Aug 10	Hold	DIC 5Hz, DAX 5Hz	Hold Points do not match well with Puled SS-42
SS-47	10 <sup>-3</sup>	3.05	SS304 Aug 10	Monotonic	DIC 2Hz, DAX 2Hz	
SS-48	5x10 <sup>-2</sup>	152.5	SS304 Aug 10	Hold	DIC 5Hz, DAX 5Hz	Better Hold Point for comparison to pulsed SS-42

SS-49	10 <sup>-3</sup>	3.05	SS304 Aug 10	Monotonic	DIC 1Hz, DAX 1Hz	DIC failed (Vic Snap 2009)
SS-50	10 <sup>-1</sup>	305	SS304 Aug 10	Monotonic	DIC 10Hz, DAX 10Hz	Retest with GL 40mm
SS-51	10 <sup>-3</sup>	3.05	SS304 Feb 10	Monotonic	DIC 1Hz, DAX 1Hz	
SS-52	10 <sup>-4</sup>	0.305	SS304 Aug 10	Monotonic	DIC 1/5Hz, Dax 1Hz	
SS-53	10 <sup>-4</sup>	0.305	SS304 Aug 10	Pulsed	DIC 1/10Hz, Dax 1Hz	
SS-54	10 <sup>-4</sup>	0.305	SS304 Aug 10	Equal Time	DIC 1/10Hz, Dax 1Hz	
SS-55						
SS-56	10 <sup>-4</sup>	0.305	SS304 Aug 10	Hold	DIC 1/10Hz, Dax 1Hz	
SS-57	10 <sup>-4</sup>	0.31	Aug 10 SS304	Hold	DIC 1/10Hz, Dax 1Hz	Better Hold Times Then SS-55
SS-58	4x10 <sup>-4</sup>	1.22	Aug 10 SS304	Monotonic	DIC 1/5Hz, Dax 1Hz	Needed to Compare monotonic test with one material
SS-59	10 <sup>-2</sup>	30.5	Aug 10 SS304	Monotonic	DAX 20Hz	
SS-60	10 <sup>-2</sup>	30.5				
SS-61	5x10 <sup>-2</sup>	153				
SS-62			Feb 10 SS304			ThermoCouple attempt Failed
SS-63	10 <sup>-2</sup>	30.5	Feb 10 SS304	Hold		Retest of SS-20
SS-64	10 <sup>-3</sup>	3.05	Nov 10 SS304	Monotonic	DIC 1Hz, DAX 1Hz, IR 6.25Hz	New Material Comparison, found to be annealed
SS-65	10 <sup>-3</sup>	3.05	Nov 10 SS304	Monotonic	DIC 1Hz, DAX 1Hz, IR 1Hz	Restest of SS-64 for reproducibility
SS-66	10 <sup>-3</sup>	3.05	Nov 10 SS304 90 Degrees	Mototonic	DIC 1Hz, DAX 1Hz, IR 1Hz	New Material Comparison at 90 degrees, found to be annealed
SS-67	10 <sup>-3</sup>	3.05	Nov 10 SS304 Second Sheet	Mototonic	DIC 1Hz, DAX 1Hz, IR 1Hz	New Material second sheet Comparison at 0 degrees, found to be annealed
SS-68	10 <sup>-3</sup>	3.05	Nov 10 SS304 Choice Metals	Mototonic	DIC 1Hz, DAX 1Hz, IR 1Hz	New Material choice metals sheet Comparison



Sheet

SS-69	10 <sup>-3</sup>	3.05	Nov 10 SS304	IsoThermal Monotonic	DIC 1Hz, DAX 1Hz, IR 1Hz	T = 0C Failed actuator ran out of travel
SS-70	10 <sup>-3</sup>	3.05	Nov 10 SS304	IsoThermal Monotonic	DIC 1Hz, DAX 1Hz, IR 1Hz	T = 25C
SS-71	10 <sup>-3</sup>	3.05	Nov 10 SS304	IsoThermal Monotonic	DIC 1Hz, DAX 1Hz, IR 1Hz	T = 60C
SS-72	10 <sup>-3</sup>	3.05	Nov 10 SS304	IsoThermal Monotonic	DIC 1Hz, DAX 1Hz, IR 1Hz	T = 100C
SS-73	10 <sup>-3</sup>	3.05	Nov 10 SS304	IsoThermal Monotonic	DIC 1Hz, DAX 1Hz, IR 1Hz	T = 25C Retest of SS- 70
SS-74	10 <sup>-3</sup>	3.05	Nov 10 SS304	Pulsed	DIC 1Hz, DAX 1Hz, IR 1Hz	Failed due to number of pulses
SS-75	10 <sup>-3</sup>	3.05	Nov 10 SS304	Pulsed	DIC 1Hz, DAX 1Hz, IR 1Hz	Repeat of SS-74
SS-76	10 <sup>-3</sup>	3.05	Feb 11 Choice Metals	Monotonic	DIC=DAX=1hz	No IR, UTS 711MPa, Eu = 55%
SS-77	10 <sup>-3</sup>	3.05	Feb 11 Choice Metals	Monotonic	DIC=DAX=1hz	Validity test of SS-76
SS-78	10 <sup>-3</sup>	3.05	Feb 11 Choice Metals	Pulsed	DIC=DAX=1hz	Increased Ductility Test
SS-79	10 <sup>-3</sup>	3.05	Feb 11 Choice Metals	Pulsed	N/A	Vic-Gauge Test, total Failure
SS-80	5X10 <sup>-3</sup>	15.2	McMaster Annealed	Monotonic	DIC 1Hz, DAX 1Hz, IR 1Hz	
SS-81	10 <sup>-2</sup>	30.4	McMaster Annealed	Monotonic	DIC 1Hz, DAX 1Hz, IR 1Hz	
SS-82	5X10 <sup>-2</sup>	152	McMaster Annealed	Monotonic	DIC 5Hz, DAX 5Hz, IR 5Hz	
SS-83	2.5X10 <sup>-3</sup>	7.6	McMaster Annealed	Monotonic	DIC 1Hz, DAX 1Hz, IR 1Hz	
SS-84	10 <sup>-3</sup>	3.05	McMaster 2/26/11	Monotonic	DIC 1Hz, DAX 1Hz, IR 1Hz	
SS-85	10 <sup>-3</sup>	3.05	McMaster 2/26/11	Monotonic	DIC 1Hz, DAX 1Hz, IR 1Hz	
SS-86	10 <sup>-2</sup>	30.4	McMaster Annealed	Pulsed	DIC 4Hz, DAX 4Hz, IR 4Hz	

SS-87	10 <sup>-2</sup>	11.14	McMaster Annealed	Equal Time	DIC 4Hz, DAX 4Hz, IR 4Hz	
SS-88	5X10 <sup>-3</sup>	15.2	McMaster Annealed	Pulsed	DIC 2Hz, DAX 2Hz, IR 2Hz	
SS-89	5X10 <sup>-3</sup>	8.1	McMaster Annealed	Equal time	DIC 2Hz, DAX 2Hz, IR 2Hz	
SS-90	10 <sup>-3</sup>	2.03	McMaster Annealed	Equal Time	DIC 1Hz, DAX 1Hz, IR 1Hz	
SS-91	10 <sup>-3</sup>	3.04	McMaster Annealed	Monotonic	DIC 1Hz, DAX 1Hz, IR 1Hz	IsoThermal T=35C
SS-92	5X10 <sup>-2</sup>	152	McMaster Annealed	Monotonic	DIC 5Hz, DAX 10Hz, IR 5Hz	IsoThermal T = 35C
SS-93	10 <sup>-2</sup>	30.4	McMaster Annealed	Monotonic	DIC 5Hz, DAX 5Hz, IR 5Hz	IsoThermal T=35C
SS-94	4x10 <sup>-4</sup>	1.22	McMaster Annealed	Monotonic	DIC 1/2Hz, Dax 1Hz, IR 1/2Hz	IsoThermal T=35C
SS-95	5X10 <sup>-3</sup>	8.08	McMaster Annealed	Equal time	DIC 2Hz, DAX 2Hz, IR 2Hz	Retest SS-89
SS-96	10 <sup>-3</sup>	3.04	McMaster Annealed	Monotonic	DIC 1Hz, DAX 1Hz, IR 1Hz	IsoThermal T=30C
SS-97	10 <sup>-3</sup>	3.04	McMaster Annealed	Monotonic	DIC 1Hz, DAX 1Hz, IR 1Hz	IsoThermal T=30C
SS-98	10 <sup>-3</sup>	3.04	McMaster Annealed	Monotonic	DIC 1Hz, DAX 1Hz, IR 1Hz	IsoThermal T=30C
SS-99	10 <sup>-3</sup>	3.04	McMaster Annealed	Monotonic	DIC 1Hz, DAX 1Hz, IR 1Hz	IsoThermal T=35C
SS-100	10 <sup>-3</sup>	3.04	McMaster Annealed	Monotonic	DIC 1Hz, DAX 1Hz, IR 1Hz	IsoThermal T=150C
SS-101	4x10 <sup>-4</sup>	1.22	McMaster Last	Monotonic	DIC 1Hz, DAX 1Hz, IR 1Hz	IsoThermal T=25C
SS-102	10 <sup>-2</sup>	30.4	McMaster Last	Monotonic	Vic Snap Failed	IsoThermal T=25C
SS-103	10 <sup>-2</sup>	30.4	McMaster Last	Monotonic	DIC 2Hz, DAX 2Hz, IR 2Hz	IsoThermal T=25C
SS-104	4x10 <sup>-4</sup>	1.22	McMaster Last	Monotonic	DIC 1Hz, DAX 1Hz, IR 1Hz	IsoThermal T=30C
SS-105	10 <sup>-2</sup>	30.4	McMaster Last	Monotonic	DIC 2Hz, DAX 2Hz, IR 2Hz	IsoThermal T=30C
SS-106						
SS-107	10 <sup>-4</sup>	0.305	McMaster Last	Monotonic	DIC=DAX=IR=1Hz	IsoThermal T = 25C
SS-108	10 <sup>-4</sup>	0.305	McMaster Last	Monotonic	DIC=DAX=IR=1Hz	IsoThermal T = 30C

SS-109	10 <sup>-4</sup>	0.305	McMaster Last	Monotonic	DIC=DAX=IR=1Hz	IsoThermal T = 35C
SS-110	10 <sup>-4</sup>	0.305	McMaster Last	Monotonic	DIC=DAX=IR=1Hz	IsoThermal T = 60C
SS-111	4x10 <sup>-4</sup>	1.22	McMaster Last	Monotonic	DIC 1Hz, DAX 1Hz, IR 1Hz	IsoThermal T=60C
SS-112	10 <sup>-2</sup>	30.4	McMaster Last	Monotonic	DIC 4Hz, DAX 4Hz, IR 4Hz	IsoThermal T=60C
SS-113	4x10 <sup>-4</sup>	1.22	McMaster Last	Monotonic	DIC 1Hz, DAX 1Hz, IR 1Hz	IsoThermal T=100C
SS-114	10 <sup>-4</sup>	0.305	McMaster Last	Monotonic	DIC=DAX=IR=1/4Hz	IsoThermal T = 100C
SS-115	10 <sup>-2</sup>	30.4	McMaster Last	Monotonic	DIC 4Hz, DAX 4Hz, IR 4Hz	IsoThermal T=100C
SS-116	10 <sup>-4</sup>	0.305	McMaster Last	Monotonic	DIC=DAX=IR=1/4Hz	IsoThermal T = 150C
SS-117	4x10 <sup>-4</sup>	1.22	McMaster Last	Monotonic	DIC 1Hz, DAX 1Hz, IR 1Hz	IsoThermal T=150C
SS-118	10 <sup>-2</sup>	30.4	McMaster Last	Monotonic	DIC 4Hz, DAX 4Hz, IR 4Hz	IsoThermal T=150C